Structural and Electrical Investigations of Tungsten Substituted Barium (Strontium) Titanate Ferroelectric Ceramics

A thesis submitted

by

Sheela Devi

in fulfillment of the requirements
for the award of the degree of

Doctor of Philosophy

to

University of Delhi
Delhi, India

CERTIFICATE

This is to certify that the thesis entitled **"Structural and Electrical Investigations of Tungsten Substituted Barium (Strontium) Titanate Ferroelectric Ceramics"** being submitted by **Ms. Sheela Devi** to the **Faculty of Technology, University of Delhi, India** for the award of the degree of **Doctor of Philosophy** is a record of bonafide research work carried out by her. She has worked under my guidance and supervision, and has fulfilled the requirements for the submission of the thesis, which in our opinion has reached the requisite standard for the award of the degree.

The results contained herein have not been submitted in part or full to any other University or Institution for the award of any degree or diploma.

(Dr. A. K. Jha)
Associate Professor
Department of Applied Physics
Delhi College of Engineering
University of Delhi
Delhi-10042, India

(Prof. A. Trivedi)
Dean, Faculty of Technology
University of Delhi
Delhi-110042, India

Acknowledgements

Gratitude unlocks the fullness of life; it turns what we have into enough, and more; Gratitude makes sense of our past; it turns denial into acceptance; Chaos into order; Brings peace for today; and creates vision for tomorrow…….

"Melody Beattie"

As I reach this milestone in my research work, I am filled with gusto and grateful. I wish to express my deep sense of gratitude to ***Dr. A. K. Jha, Supervisor, Department of Applied Physics, Delhi Technological University, Delhi***, India for his guidance, keen interest, constructive criticism and suggestions throughout the course of the investigations. His dedication, suggestions and inexhaustible source of energy was a constant source of inspiration. I am grateful to him for showing me all the angles of research life.

I am thankful to Prof. A. Trivedi, Dean, Faculty of Technology, University of Delhi and Prof. P.B. Sharma, Vice- Chancellor, Delhi Technological University for their generous support and providing ample infrastructure to carry out the research work.

I would like to convey my extreme thanks to all the faculty members and technical staff of Department of Applied Physics for their support.

I would like to pay my thanks to ***Mr. Padmakshan & Rohtas (University of Delhi, Delhi)*** for carrying out X-Ray diffraction. I take the pleasure of thanking ***Mr. Vinod Kumar***, Delhi Technological University, Delhi who helped me for carrying out X-Ray diffraction and Scanning Electron Microscope.

I would also like to pay my thanks to ***Ministry of HRD, Govt. of India, New Delhi*** for the financial support during the whole research period.

When one owes to so many, it is almost impossible and invidious to single out names. I will always remain thankful to all my colleague and friends, who helped me

during the course of my research work. I acknowledge my friends ***Vidya, Arti, Rubal, Priya, Shruti, Venus, Sapna, Shakshi, Neelam, Suneet, Malya, oxyten, Yogesh, Mahamad Mohiddon, Ankita, Rakesh, Deshant*** for their cooperation, concern and encouragement in their own little ways actually pulled me through the tougher times.

I would also thanks to my seniors and juniors ***Sameer, Prasun, Neelam, Sugandha and Priyanka*** for their active support.

It will be very difficult for me to carry the whole research work without the strong support of my whole family, who all the way supported to me to proceed my research work besides all constraints and its only with their blessings and moral support that enabled me to finish this difficult task with an divine edge. I hearty acknowledge to my sincere gratitude to my ***beloved parents,*** my elder sister ***Gaytari,*** my ***jija ji*** and my younger brothers **Abhimannu,** and **Krishan** for their blessings, unconditional love and tremendous moral support. It's their wide adaptability, strong ethical support and faith in me to gain an easy outlook over the whole problem.

Last but not the least it could be incomplete without the gracious blessings and wishes from **God** that made to realize the truth and follow me to precede the right path for acquiring few pebbles of knowledge from its seashore.

Place: Delhi ***(Sheela Devi)***

Date:

Abstract

Pyroelectric crystals possess the unusual characteristic of being permanently polarized within a given temperature range. Unlike the more general piezoelectric materials that produce a polarization under stress, the pyroelectric materials develop the polarization spontaneously and posses permanent dipoles. The polarization also changes with temperature, hence, the term pyroelectricity. A subgroup of the spontaneously polarized pyroelectric materials is a very special category of materials known as ferroelectric materials. Similar to pyroelectric materials, materials in this group possess spontaneous dipoles; however, unlike pyroelectrics, these dipoles are reversible by an electric field of suitable magnitude less than the dielectric breakdown of the material. Thus, the two conditions necessary in a material to be classified as a ferroelectric material are:

(i) the existence of spontaneous polarization and

(ii) the ability to reverse the direction of polarization.

Ferroelectricity was discovered in Rochelle Salt ($KNaC_4H_4O_6.4H_2O$) in 1921 and then in polycrystalline Barium Titanate ($BaTiO_3$) around the middle of 1940s. Thereafter, large number of new materials have been discovered which show ferroelectricity that leading to a significant number of industrial and commercial applications. The prominent properties of ferroelectric materials such as polarization hysteresis, large dielectric constant and remarkable piezoelectric, pyroelectric and electro-optical effects makes them useful for a number of electronic devices like small size high capacitance capacitors, piezoelectric sonar, pyroelectric security surveillance

devices, medical diagnostic transducers, electrooptic light valves, ferroelectric memories, etc. Because of all these important applications, the field of ferroelectric materials is ever expanding. In the general group of ferroelectric materials, based on the basic structure, the following four types of ferroelectric materials are known:

(i) Tungsten-Bronze group

(ii) Perovskites group

(iii) Pyrochlore group

(iv) Bismuth Layer-Structured group.

The material chosen in the present work is from pervoskite group and is detailed below.

Barium Titanate ($BaTiO_3$)

Barium titanate is a well known ferroelectric material since 1940's. It is also one of the oxygen octahedron group of ferroelectric materials. In this structure Ba^{2+} ions occupy corners of a cube, O^{2-} ions occupy the centre of surface faces of the cube and at the centre of the cube small Ti^{4+} ion is located.

Barium titanate ($BaTiO_3$) has a paraelectric cubic phase above its curie temperature of about 120 ˚C. In the temperature range of 0 ˚C to 120 ˚C the ferroelectric tetragonal phase with c/a ratio ~1.01 is stable. Between -90˚C to 0˚C the ferroelectric orthorhombic phase is stable. On decreasing the temperature below -90˚C phase transition from orthorhombic to ferroelectric rhombohedral phase leads to polarization along one of the [111] cubic directions.

Among the ferroelectric materials, the perovskite materials like $BaTiO_3$, are widely used as capacitors, ultrasonic transducers, dynamic random access memories (DRAMs), non-volatile ferroelectric random access memories, infrared sensors,

pyroelectric infrared sensors etc. It shows positive temperature coefficient (PTC) of resistance. Due to PTCR properties, barium titanate is very often used as thermistors, e.g., in thermal switches. After an extensive literature surveys, in Journals like Materials Science, Ceramic International, Journal of European Ceramics Society, Ferroelectrics, Journal of Inorganic Materials, Solid State Communication, Physica B, etc. it was felt that although a lot of work has been reported for both A- as well as B-site substitutions in the Barium Titanate, however, extensive study of the changes in physical properties due to the systematic substitution of the tungsten in the barium (strontium) titanate materials is lacking, prompting this candidate to undertake the present work.

In the present work, a systematic B-site substitution in barium (strontium) titanate was undertaken and their properties were investigated. The chemical formulas for the studied compositions are:

Series 1: $BaTi_{0.85}W_{0.15}O_3$ for optimization of synthesis parameters

Series 2: $Ba(Ti_{1-x}W_x)O_3$ x = 0.0, 0.05, 0.15, 0.30

Series 3: $Ba_{0.8}Sr_{0.2}(Ti_{1-x}W_x)O_3$ x = 0.0, 0.05, 0.075, 0.1, 0.15, 0.30.

All the samples were prepared by solid state reaction method at the optimized sintering conditions and studied for their structural, dielectric, ferroelectric, piezoelectric, dc conductivity and impedance properties.

Also, Barium titanate and $BaTi_{0.95}W_{0.05}O_3$ were synthesized by mechanical activation technique by using planetary ball-mill and its structural and electrical properties have been investigated.

List of Figures

Contents

Chapter 1

Chapter 1

Introduction

1.1 General Background

Materials have been the milestones of progress of mankind. All civilizations have been categorized by the materials they used; the stone age, the bronze age, the steel age etc. Some of these periods in history lasted centuries but in recent times both the rate of major materials breakthroughs and their improvements are happening rapidly. During the 20^{th} century, virtually every aspect of the human life, from clothing to construction, changed profoundly by new materials. High performance materials made possible some of the century's most dazzling technological achievements: airplanes and spacecraft, microchips and magnetic disks, lasers and the fiber-optic highways. Behind all these are the ability of scientists and engineers to customize the materials for particular applications by manipulating its composition and microstructure: they start with a requirement and develop a material that meet the requirement. There are three major classes of materials metals, polymers and ceramics. The combination of two or more of these materials together to produce a new material whose properties would not be attainable by conventional means is called a composite. In the last half century, the growth of materials technology has been explosive, and its impact on our daily lives pervasive. The use of plastics is now so widespread that it is difficult to imagine life without them. Today, metals unknown in ancient times, such as aluminum and titanium, play a leading role in modern technology. These metals are widely used, for instance, in the aircraft industry because of their low densities and high resistance to corrosion. The ceramics which were the first engineering materials,

finding application as building materials and pottery in the stone age, recent technological advances combined with their unique electrical properties, hardness, durability and heat resistance are making ceramics the material of the future. One of the most recent Nobel Prizes for Physics was awarded to Bednorz and Mueller of IBM for the discovery that certain complex ceramic materials which conduct electricity without resistive loss at temperatures substantially higher than those for conventional metallic superconductors.

Beginning with the invention of the transistor in the 1950's, the electronics revolution, enabled by advances in materials, has dramatically and irreversibly changed our lives. The electrical industry and its flourishing daughter the electronic industry, uses a great variety of dielectric and insulating materials and they have constantly evolved over the years by the development of new and better materials. Ni-Zn and Mn-Zn ferrites found increasingly widespread use as transformer and coil core materials in telephones and in radio receivers in early 1920's. Some other electroceramics exhibit optical phenomena, such as luminescence (useful in fluorescent lighting) and lasing (exploited in lasers) and still others exhibit changes in optical properties with the application of electric fields and are therefore used extensively as modulators, demodulators and switches in optical communications. Perhaps, nowhere has the promise of ceramics been more tantalizing than in the quest for materials called superconductors, which can carry electric current with zero resistance. The applications of these materials have even spread into the medical field. Surgeons are already using bioceramic materials for repair and replacement of human knees, shoulders, elbows, fingers, eyes and wrists.

The discovery of the unusual dielectric properties of a number of simple mixed oxides which crystallize with the perovskite structure in early 1940's lead to a new era of ferroelectric ceramics industries. Ferroelectric oxide ceramics are used in a very broad range of functional ceramics and form the materials base for the many electronic applications. These electronic applications accounted for more than 60% of the total high technology ceramics market worldwide in 1990 itself [1]. From then the development in the electroceramics field is continuously increasing promoting growth of electroceramic industries.

1.2 History of Development of Ferroelectric Materials

The history of ferroelectrics can be traced back to Rochelle or Siegnette salt (Sodium potassium tartrate tetrahydrate, $NaKC_4H_4O_6.4H_2O$), which was discovered more than 400 years ago, initially for medicinal purpose. In this material ferroelectric properties were discovered subsequently by Joseph Valasek in 1921 [2]. The new effect discovered by Valasek was a dielectric hysteresis which resembled ferromagantic hysteresis loop. It is this analogy with ferromagnetism that ferroelectricity owes its name. Before this discovery, ferroelectricity was only a hypothetical property of solid materials at the turn of the 20^{th} century. However, the practical application of this material was largely limited due to its water solubility. It was after the discovery of ferroelectric ceramics that this class of materials became extremely useful for a variety of applications.

The first ferroelectric ceramics material was barium titanate ($BaTiO_3$), which was discovered in the mid 1940s [3-5]. During the World War II, there was pressing needs for high dielectric constant materials to fabricate high capacitance capacitors.

Before publications were available in the literature, $BaTiO_3$ has already been studied as a high dielectric constant material. Shortly thereafter, ferroelectricity was reported in this material by Wul and Goldman in 1945 [6].

The history of ferroelectric ceramics also includes the report of lead zirconate titanate (PZT) piezoelectric ceramics, the development of transparent electrooptical lead lanthanum zirconate titanate (PLZT), the research on lead magnesium niobate ($PbMg_{1/3}Nb_{2/3}O_3$ or PMN) relaxor ferroelectric ceramics and the discovery of many other non- pervoskite ceramics [3, 5].

1.3 Dielectrics

Dielectrics are insulating materials, in which the electrons are bound to their parent atoms/molecules and thus ordinarily do not contain any free charge carriers for conduction [7]. Even with a small applied voltage or thermal energy at normal temperature, electrons are not free for conduction. However, they do contain positive and negative charges, as usual; they are bound together and can be affected by a strong applied electric field. In certain dielectric materials, caller polar dielectrics, the constituent atoms are ionized to a certain degree and contain positively and negatively charged ions [8]. Dielectric materials offer a very high resistance to the passage of electric current and therefore differ in their basic electrical properties from conductive materials [9]. An applied electric field produces an electric current in a conducting material while in the case of dielectrics the applied field redistributes the charge with the material [10]. When a sufficient electric field is applied, cations are attracted to the cathode and anions to the anode due to electrostatic attraction and the electron clouds get deformed, forming electric diploes [8]. A material is said to be polarized

when the centre of positive charges do not coincide with that of negative charges and the phenomenon is known as polarization of the dielectric. Since in general, dielectric materials contain both bound and smaller number of mobile charges, applied electric fields produce both current and polarization.

1.3.1 General Properties of Dielectrics

1.3.1.1 Dielectric Polarization

The most important property of dielectrics is their ability to get polarized when an external electric field is applied. The phenomenon of polarization leads to the alignment of the dipoles of the dielectric and it acquires an *electric dipole moment* **p** [9]. From a macroscopic point of view, the negative charges of the dielectric material are displaced relative to the positive charges and the material is said to be polarized [10].

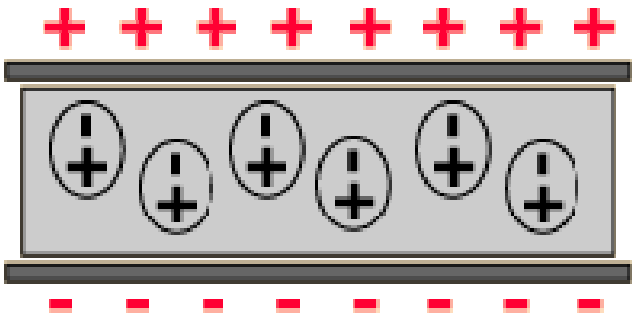

Fig. 1.1 Dielectric polarization

The state of dielectric acted upon by an electric field can be described by two vector quantities: intensity of the *applied electric field* **E** and the *polarization vector* **P**. The magnitude of polarization **P** of a dielectric numerically describes the phenomenon of polarization of a dielectric in an external electric field. In the absence of an external electric field each volume element of the dielectric has no electric dipole moment because the algebraic sum of the dipole moment in each volume

element of the dielectric is equal to zero [11]. The action of an external electric field forces the charges of the molecules of the dielectric into a certain ordered arrangement in space, as is schematically shown in Fig.1.1. In such a case each volume element of dielectric will have an dipole moment other than zero and equal to the vector sum **Σp** of the moments of all the polarized molecules present in this volume element. The polarization **P** can be expressed quantitatively as the sum of the electric dipole moment per unit volume,

$$\mathbf{P} = \frac{\sum p}{V} \tag{1.1}$$

Apart from the vector quantity ***P*** and ***E*** mentioned above, the macroscopic behaviour under static or low frequency conditions can also be described by another quantity – electric displacement vector **D** [12].

Compared to air-filled capacitors, dielectric capacitors can store more electric charge due to the dielectric polarization **P.** The physical quantity corresponding to the stored electric charge per unit area is called the electric displacement **D**, and is related to the electric field **E** by the following expressions [12]:

$$\mathbf{D} = \varepsilon_r \varepsilon_o \mathbf{E} \tag{1.2}$$

$$\mathbf{D} = \varepsilon_o \mathbf{E} + \mathbf{P} \tag{1.3}$$

Comparing Eqs. (1.2) and (1.3), we get the relation between P and E for an isotropic materials as:

$$P = \varepsilon_0 (\varepsilon_r - 1) E = \varepsilon_o \chi_e E \tag{1.4}$$

where ε_o is the permittivity of the free-space = 8.854 x 10^{-12} F/m and ε_r the relative permittivity. The quantity (ε_r - 1) is termed as the electrical or dielectric susceptibility χ_e.

Microscopic basis of Dielectric Polarization

Permittivity is essentially a macroscopic description of the properties of a dielectric [13]. To understand exactly what is happening inside the material when an electric field is applied, we have to link the permittivity to atomic or molecular mechanisms that describe the process of polarization of the material [13]. On the macroscopic scale we defined the polarization $\boldsymbol{P}$ to represent the bound charges at the surface of the material. Polarization reduces the effective electric field inside the material. If the polarizing entities in a solid are close enough to each other, the field component due to induced polarization can help produce dipoles [10]. Strictly, the induced polarization depends on the actual field experienced by the individual molecule and it is different from the applied field $\boldsymbol{E}$ [11]. As depicted in Fig. 1.2, when one moves through the dielectric, the field is not constant but its value depends not only on the charges on the plates but also on the orientations of all the other dipoles around the point of consideration in the dielectric.

The actual field experienced by a molecule in a dielectric is the *local field* $\boldsymbol{E}_{\text{loc}}$. The microscopic polarization response, described by direct analogy to Eq. (1.4), is proportional to the $\boldsymbol{E}_{\text{loc}}$ at the site of the polarizing entity [10] and is expressed as:

$$\boldsymbol{P} = \varepsilon_o \chi_e \boldsymbol{E}_{\text{loc}} \tag{1.5}$$

The simplest case that illustrates this important concept is that of a spherical unit within a crystal having a simple cubic lattice; the local field $\boldsymbol{E}_{\text{loc}}$ acting on a molecule increases with polarization as [11]:

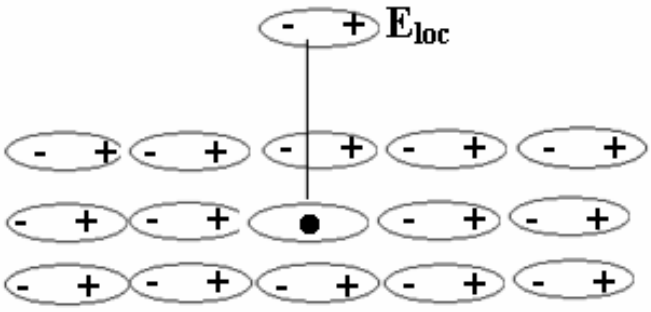

Fig. 1.2 Local electric field inside a polarized dielectric at the atomic scale

$$E_{loc} = E + \frac{P}{3\varepsilon_o} \tag{1.6}$$

The induced polarization in the molecule now depends on this local field $\boldsymbol{E}_{\text{loc}}$ rather than the average or applied field $\boldsymbol{E}$. Thus,

$$\mathbf{p}_{\text{induced}} = \alpha \boldsymbol{E}_{\text{loc}} \tag{1.7}$$

where the constant α is called polarizability. Thus, the polarizability of an atom is the ratio of the average dipole moment induced in a unit volume of the dielectric to the effective local field. Polarizability reflects the properties of an individual atom/molecule of a matter and not of a certain very large volume of it and is the most important microscopic electrical parameter of a dielectric [7]. For a dielectric containing N atoms or molecules per unit volume, the total dipole moment or polarization $\boldsymbol{P}$, is equal to

$$\boldsymbol{P} = \text{N}\,\alpha\,\boldsymbol{E}_{\text{loc}} \tag{1.8}$$

Using Eqs. (1.4), (1.6), (1.7) and (1.8), we can obtained a relationship between ε_r and α. This is the **Clausius - Mossotti equation** [7, 14] expressed as:

$$\frac{\varepsilon_r - 1}{\varepsilon_r + 2} = \frac{N\alpha}{3\varepsilon_o} \tag{1.9}$$

This equation relates a macroscopic quantity relative permittivity or dielectric constant (ε_r) to a microscopic quantity the polarizability (α).

1.3.1.2 Types of polarization

In general, there are four different types of polarization which contribute to the dielectric response [14]:

Fig. 1.3 shows schematically the origin of the electric polarization. The total polarization in a material is the sum of four different types of polarization mechanisms, namely, electronic, ionic, dipolar and space charge polarizations. The degree to which each mechanism contributes to the overall polarization of the material depends on the frequency of the applied field in addition to the nature of the material [8, 12-13].

In general, any or all of the above mentioned mechanisms of polarization may be operative in a material. In an alternating field, the dipoles can reverse alignment with each reversal of the field. For an assembly of dipoles in a dielectric the same will apply; the polarization reversing in accordance with the direction of the applied electric field. Thus, the total polarization, the total polarizability and relative permittivity will depend on the ease with which the direction of the alignment of dipoles can be reversed. If the frequency of the field is increased, a point is reached when, because of their inertia, the dipoles cannot keep up with the oscillating applied electric field and the reversal (switching) of the polarization lag behind. This corresponds to a reduction in the polarization produced by the field, which results in the reduction in the permittivity of the material. Ultimately, as the frequency of the applied field increases, the dipoles will barely have started to move before the field reverses and then try to move other way. At this frequency the field is producing virtually no polarization in the dielectric. This process is generally called relaxation and the frequency beyond which the polarization no longer follows the field is called the relaxation frequency (Fig. 1.4). If the frequency of the applied field exceeds the relaxation frequency of a particular polarization process, the dipoles never reach an

equilibrium state, i. e., cannot reorient fast enough with the field direction and the polarization mechanism ceases to contribute to the overall polarization [15]. The followings are various polarization mechanisms:

(i) **Electronic polarization:** The electronic polarization occurs due to the displacement of the negatively charged electrons with respect to the positively charged core. The electronic polarizability α_e is approximately proportional to the volume of the electron shell [12]. In general α_e is temperature independent and large atoms have a large electronic polarizibality. Electronic polarization can follow alternating fields with frequency up to THz-PHz (10^{12}-10^{15} cycle/second, higher than visible light frequencies) [8].

(ii) **Ionic polarization:** The ionic polarization involves the displacement of ions (cations and anions) within the crystal under an applied electric field. It depends on the crystal structure. The ionic polarizibality is denoted by α_i. The ionic polarization responds up to GHz-THz (10^9-10^{12} cycle /sec, microwave frequency region).

(iii) **Orientation (or Dipolar) polarization:** This polarization occurs due to the alignment of permanent pre-existing dipoles. At ambient temperatures, usually all dipole moments have statistical distributions of their direction [15]. An electric field generates a preferred direction for the dipoles, while the thermal movement of the atoms perturbs the alignment. This polarization occurs generally in liquids and solids which have asymmetric molecules with permanent dipole moments. The dipole orientation can follow up to GHz (10^9 cycle/sec).

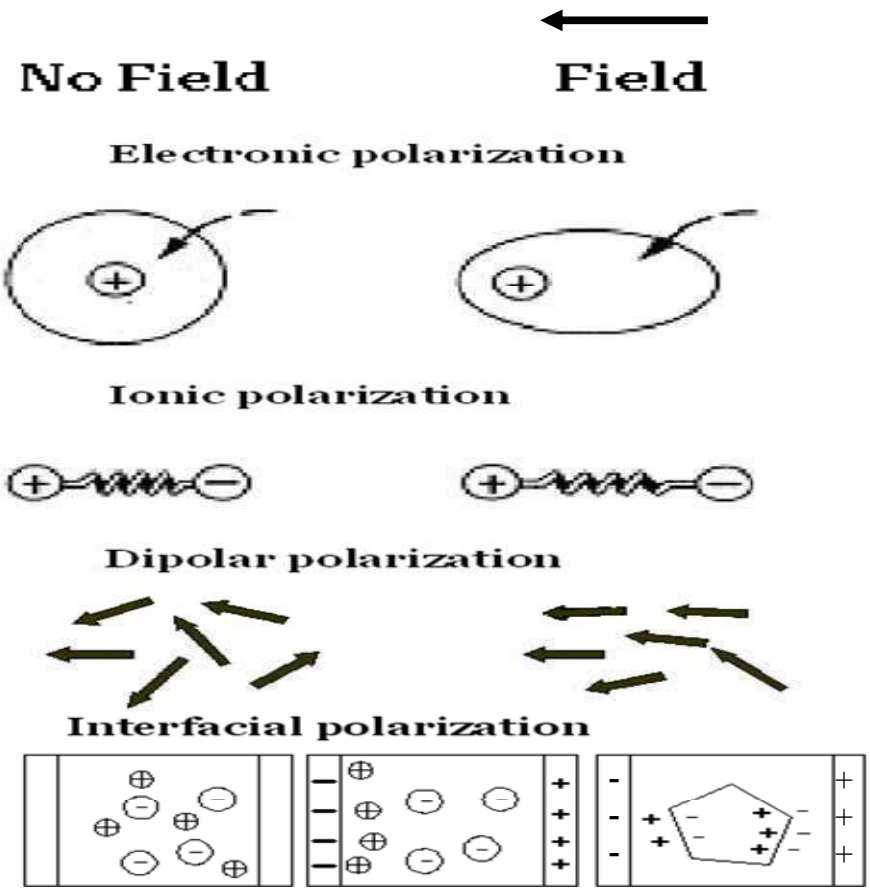

Fig. 1.3 Microscopic origins of the electric polarization

(iv) **Space charge polarization:** This type of polarization exists in dielectric materials having multiphasic structure and which show spatial inhomogeneities of charge carrier densities. In a real crystal there exist a large number of defects such as impurities centres, dislocations and so on. Free charge carriers, migrating through the crystal under the influence of an applied field may be trapped by or pile near a defect. This results in localized accumulation of charges that induce its image charges on an electrode and give rise to a dipole moment. This is called interfacial or space–charge polarization. The relaxation frequencies can be as low as 100 Hz- 1 kHz [12, 16]. In some cases it is known to exceed up to 100 kHz too [12].

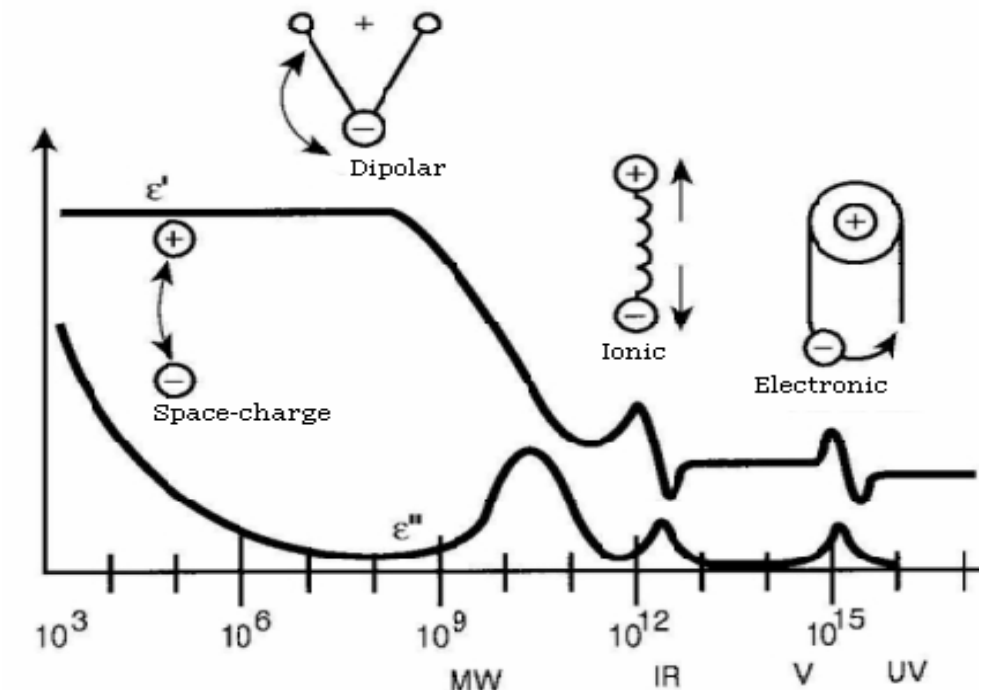

Fig. 1.4 Frequency dependence of the real and imaginary parts of dielectric

The total polarization of dielectric material results from all the components mentioned above. Accordingly, the total polarizability is the sum of individual polarizabilities and is expressed as:

$$\alpha = \alpha_e + \alpha_i + \alpha_o + \alpha_s \qquad (1.10)$$

where α represents the total polarizability and α_e, α_i, α_d and α_s are the polarizability of the respective polarization mechanisms; electronic, ionic, dipolar and space charge polarizations.

1.3.1.3 Dielectric Constant and Dielectric Loss

Dielectric Constant

A material is classified as "dielectric" if it has the ability to store energy when an external electric field is applied. If a DC voltage V is applied across a parallel plate capacitor (Fig. 1.5), more charge is stored when a dielectric material is placed in

between the plates than that when vacuum exists between the plates. The dielectric material increases the storage capacity of the capacitor by neutralizing charges at the electrodes, which ordinarily would contribute to the external field. The capacitance of the dielectric material is related to dielectric constant [11], as indicated in the following equations:

$$C_o = \frac{A}{d}\varepsilon_o \tag{1.11}$$

$$C = C_o\, \varepsilon_r \tag{1.12}$$

where C_o and C are capacitances without and with dielectric, ε_r is the relative permittivity for dielectric constant of the dielectric medium and A and d are the area of the capacitor plates and the distance between them respectively.

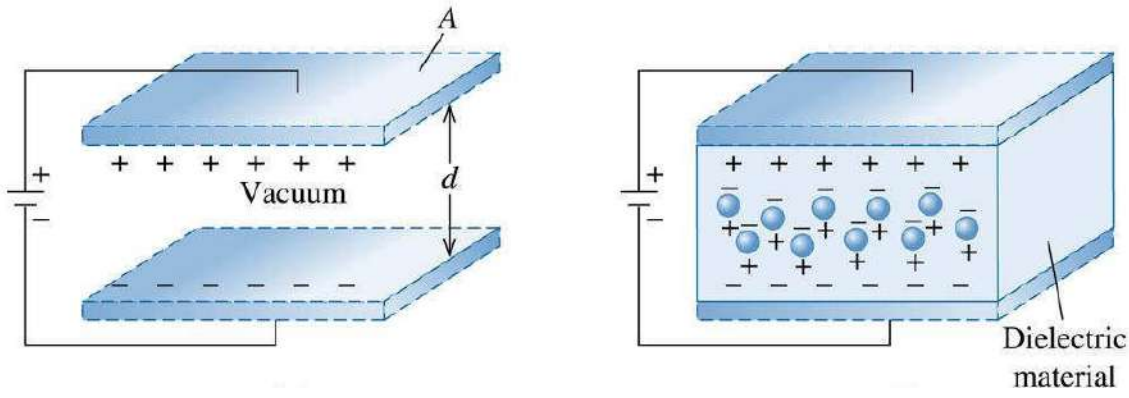

Fig. 1.5 Parallel plate capacitor under DC electric field

Dielectric Loss

When an electric field acts on any matter the latter dissipates a certain amount of electrical energy that transforms into heat energy and this phenomenon is commonly known as the "loss" of power [16]. The dielectrics display a characteristics feature: under a given voltage the dissipation of power in these dielectrics depends on the voltage frequency. The loss of power at an alternating voltage is markedly higher than

at a direct voltage, and rapidly grows with increasing frequency of voltage and also depends on the nature of the dielectric material. These basic properties were established for the first time in 1886 by the Russian physicist I. Borgman [9].

The magnitude of the loss in a dielectric under the action of an applied voltage is commonly known as *dielectric loss*. The energy loss that occurs in dielectrics is due to dc conductivity and dipolar relaxation [9].

When complex permittivity is drawn as a simple vector diagram (Fig. 1.6), the real and imaginary components are 90° out of phase. The vector sum forms an angle δ with the real axis (ε'_r), which can be mathematically expressed by a complex dielectric permittivity:

$$\varepsilon_r = \varepsilon'_r - j\,\varepsilon''_r \qquad (1.13)$$

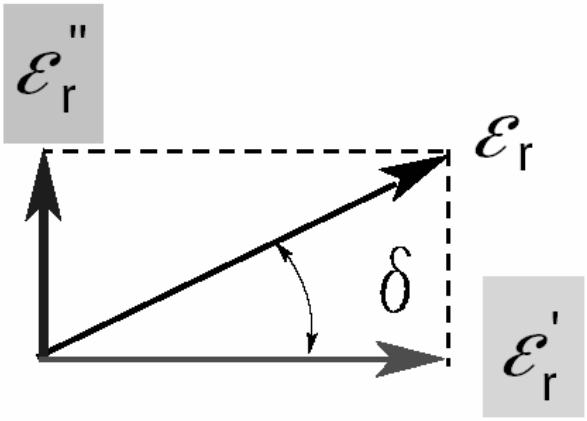

Fig. 1.6 Loss tangent vector diagram

The loss tangent or tan δ is defined as the ratio of the imaginary part of the dielectric constant to the real part. The dissipation factor is denoted by D and Q is used to denote the quality factor. The loss tangent tan δ is called tangent loss or dissipation factor. Sometimes the term "quality factor or Q- factor" which is the reciprocal of the loss tangent [9, 16], i.e.,

$$\tan\delta = \frac{\varepsilon_r''}{\varepsilon_r'} = \frac{1}{Q} = \text{ energy lost/stored per cycle} \qquad (1.14)$$

1.3.2 Classification of Dielectrics

The dielectrics can be classified into two classes [9]:

(i) **Polar dielectrics:** In the molecules of the polar dielectrics the centers of the positive and negative charges do not coincide with each other. They consist of molecules with non-zero dipole moment. They are of asymmetric shape.

(ii) **Non-polar dielectric:** In case of non-polar dielectrics, centers of positive and negative charges inside the molecule coincide. Dipole moment of individual molecules in non-polar dielectric is zero. These molecules are symmetric.

Experimental investigations of polar crystals have demonstrated that they can further be divided into *linear* and *nonlinear* dielectrics in accordance with their behaviour in electric fields [17], as discussed below.

Linear Dielectrics

The "*linear*" dielectrics are characterized by the property that their polarization ***P*** and electric displacement ***D*** are directly proportional to the intensity of the applied electric field ***E*** [9],

$$\mathbf{P} = \varepsilon_o \chi_e \mathbf{E} \text{ and} \qquad (1.15)$$
$$\boldsymbol{D} = \varepsilon_r \varepsilon_o \boldsymbol{E}$$

Thus, in such dielectrics the permittivity ε and the dielectric susceptibility χ_e do not depend on the intensity of the electric field. Therefore,

$$C = \varepsilon_r \varepsilon_o \frac{A}{d} \qquad (1.16)$$

i.e., the capacitance of the capacitor with a linear dielectric does not depend on the voltage V applied to the capacitor while the charge

$$Q = CV \qquad (1.17)$$

of the capacitor is directly proportional to the voltage applied to it.

Nonlinear Dielectrics

The electric polarization of nonlinear dielectrics is a nonlinear function of the applied electric field. The most important materials among nonlinear solid dielectrics are *ferroelectric materials*, which can exhibit (in a limited range of temperature) a spontaneous polarization $\mathbf{P_s}$ in the absence of an applied electric field and which has spontaneously polarized regions known as domains [17].

1.4 Ferroelectricity

Ferroelectricity [18, 19] is the phenomenon, by virtue of which some materials exhibit spontaneous electric polarization even in the absence of any externally applied field. Ferroelectric crystals possess regions with uniform polarization called ferroelectric domains. Within a domain, all the electric dipoles are aligned in the same direction. The number of distinct spontaneous polarization directions in a ferroelectric material depends on its symmetry point group.

The ferroelectric properties of a ferroelectric material disappear above a critical temperature T_c; this temperature is called the ferroelectric Curie temperature, where material becomes paraelectric [20]. The phase transition from ferroelectric to the paraelectric phase is associated with anomalies in the physical properties like specific heat, dielectric constant, spontaneous polarization, etc. The ferroelectric structure has a lower symmetry than the nonpolarized state; thus, at the transition temperature a change in the crystal structure is observed [20].

1.4.1 Phenomenology of Ferroelectricity

The interpretation of ferroelectric properties is based on one hand on the thermodynamic considerations that is independent of any particular model; on the

other hand, theories have been developed on the basis of atomic models. The latter requires for their verification detailed studies of the structure of the crystal as a function of temperature [20].

About ten years ago, it was believed that there were two different types of ferroelectric transition mechanism: displacive type and order-disorder type [14]. However, many ferroelectric phenomena cannot be explained unequivocally by either displacive type mechanism or by order-disorder type mechanism [21].

Ferroelectric phase transitions can be described mathematically with some success by Landau theory, often called Landau- Devonshire theory, as a credit to Devonshire, who developed it specifically for the ferroelectric case. An exhaustive description of ferroelectric phase transitions has been given by Strukov and Lavanyuk [21].

Landau Theory of the Phase Transition

Based on the phase transition theory of Landau- Ginzburg [22-24], Devonshire [22, 25] developed a phenomenological theory of ferroelectricity by choosing the polarization **P** as order parameter [22]. It is convenient to treat the ferroelectric phase by choosing Gibbs function G as a state function of the ferroelectric system and the temperature **T** and polarization **P** as independent variables. Since the Gibbs free energy G is not changed by reversing the direction of the axes of the space coordinate system and is independent of the direction of the polarization **P**, G can be expressed in an power series of polarization

$$G(T) = G_o + \frac{1}{2}\alpha(T)^2 + \frac{1}{4}\beta(T)^4 + \frac{1}{6}\gamma(T)^6 + \ldots\ldots\ldots \quad (1.18)$$

where G_o is the elastic Gibbs free energy of the system when polarization P = 0 and the coefficients $\alpha, \beta, \gamma\ldots\ldots\ldots$ are function of T.

A stable state of the thermodynamic system is characterized by a minimum value of the free energy G. The conditions for a minimum of G are:

$$\frac{\partial G}{\partial P} = 0; \qquad \frac{\partial^2 G}{\partial P^2} \geq 0 \qquad \text{or} \qquad \frac{\partial E}{\partial P} = \chi^{-1} > 0 \tag{1.19}$$

where χ is susceptibility.

By combining Eqs. (1.18) and (1.19), the equation of the state for the ferroelectric system takes the form

$$P(\alpha(T) + \beta(T)P^2 + \gamma(T)P^4) = 0; \qquad \beta^2(T) - 4\alpha(T)\gamma(T) > 0 \tag{1.20}$$

$$\chi^{-1} = \alpha(T) + 3\beta(T)P^2 + 5\gamma(T)P^4 > 0 \tag{1.21}$$

Two roots can be found for the left side of Eq. (1.20). The first root P = 0 corresponds to a paraelectric phase and the second root P ≠ 0 to a ferroelectric phase [22].

Paraelectric Phase

When P = 0, then Eq. (1.21) becomes,

$$\chi^{-1} = \alpha(T) > 0 \tag{1.22}$$

Hence, we see that α must have a positive value when a stable state of the crystal is a paralectric phase. Expanding α (T) as a Taylor series in ($T-T_o$) and taking into a account only the first order- term, we have [22],

$$\alpha(T) = \alpha_o(T - T_o) \tag{1.23}$$

Combining Eqs. (1.22) and (1.23), we obtain

$$\chi = C[4\pi(T - T_o)]^{-1}, T > T_o \tag{1.24}$$

Where $C = \frac{4\pi}{\alpha}$. This is the Curie-Weiss law with C being the Curie-Weiss Constant.

Ferroelectric Phase

When $P \neq 0$, there are two situations corresponding to:

(a) second-order phase transition when $\beta > 0$, and

(b) first -order phase transition when $\beta < 0$.

Second-order (or continuous) phase transition ($\beta > 0$)

When β is positive, γ is often neglected [8]. Combining Eqs. (1.19) and (1.24), we get

$$\left(\frac{T - T_o}{\varepsilon_o C}\right)P + \beta P^3 = 0 \tag{1.25}$$

so that either $P = 0$ or $P^2 = \left(\frac{T - T_o}{\varepsilon_o \beta C}\right)$

For $T > T_0$, the unique solution $P = 0$ is obtained. For $T < T_0$, the minimum of the Landau free energy is obtained at:

$$P = \sqrt{\frac{(T_o - T)}{\beta \varepsilon_o C}} \tag{1.26}$$

The phase transition occurs at $T_c = T_o$ and the polarization reduces continuously to zero at this temperature; this is called a second-order transition. The relative permittivity ε is calculated as [8]:

$$\frac{1}{\varepsilon} = \frac{\varepsilon_o}{(\partial P / \partial E)} = \varepsilon_o(\alpha + 3\beta P^2) \tag{1.27}$$

Then,

$$\varepsilon = \frac{C}{T - T_o} \quad (T > T_o) \tag{1.28}$$

$$= \frac{C}{2(T - T_o)} \quad (T < T_o) \tag{1.29}$$

The variation of P and ε with temperature is shown in Fig. 1.7. P is a continuous function of temperature; a transition of this type is associated with a discontinuity in

the specific heat. Tri- glycine sulphate (TGS) exhibits a second- order ferroelectric phase transition.

First –order phase transition (β <0)

When β is negative and γ is positive, the transition is of first order. The equilibrium condition gives,

$$\frac{(T-T_o)}{\varepsilon_o C}P + \beta P^3 + \gamma P^5 = 0 \qquad (1.30)$$

This leads to either P = 0 or

$$P^2 = \left[-\beta + \sqrt{\frac{\beta^2 - 4\gamma(T-T_o)}{\varepsilon_o C}}\right] 2\gamma \qquad (1.31)$$

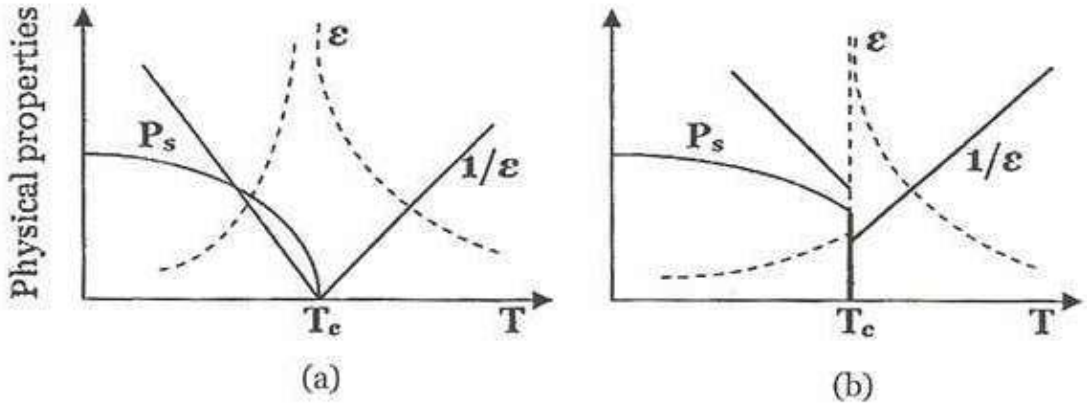

Fig. 1.7 Variation of P_s and ε with temperature in case of (a) second order and (b) first order phase transition

A transition from the non- polarized to a spontaneously polarized state occurs when the free energies of the paraelectic and ferroelectric phases are equal, i. e., G = 0. Therefore, we get

$$T_c = T_0 + \left(\frac{3}{16}\right)\left(\frac{\beta^2 \varepsilon_o C}{\gamma}\right) \qquad (1.32)$$

It is evident that the Curie temperature T_c is slightly higher than the Curie-Weiss temperature T_o and the polarization shows a discrete jump at the critical temperature from zero to some non-zero value, as shown in Fig. 1.7. Barium titante ($BaTiO_3$) is an example of a ferroelectric that undergoes a first-order phase transition.

1.4.2 General Properties of Ferroelectric Materials

1.4.2.1 Crystal Symmetry

The crystals are classified into 32 crystal categories (point groups) according to the symmetry elements it possesses [26]. Out of these 32 classes i.e., point groups, 11 are centrosymmetric and do not posses polar properties [27-28]. The remaining 21 do not posses centre of symmetry, i. e., they are non-centrosymmetric and therefore posses one or more polar axes. Of these, 20 classes are piezoelectric (the one exception is cubic class 432) (Fig. 1.8). Piezoelectric crystals have the property that the application of mechanical stress induces polarization and conversely the application of an electric field produces structural deformation. Of the 20 piezoelectric classes, 10 have a unique polar axis and are spontaneously polarized, i. e., they are polarized even in the absence of an externally applied electric field. Crystals belonging to these 10 classes are called pyroelectric because their polarization vary with temperature. Ferroelectric crystals belong to the pyroelectric family. They additionally also exhibit the property that the direction of the spontaneous polarization can be reversed by the application of a suitable electric field. Therefore, materials that can be defined as ferroelectrics must have two characteristics: the presence of spontaneous polarization and reversibility of the polarization under electric field [3, 4].

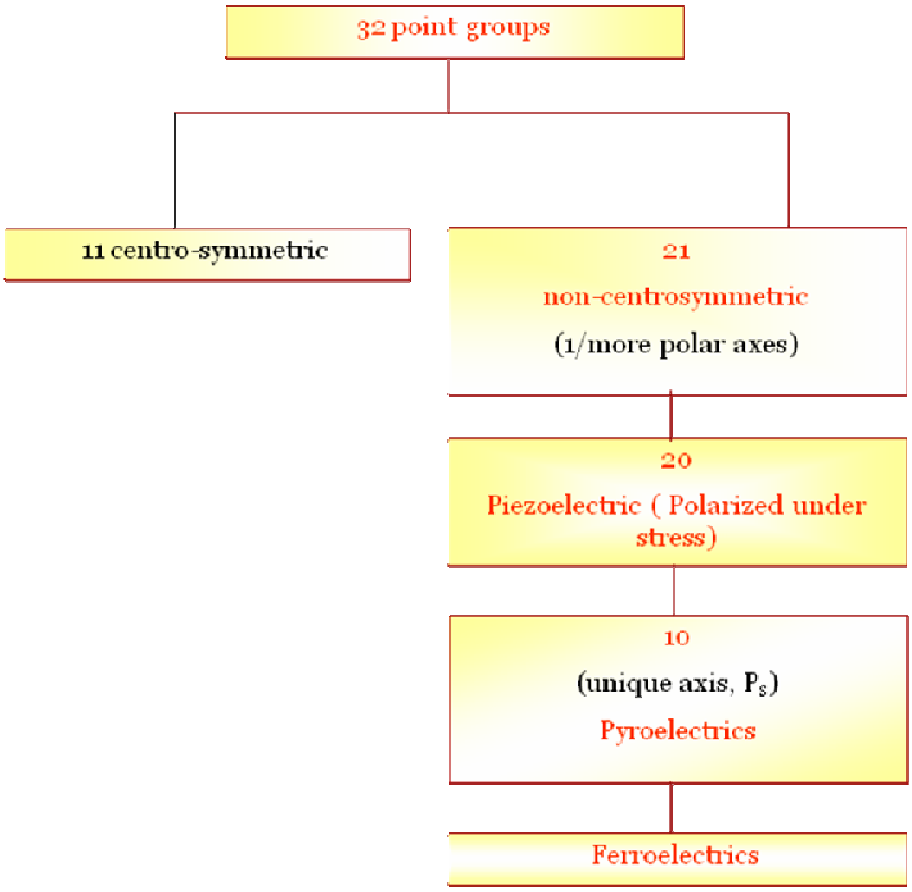

Fig. 1.8 Classification scheme on the basis of crystal symmetry

1.4.2.2 Spontaneous Polarization and Pyroelectric Effect

The spontaneous polarization is the value of the dipole moment per unit volume or by the value of the charge per unit area on the surface perpendicular to the axis of spontaneous polarization. The axis of spontaneous polarization is usually along a given crystal axis. Although a crystal with polar axes (20 non-centrosymmetric point groups) shows the piezoelectric effect, it is not necessary that they have a spontaneous polarization. It could be due to the cancelling of the electric moments along the different polar axes to give a zero net polarization [29]. Only crystals with a unique polar axis (10 out of 21 non-centrosymmetric point groups) show a spontaneous polarization *(P_s)* along this axis. When the value of the

spontaneous polarization depends on the temperature, this is called the pyroelectric effect which was first discovered in tourmaline by Teophrast in 314 B. C. and so named by Brewster in 1824 [30]. Pyroelectric crystals show a spontaneous polarization in a certain temperature range. If the magnitude and direction of $\boldsymbol{P_s}$ can be reversed by an external electric field, then such crystals are said to show ferroelectric behavior. Hence, all single crystals and poled ceramics which show ferroelectric behavior are pyroelectric, but not vice versa. For example, tourmaline shows pyroelectricity but not ferroelectricity.

1.4.2.3 Ferroelectric Domains

In general, the direction of spontaneous polarization is not the same throughout a ferroelectric crystal; certain regions are polarized in one direction, others in a different direction. In other words, alignment of the electric dipoles may extend only over a region of the crystal, while in other regions the direction of the spontaneous polarization may be in other direction. Such regions having the same direction of polarization are referred to as *domains*. The boundaries between domains are called *domain walls*. A ferroelectric crystal has multiple ferroelectric domains. A single domain can be obtained by domain wall motion, made possible by the application of an appropriate strong electric field. An enough strong electric field can reverse the direction of polarization in the domain and the process is known as domain switching [31- 32].

1.4.2.4 Hysteresis Loop

A ferroelectric material is spontaneously polarized, i.e., it is polarized in the absence of an external field. The direction of the spontaneous polarization, known as *polar axis*, may be altered under the influence of an applied electric field. In general

the direction of spontaneous polarization is not the same throughout the macroscopic crystal [20].

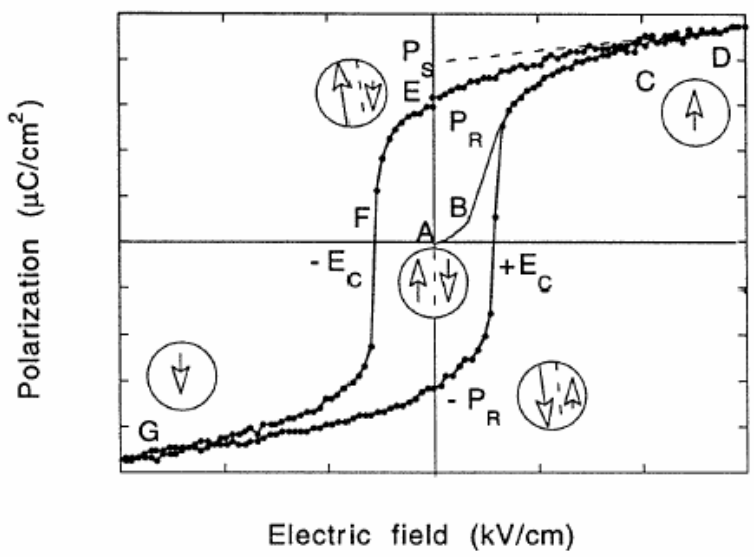

Fig. 1.9 Polarization vs. Electric Field (P-E) hysteresis loop for a ferroelectric crystal

Rather the crystal consists of a number of domains; within each domain the polarization has a specific direction, but this direction varies from one domain to another. On the basis of the domain concept, the occurrence of hysteresis in P versus E relationship can be explained as follows:

With reference to the Fig.1.9, consider a crystal which initially has an overall polarization equal to zero, i.e., the sum of the vectors representing the dipole moments of the individual domains vanishes. When an electric field is applied to the crystal, the domains with polarization along the applied field direction grow at the expense of the "antiparallel" domains, increasing the polarization (AB). As the applied field is increased, the polarization increases. When all domains are aligned in the direction of the applied field (CD), the polarization saturates and the crystal consists of a single domain. The extrapolation of the linear part CD to zero external field gives the

spontaneous polarization $\mathbf{P_s}$. When the applied field for a crystal corresponding to point D in the figure is reduced, the polarization of the crystal decreases, but for zero applied fields there remains the *remanent polarization* $\mathbf{P_r}$ (AE) in Fig. 1.9 where $\mathbf{P_r}$ refers to the crystal as a whole. When the field is reduced to zero, some of the domains remain aligned in the positive direction and the crystal exhibits remanent polarization [26]. In order to remove the remanent polarization, a field in the opposite direction needs to be applied. The field required to make the polarization zero (AF) again is called the *coercive field* $\mathbf{E_c}$. Further increase of the field in the negative direction cause complete alignment of the dipoles in the opposite direction (FG), and the cycle can be completed by reversing the field direction once again. It is evident that if the coercive field is larger than the breakdown field of the crystal, no change in the direction of spontaneous polarization can be achieved. The relation between **P** and **E** is thus represented by a hysteresis loop, which is the most important characteristic of a ferroelectric crystal.

1.4.2.5 Curie Temperature and Phase Transition

All ferroelectric materials are characterized by a transition temperature called Curie temperature *(T_c)*. At a temperature $T \geq T_c$, they do not exhibit ferroelectricity. On decreasing the temperature through the Curie point, a ferroelectric crystal undergoes a phase transition from a non-ferroelectric (paraelectric) phase to a ferroelectric phase. If there are more than one ferroelectric phases, the temperature at which the crystal transforms from one ferroelectric to another is called the transition temperature. Early research work on ferroelectric transitions has been summarized by Nettleton [33,34]. Near the Curie temperature or transition temperature, thermodynamic, dielectric, elastic, optical and other properties show an anomalous

behavior. This is due to a distortion in the crystal structure due to phase change. The temperature dependence of the dielectric constant above the Curie temperature ($T > T_c$) in ferroelectric crystals is governed by the Curie-Weiss law:

$$\varepsilon = \varepsilon_o + \frac{C}{T - T_o} \tag{1.33}$$

where ε is the permittivity of the material, ε_o is the permittivity of free space, C is a constant called the Curie constant and T_o is the Curie temperature. The Curie temperature T_o is different is different from the Curie point T_c. T_o is a constant obtained by extrapolation, while T_c is the actual temperature where the crystal structure changes. For the first order transitions, $T_o < T_c$; while for the second order phase transitions $T_o = T_c$ [35].

1.4.3 Classification of Ferroelectric Materials

Ferroelectric materials can be classified on the basis of:

(1) The mechanism of the appearance of spontaneous polarization, and

(2) The crystal structure.

(1) The mechanism of the appearance of spontaneous polarization

There are two mechanisms under this category as discussed below.

(a) **Displacive type:** In this case, a rearrangement of the structure, due to the displacements of certain ions, produces spontaneous polarization. The direction of spontaneous polarization coincides with the direction of the displacement. The polarization of such ferroelectrics is usually associated with the displacement of a cation from the centre of the surrounding oxygen octahedron. Depending on the geometry of the structure (e.g., dimensions, positions of the ions, etc.), the nature of the binding and the electronic

configuration of the atoms, the resulting dipole moments are oriented either parallel or antiparallel in a given structure. Barium titanate and most of the oxide ferroelectrics fall under this category [14, 17].

(b) **Order-disorder type:** Certain ferroelectric materials exhibit a transition which involves the ordering of certain structure elements which were disordered before the transition. The polarization process in these ferroelectrics can be considered to take place in two stages: the appearance of dipoles due to the deformation of the atomic groups and the alignment (to produce a parallel or antiparallel orientation) of dipole moments due to the ordering of the structure elements. The ordering mechanism acts as a "trigger" for the induction of ferroelectric. e.g. in KH_2PO_4, tri- glycine sulphate (TGS).

(2) The crystal structure

On the basis of crystal structure, the ferroelectric materials can be classified into the following four subcategories.

Corner - Sharing Oxygen Octahedral

A large class of ferroelectric crystals is made up of mixed oxides containing corner sharing octahedral of oxygen ions. Inside each octahedron is a cation B^{b+} where 'b' varies from 3 to 6. The space between the octahedral are occupied by A^{a+} ions, where 'a' varies from 1 to 3. The corner sharing oxygen octahedral includes pervoskite type compounds, tungsten bronze type compounds, bismuth oxide layer structured compounds and lithium niobate and tantalate.

(a) **Pervoskite:** Pervoskite is a family name of a group of materials having a structure of the type ABO_3 e.g. calcium titanate ($CaTiO_3$) (Fig.1.10). Many piezoelectric (including ferroelectric) ceramics such as Barium Titanate

($BaTiO_3$), Lead Titanate ($PbTiO_3$), Lead Zirconate Titanate (PZT), Lead Lanthanum Zirconate Titanate (PLZT) etc., have a pervoskite structure.

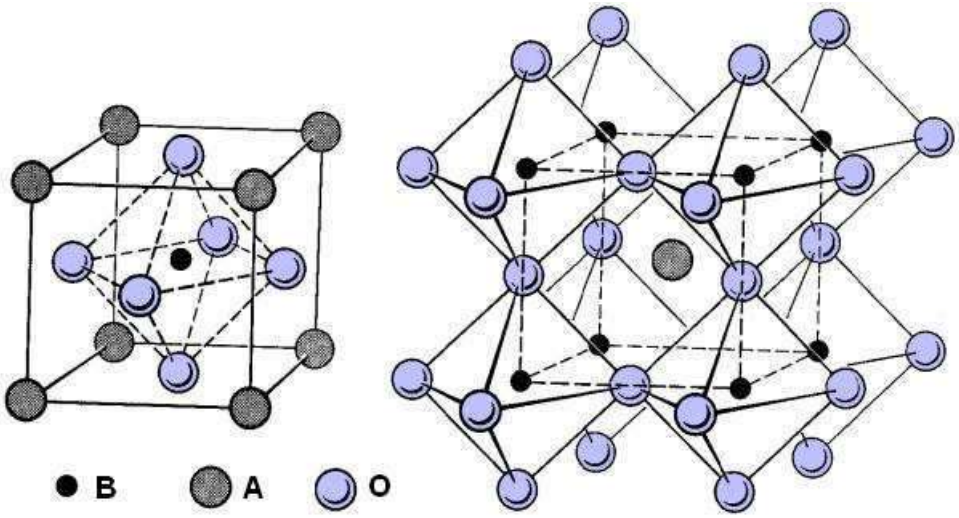

Fig. 1.10 Crystal structure of pervoskites

(b) **Tungsten-Bronze group:** Lead niobate ($PbNb_2O_6$) was one of the first crystals having the tungsten bronze type structure with ferroelectric properties. The site occupancy formula for this type of structure is given by $(A_1)_2(A_2)_4(C)_4(B_1)_2(B_2)_8O_{30}$ [36]. The open nature of this structure as compared to the pervoskite allows a wide range of cation and anion substitutions without loss of ferroelectricity [22, 37-38].

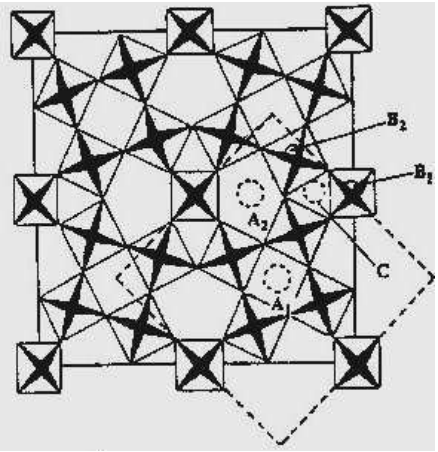

Fig. 1.11 Tungsten- bronze crystal structure

(c) **Bismuth oxide layer structured group:** The two important piezoelectric materials with the $(Bi_2O_2)^{2+}$ layer structure are Bismuth Titanate ($Bi_4Ti_3O_{12}$) and Lead Niobate ($PbBi_2Nb_2O_9$). As shown in Fig. 1.12, the structure consists of corner linked pervoskite–like sheets, separated by $(Bi_2O_2)^{2+}$ layers [39, 40]. The plate like crystal structure of these compounds leads to highly anisotropic ferroelectric properties. The bismuth oxide layer structured ferroelectric materials have the potential to become important piezoelectric ceramics because of their higher stability, higher operating temperature and frequency in addition to being Pb free. These ceramics are mainly useful for piezoelectric resonators which need to exhibit a very stable resonant frequency [35, 41-42].

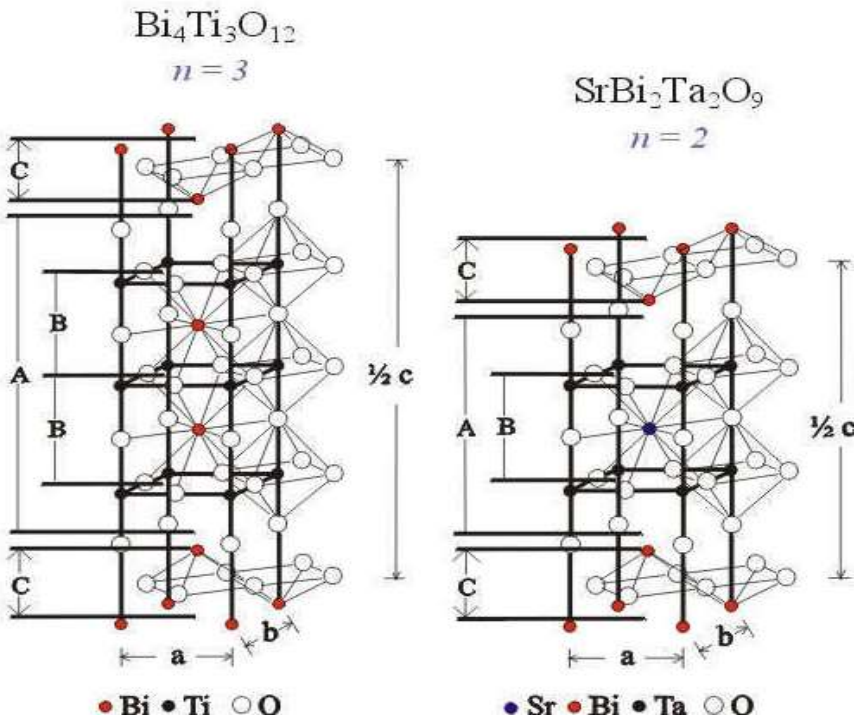

Fig. 1.12 Crystal structure of bismuth oxide layer structured (BLSF) materials

(d) **Pyrochlore group:** Members of this group have general formula $A_2B_2O_7$ and the crystal structure is shown in Fig. 1.13, where A – site can be represented by any of a long list of metal ions such as lead, calcium, potassium, bismuth, sodium, barium, calcium, cerium, etc. while the B-site can be represented by any of these metal ions like niobium, tungsten, tantalum, titanium, etc. The compositions like $Cd_2Nb_2O_7$, $Y_2Ti_2O_7$, $Mn_2Sb_2O_7$, etc. also belong to this family.

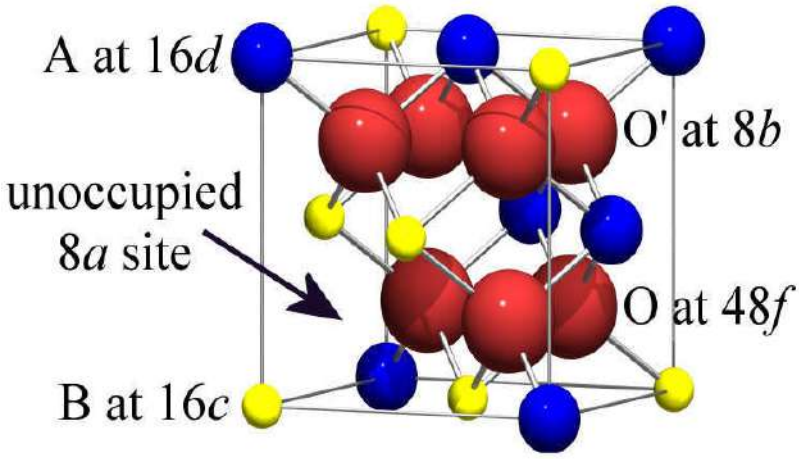

Fig. 1.13 Crystal structure of pyrochlore

1.4.4 Applications of Ferroelectric Materials

Ferroelectric materials are utilized in various devices such as high dielectric constant, pyroelectric sensors, piezoelectric devices, electro-optics devices, memories and PTC (positive temperature coefficient of resistivity) components. These applications exploit properties that are indirect consequences of ferroelectricity, such as dielectric, piezoelectric, pyroelectric and electro-optic properties. However, ferroelectric devices often fail to commercialize in areas of application where competitive materials exist. In the following sections, the applications have been discussed on the basis of the various properties.

(i) **Capacitors:** One of the major applications of ferroelectric materials is for capacitors, utilizing their high dielectric constants around the Curie temperature. A capacitor consists of a dielectric material sandwiched between two electrodes. The capacitance for a capacitor with a dielectric filling the space between the electrodes is given by Eq. (1.16). To get a high volumetric efficiency (capacitance per unit volume) the dielectric material between the electrodes should have a large dielectric constant, a large area and small thickness. The dielectric constant of $BaTiO_3$ is very high ~15,000 compared to 5 to 10 for common ceramics and polymers. The volumetric efficiency can be further enhanced by using multilayer ceramic (MLC) capacitors, which consists of alternate layers of dielectric and electrode material. Each individual dielectric layer contributes capacitance to the total capacitance. The high dielectric constants of the relaxor materials such as PMN ($\varepsilon \approx 25{,}000$) make them ideal for MLC capacitor applications [43, 44]. Another added advantage of ferroelectric materials is due to their nonlinear nature they can be used to make capacitors with tunable capacitance.

(ii) **Ferroelectric Memories:** Recently, very large scale integrated semiconductor memories using ferroelectric films have been investigated intensively. Utilization of ferroelectrics with high permittivity or polarization hysteresis has been considered as a possible solution to the problem of limitation in production of fine –scale capacitors using the conventional Si micromachining technology [8].

There are *volatile* and *non-volatile* memory devices in semiconductor memories [45]. Dynamic Random Access Memories (DRAMs) and Static

Random Access Memories (SRAMs), widely used because of its high integration capability, are volatile memories. Data stored in volatile memory is lost when power fails. The non- volatile memories which retain the data even if power fails, include Electrically Erasable Read Only Memories (EFPROMs) and Si- surface – potential control CMOS (Complimentary Metal Oxide Semiconductor) FET channel. However both types, in general, have problems in integration density and writing time.

Ferroelectric memories are attractive for DRAM devices because of their high permittivity [46]. Also, because of their high dielectric constant, higher memory integration is possible. $SrTiO_3$ and $Ba_xSr_{1-x}TiO_3$ (BST) films are the ferroelectric materials used for DRAM devices.

The *non-volatile* memories are very expensive. The advantages offered by Ferroelectric Random Access Memories (FRAMs) include non-volatile, radiation hardened compatibility with CMOS and GaAs circuitry, high speed (~ 30 ns, time for read/rewrite) and high density (~ 4 μm^2 cell size).

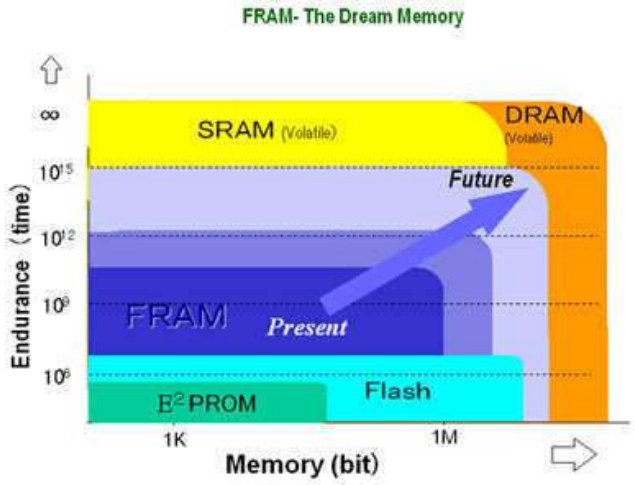

Fig. 1.14 Overview of FRAM Memory

Data in FRAM is stored by localized polarization in the microscopic regions of ferroelectric thin films. The radiation hardness of FRAMs allow for the use of devices containing these memories in harsh environments such as outer space [47-48]. For good performance of the device, the ferroelectric thin film should fulfill certain requirements. As the FRAM operates on the basis of polarization switching, the ferroelectric material should have a large remanent polarization and small coercive field.

One of the problems with memories is the tendency to lose its ability to store data after a certain number of read/write cycles. The ferroelectric materials can sustain upto 10^{12} cycles of read/write operations compared to few thousands cycles in ferromagnetic materials. This phenomenon is called fatigue. A fatigue endurance of 10^{15} cycles is desirable for the FRAMs.

(iii) **PTC phenomenon:** The increases in resistivity with increasing temperature are referred to as the PTC or PTCR *(positive temperature coefficient of resistivity)* effect, a phenomenon discovered in 1954. Since then it has been investigated intensively by many researchers [35]. PTC thermistors are used for not only for the temperature-change detection but also for active current controllers. Practical applications for these devices are made in over- current/ voltage protectors and starting switches for motors.

(iv) **Pyroelectric devices:** Pyroelectricity is utilized in the fabrication of pyrodetectors like temperature / infrared light sensors and infrared image sensors. The pyroelectric sensor is a device for transducing optical/thermal energy to electrical energy. The principle on which the pyroelectric sensors work is based on the charge generation associated on the change in spontaneous polarization with the changing temperature.

The advantages of pyrosensors compared to semiconducting infrared- sensor materials are wide range of response frequency, use at room temperature, quick response and high quality. Thin films of PZT, $PbTiO_3$ and (Pb, La) TiO_3 are widely used for pyroelectric sensing applications [49, 50].

(v) **Piezoelectric devices:** Piezoelectric materials are extensively utilized for the fabrication of various devices such as transducers, actuators, surface acoustic wave devices, frequency control and so on.

The high voltage generated in a piezoelectric ceramic under applied mechanical stress can cause sparking and ignite the gas. Usually PZT ceramic disks are used for application like gas- ignitors [51].

Piezoelectric materials can be used for both active and passive transducer applications. In the passive mode the transducer acts as a sound receiver, i.e., for the conversion of sound energy into electrical signal. The converse piezoelectric effect permits a transducer to act as an active sound transmitter [52]. Ultrasonic transducers convert electrical energy into mechanical form when generating an acoustic pulse and convert mechanical energy into an electrical signal when detecting its echo. The transmitted waves propagate into a body and echoes are generated which travel back to be received by the same transducer. These echoes vary in intensity according to the type of tissue or body structure, thereby creating images [53]. Recent laptop computers with a liquid crystal display require a very thin, no electromagnetic- noise transformer to start the glow of a fluorescent back- lamp. For this a piezoelectric transformer is used. The original piezoelectric transformer was proposed by C.A. Rosen [54].

1.5 Motivation and Aim of the Present Work

Pervoskite type structure is an important class of ferroelectric materials which are useful for various device applications because of their excellent properties such as pyroelectric, piezoelectric, electro-optic, etc. A practical advantage of pervoskite structure is that many different cations can be substituted on both the A and B sites keeping the ferroelectric properties intact.

After an extensive literature survey in the Journals like Materials Science, Ceramic International, Journal of European Ceramics Society, Ferroelectrics, Journal of Inorganic Materials, etc., it was felt that although a lot of work has been reported for both A- as well as B- site substitutions in barium titanate [55-62], however, extensive study of the changes in physical properties due to systematic substitution of tungsten in barium (strontium) titanate is lacking, prompting this candidate to undertake the present work.

There exists a vast literature on the influence of the A-site substitution in BT but not many reports on the B-site substitution in BT ceramics are available. Defects in crystals significantly influence the physical properties of the materials [63]. There are two categories of substituents, ***hard*** and ***soft*** substituents [22].

***Soft doping*:** Ions with higher valency than the substituting ion are known as a soft dopant. The soft dopants act as donor, and causes cation vacancies in the lattice and such the resulting ferroelectric materials are generally characterized by a lower coercive field (E_c), higher dielectric constant and bulk resistivity [22].

Hard doping: The substitution by lower -valent cations for the constituent ions is known as hard doping. A hard dopant is acts an acceptor, and it causes oxygen (anion) vacancies in the lattice. "*Hard*" ferroelectrics are generally characterized by lower

dielectric constant and bulk resistivity but higher coercive field [22]. The change in ferroelectric properties is considered to originate from defects generated due to dopant types.

In the present work, a systematic investigation has been carried out to study the influence of B- site compositional changes on the structural and electrical properties of barium titanate and barium strontium titanate compounds which are discussed in the following seven chapters of this thesis.

Chapter 1 includes the introduction to historical development of ferroelectric materials and the phenomenon of ferroelectricity. Various properties of ferroelectric materials such as dielectric, ferroelectric, piezoelectric and pyroelectric properties have also been introduced.

Chapter 2 contains the details of the experimental techniques used in the present work.

Chapter 3 contains the optimization of sintering conditions and the effect of heating rate on the properties of $BaTi_{0.85}W_{0.15}O_3$.

C***hapter 4*** contains the observations and results and discussions of tungsten substituted barium titanate.

C***hapter 5*** contains the effect of tungsten substitution in barium strontium titanate on the microstructural, dielectric and ferroelectric properties.

In **C*hapter 6***, synthesis and characterization of barium titanate and tungsten substituted barium titanate by mechanical activation method has been discussed.

Chapter 7 contains the inference from the present study and suggestions for further work.

References

[1] L. E. Cross, "*Ferroelectric ceramics: Tailoring properties for specific applications, in Ferroelectric Ceramics,* edited by N. Setter and E. L. Colla", (Birkhauser, Verlag, Basel, 1993) 1.

[2] J. Valasek, *Phys. Rev*. **17** (1921) 475.

[3] G. H. Haertling, *J. Am. Ceram. Soc*. **82** (1999) 797.

[4] D. Damjanovic, *Rep. Prog. Phys*. **61** (1998) 1267.

[5] L. E. Cross and R. E. Newnham, *History of ferroelectrics, ceramics and civilization.High- technology ceramics- past, present and future,* vol. III (American Ceramic Society, Westerville, Ohio, 1987) P. 289-305.

[6] B. M. Wul and I. M. Goldman, Dokl. Akad. Nauk. SSSR. **46** (1945) 154.

[7] D. Baker, D. C. Koehler, W. O. Fleckenstein. G. E. Roden and R. Sabia, Materials Technology, Vol. II (Prentice- Hall Inc., Englewod Cliffs, New Jersey).

[8] K. Uchino, *Ferroelectric Devices* (Marcel Dekker Inc., New York, 2000).

[9] B. Tareev, *Physics of Dielectric Materials* (Mir Publishers, Moscow, 1979).

[10] R. A. Conclaser and S. D. Nagle, *Materials and Devices for Electrical Engineers and Physicists* (McGraw Hill Co., New York).

[11] S.O. Kasap, Principles of Electronics Materials and Devices, 2nd Edition (Tata McGraw- hill Inc., New York, 2002).

[12] R. C. Buchanan, *Ceramics Materials for Electronics: Processing, Properties & Applications* (Marcel Dekker Inc., New York, 1991).

[13] J. C. Anderson and K. D. Leaver, *Materials Science* (Thomas Nelson and Sons Ltd., London, 1969).

[14] C. Kittle, *Introduction to Solid State Physics* (John Wiley and Sons Inc., New Jersey, **7th** Edition, 1996).

[15] R. Waser, U. Bottger and S. Tiedke, *Polar Oxides: Properties, characterization and Imaging* (Wilet –VCH Verlag Gmbh & Co. KGaA, Weinheim, 2005).

[16] R. M. Rose, L. A. Shepard and J. Wulff, Electronic Properties (Wiley eastern Pvt. Ltd., North Dakota, 1965).

[17] I. S. Zheludev, *Physics of Crystalline Dielectric: Crystallography and Spontaneous Polarization,* Vol. I (Plenum Press, New York, 1971).

[18] W. Kanzig, *Ferroelectric and Antiferroelectric in Solid State physics*, Vol. 4 (Academic Press, New York, 1957).

[19] M. Lines and A. Glass, *Principles and Applications of Ferroelectrics and Related Materials* (Clarendon Press, Oxford, 1979).

[20] A. J. Dekker, *Solid State Physics* (Macmillan, New York, 1991).

[21] B. A. Strukov and A. P. Lavanyuk, *Ferroelectric Phenomena in Crystals* (Springer, New York, 1998).

[22] Y. H. Xu, *Ferroelectric Materials and their Applications* (Elsevier Science Publishers, Amsterdam, 1991).

[23] G. Yi, Z. Wu, M. Sayer, C. Jen and J. F. Bussiere, *Electron. Lett*. **25** (1989) 907.

[24] T. Mitsui, I. Tatsuzaki and E. Nakamura, *An Introduction to the Physics of Ferroelectrics* (Gordon and Breach, London, 1976).

[25] Y. J. Song, H. H. Kim, S.Y. Lee, D. J. Jung, B. J. Koo, J. K. lee, Y. S. Park, H. J. Cho, S. O. Park and K. Kim, *Appl. Phys. Lett*. **76** (2000) 451.

[26] F. Jona & G. Shirrane, *Ferroelectric Crystals* (Pergamon Press, Oxford. London, 1962)

[27] J. Y. Nye, *Physical Properties of Crystals* (Clarendon Press, Oxford, 1990).

[28] R.E. Newnham, *Structure- Property Relations* (Springer Verlag, New York, 1975).

[29] A. Safari, R.K. Panda and V. F. Janas, *Ferroelectric Ceramics: Processing, Properties & Applications* (Rutgers University, Piscataway NJ, USA).

[30] S. B. Lang, *Source Book of Pyroelectricity* (Gordon & Breach, N. Y., 1974).

[31] B.T. Batthais and A. V. Hippel, *Phys. Rev*. **73** (1948) 1378.

[32] A. V. Hippel, *Rev. Modern Phys*. **22** (1950) 221.

[33] R. E. Nettleton, Ferroelectrics **1** (1970) 3.

[34] R. E. Nettleton, Ferroelectrics **2** (1971) 5.

[35] B. Jaffe, W. R. Cook Jr. and H. Jaffe, *Piezoelectric Ceramics* (Academic Press, London, 1971).

[36] P. B. Jasmieson, S. C. Abrahams and J. L. Berstein, *J. Chem. Phys*. **48** (1965) 5048.

[37] G. Goodman, *J. Am. Ceram. Soc*. **36** (1953) 368.

[38] M. H. Francombe and B. Lewis, *Acta Crystallogr*. **11** (1958) 696.

[39] B. Aurivillius, Ark. Kemi. **2** (1950) 519.

[40] B. Aurivillius, Ark. Kemi. **5** (1952) 39.

[41] L.E. Cross, *Ferroelectric Ceramics: Tutorials Reviews, theory, processing and Applications* (Birkhauser Verlag, Basel, 1993).

[42] W.G.Cady, *Piezoelectricity* (Dover Publication, New York, 1962).

[43] I. H. Pratt and S. Firestone, *J. Vac. Sci. Tech*. **8** (1971) 256.

[44] H. J. Hagemann, D. Hennings and R. Wernicke, *Phillips Tech. rev*. **41** (1983) 89.

[45] M. Barr and A. Massa, Programming Embedded Systems (O'Reilly Massachusetts, 2006).

[46] M. Okuyama, *Bull. Ceram. Soc. Jpn*. **30** (1995) 504.

[47] J. F. Scott, L. Kammerdiner, M. Paris, S. Traynor, V. Ottenbacher, A. Shawabkeh and W. F. Oliver, *J. Appl. Phys*. 64 (1988) 787.

[48] J. F. Scott, C.A. Araujo, H. B. Meadows, L, D. McMillan, A. Shawabkeh and W. F. Oliver, *J. Appl. Phys*. **65** (1989) 1444.

[49] K. Ijima, Y. Tomita, R. Takayama and I. Ueda, *J. Appl. Phys.* **60** (1986) 361.

[50] R. Takayama, Y. Tomita, K. Ijima, *J. Appl. Phys*. **61** (1987) 411.

[51] A. J. Moulson and J. M. Herbert, *Electroceramic Materials, Properties and Applications* (Chapman and Hall, London, 1990).

[52] B. A. Auld, *Acoustic Fields and Waves in Soilds*, Vol. 1, 2nd edition (Krieger Publishing, Melbourne, 1990).

[53] G.S. Kino, *Acoustic Waves: Devices Imaging and Analog Signal Processing* (Prentice-Hall, Englewood Cliffs, New Jersey, 1987).

[54] C. A. Rosen, *Proc. Electronic Component Symp*. (1957) 205.

[55] D. Morrison Finlay, D. C. Sinclair, A. R. West, *International Journal of Inorganic Materials* **3**(2001) 1205-1210.

[56] Om Prakash, Devandra Kumar, R. K. Dwivedi, K. K. Srivastava, Prakash Singh, Sindhu Singh, *J. Material Science* **42** (2007) 5490-5496.

[57] Jianquan Qi, Langtu Li, Yongli Wang, Yuwei fan, Zhilum Gui, *Materials Chemistry and Physics* **82** (2003) 423-427.

[58] M.T. Benlahrache, S. E. Barama, N. Benhamla, S. Achour, *Materials Science in Semiconductor Processing* **9** (2006) 1115-1118.

[59] D. John. Bak and C John. Wright, *J. Phys. Chem*. *B* **109** (2005) 18391-18399

[60] L. Szymczak, L. Kozielski, M. Adamczyk, A. Lisinska-Czekaj, Z. Ujma and D. Czekaj, *Ferroelectric*, **349** (2007) 179-178.

[61] Yanxia Li, Xi Yao, Liangying Zhang, *Ceramics International* **30** (2004) 1283-1287.

[62] H. B. Sharma, A. Mansingh, *Journal of Material Science* **33** (1998) 4455-4459.

[63] T. J. Boyle, C. D. Buchheit, M. A. Rodriguze, H. N. Al-Shareef & B. A. Hernandez, *J. Mater. Res.,* **11** (1996) 256.

Chapter 2

Chapter 2

Experimental Details

This chapter contains experimental details along with the theoretical background of the various structural and electrical parameters studied in the present work. The experimental techniques including the procedure for the sample preparation and characterization are described.

2.1 Preparation Techniques

The following section discusses the method for the preparation of the samples.

2.1.1 Solid – State Reaction Method

The flowchart showing the steps of solid-state reaction method is shown in Fig. 2.1. The key stages in this method of sample preparation are calcinations and sintering [1, 2].

High purity raw materials (carbonates and oxides) in the form of powders are first weighed according to their stoichiometric formula of the composition. The particle size of the powders must be in the submicron range for the solid phase reaction to occur. The next step in this method is the mixing of the constituent powders and grinding them**.** The powder mixture is then calcined at appropriate temperature. Calcination process helps in the decomposition of the constituent carbonates into oxides and removal of carbon dioxide. For example,

$$BaCO_3 \longrightarrow BaO + CO_2\uparrow$$

During the calcination step, the solid phase reaction takes place between the constituents resulting in the partial development of the phase [3-4]. Calcination causes the constituents to interact by interdiffusion of their ions.

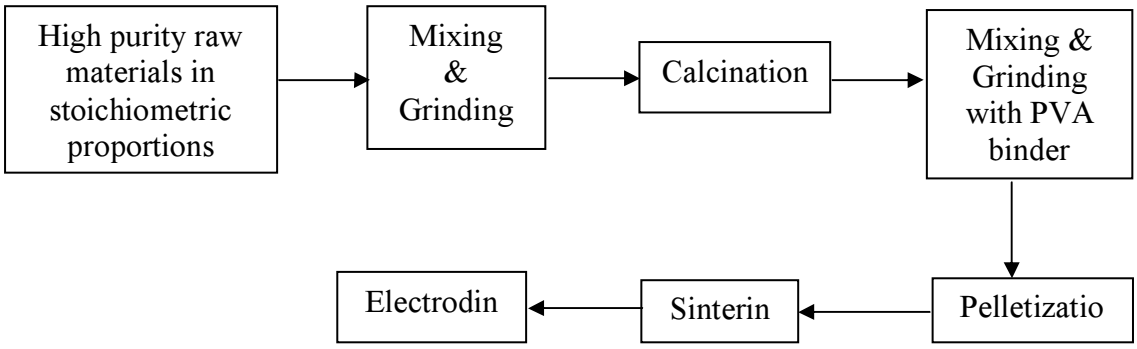

Fig. 2.1 Flowchart diagram representing the steps of solid-state reaction method

The calcining temperature is important as it influences the density/ microstructure and hence the properties of the final product. After calcination, the lumps of the mixture are crushed and thoroughly ground. Very often it is necessary to add an organic binder material like polyvinyl alcohol (PVA) for sufficient adhesion during pelletization. There are various shaping methods like powder compaction / dry pressing, isostatic pressing, extraction, slip- casting, etc. [5]. The choice of method depends on the type of material used, desired shape and thickness of the product. After shaping, the pellets are sintered. During sintering, the particles join in the region of contact by growth of neck [6, 7]. Therefore, it results in densification and grain growth. The sintering process considerably effects grain boundaries and pores. The various models and mechanisms have explained the sintering process [2, 8, 9]. From the matter transport mechanism point of view, sintering process can be divided into three stages, viz., initial stage, intermediate stage and final stage. The initial stage is

associated with the growth of neck between the particles by lattice diffusion. In the intermediate stage, the structure grows and the particles lose their individual identity, the pores form continuous channel and all the pores intersect at the grain boundaries. At the final stage, pores either occur as isolated entities on the corner of the grains or totally enclosed within them. The sintering temperature and duration is thus crucial and should be optimized. Also, the surrounding atmosphere influences the properties of the final product. The sintered pellets are then polished so as to have smooth and parallel surfaces. Electroding of the sintered samples is required to provide electrical contacts.

Sample Preparation

This section presents the details of the method used for the preparation of the various compositions studied in the present work. The sintering condition was optimized (by preparing the samples under different sintering temperatures and durations) in order to achieve the best properties. The ferroelectric ceramics having the following compositions were prepared by the solid-state reaction technique.

$BaTiO_3$ and $BaTi_{0.85}W_{0.15}O_3$ with sintering temperatures of

1200 ^{0}C, 1250 ^{0}C and 1300 ^{0}C for 2 hours and 5 hours durations.

$Ba(Ti_{1-x}W_x)O_3$; x = 0.00, 0.05, 0.10, 0.15, 0.30

$Ba_{0.8}Sr_{0.2}(Ti_{1-x}W_x)O_3$; x = 0.00, 0.05, 0.075, 0.10, 0.15, 0.30

The staring chemicals used were barium carbonate ($BaCO_3$), titanium oxide (TiO_2) strontium carbonate ($SrCO_3$) and tungsten oxide (WO_3). All the chemicals used were acquired from Aldrich Chem. Co., U.S.A., having purity ≥ 99.9 %. The chemicals were weighed in stoichiometric proportions as mentioned above. The

weighed powders were mixed and thoroughly ground by agate-mortar and passed through sieve of fine mesh. This powder mixture was then calcined at 1150 ^{0}C for 2 hours in alumina crucibles. The calcined powders were ground and admixed with about 5 wt. % PVA (Aldrich, USA) as a binder. Thereafter, the calcined powder was pressed into disk shaped pellets using hydraulic press by applying a uniaxial pressure of 300 MPa. To study the effect of sintering temperature and duration on the structural and electrical behavior of the studied compositions and to determine the optimum sintering condition for the best properties, the pellets were sintered in air at the following sintering conditions:

(i) 1200 °C, 2h;

(ii) 1250 °C, 2h;

(iii) 1300 °C, 2h;

(iv) 1300 °C, 5h.

Further, to investigate the effect of heating rate on the properties, the specimens were heated to the sintering temperature at the following rate.

(i) 1 °C/min

(ii) 3 °C/min

(iii) 8 °C/min

(iv) 13 °C/min, and

(v) 20 °C/min

The sintered pellets were then polished to a thickness of 1mm. High temperature conductive silver paste was coated over the parallel surfaces of the samples, to act as electrodes and cured at 300 °C for 15 minutes. Calcination, sintering and curing was done in a programmable muffle furnace (Electroheat, India).

2.1.2 Mechanical Activation Method

In the mechanical activation process, the solid state reaction of oxides is activated by the mechanical energy produced by the milling process. This process skips the high energy consuming calcinations step, making the preparation process simpler than the conventional solid-state technique.

In this process, the stoichiometric mixture of powders was milled in a planetary ball mill (Retsch –PM 100, Germany). To optimize the milling duration the powders has been milled for 5 hours, 10 hours, 20 hours and 30 hours at a milling speed 400 rpm. Milling was carried out in toluene medium with 10 mm zirconium oxide balls in a zirconium oxide vial with a ball–to–powder weight ratio of 8:1. The milling was stopped for 30 minutes after every 1 hour of milling to cool down the system. The mixture was then admixed with 5wt. % polyvinyl alcohol (Aldrich, USA) as a binder and then pressed at 300 MPa into disk shaped pellets. The ferroelectric ceramics having the following compositions were prepared by mechanical activation method:

$$Ba\ (Ti_{1-x}W_x)O_3;\ x = 0.0,\ 0.05$$

The sintered pellets were then polished to a thickness of 1mm. High temperature conductive silver paste was coated over the parallel surfaces of the samples to act as electrodes and cured at 300 °C for 15 minutes.

2.2 Experimental Techniques Used for Characterization

The following section discusses the instruments / techniques used for the structural and electrical characterization of the samples. A brief theoretical introduction to the characterization parameters is also given.

2.2.1 Structural Characterization

2.2.1.1 X-ray Diffraction (XRD)

X- ray crystallography is a technique in which the pattern produced by the diffraction of X-rays through the closely spaced atoms in a crystal is recorded and then analyzed to reveal the nature of that lattice (Fig. 2.2). Geometrically, one may imagine that a crystal is made up a number of lattice planes and that the scattering from a set of planes will only be strong if the X-rays reflected by each plane arrive at the detector in the same phase. This leads to a relationship between the order of diffraction pattern n, X-ray wavelength λ, the spacing between lattice planes d and the angle of incidence θ, known as Bragg's law [10, 11]:

$$2d \sin \theta = n\lambda \qquad (2.1)$$

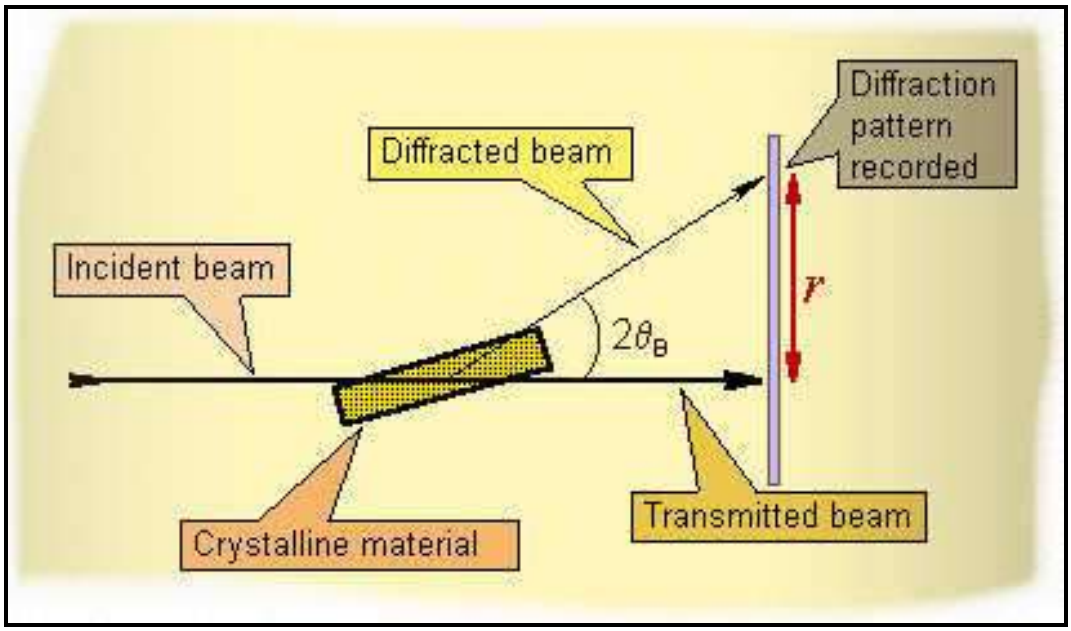

Fig. 2.2 Working principle of X-ray diffraction

X-ray powder diffraction finds frequent use in materials science as it is non-destructive and easy to use.

Utility of the XRD Patterns

Phase Identification

The most widespread use of this technique is the identification of crystalline solids. Each crystalline solid produces its own diffraction pattern which can be compared to a database of known materials, like JCPDS (Joint Committee of Powder Diffraction Standards) database in order to identify the contents of the samples and to determine the relative intensity of the characteristic lines of particular phase. The patterns thus provide a fingerprint of the phases present in the material [12].

Crystallinity

In contrast to the patterns crystalline materials that consists of series of sharp peaks, amorphous materials (e.g., liquids, glasses, etc.) produce a broad background patterns. XRD patterns can be used to determine the crystallinity by comparing the integrated intensity of the background pattern to that of the sharp peaks [12].

Crystallite Size

From the broadening of the XRD peaks, it is possible to determine average crystallite size by using Debye- Scherrer formula [10]:

$$P_{hkl} = K \lambda / \beta_{1/2} \cos \theta \qquad (2.2)$$

where K = 0.89, λ = wavelength of the radiation, $\beta_{1/2}$ is the full width at half maximum, or half-width (FWHM) and θ = the angular position of the peak.

Tetragonal Strain

The strain in a lattice along c- axis is defined as tetragonal strain (c/a) or principal strain or tetragonality [13]. The tetragonal strain is the internal strain in the lattice which is related to the phase transition temperature in these compounds and increase in tetragonal strain has been reported to increase the Curie temperature [14, 15].

X-ray Diffraction Analysis

In the present work, X-ray diffractrograms of all the samples were recorded for the structural analysis and for the determination of the various phases present in the samples. An schematic diagram of a diffractometer is shown in Fig. 2.3 (a). A Bruker (D8 Advance), diffractometer was used with CuKα radiation of wavelength (λ) 1.5405 A^{o}. The samples were analyzed in the 2θ range of 20° to 70° at a scanning rate 1° / min. The diffractrometer was operated using diffraction software which evaluate the inter-planar spacing (d_{hkl}) values corresponding to all the observed peaks using the Bragg's law.

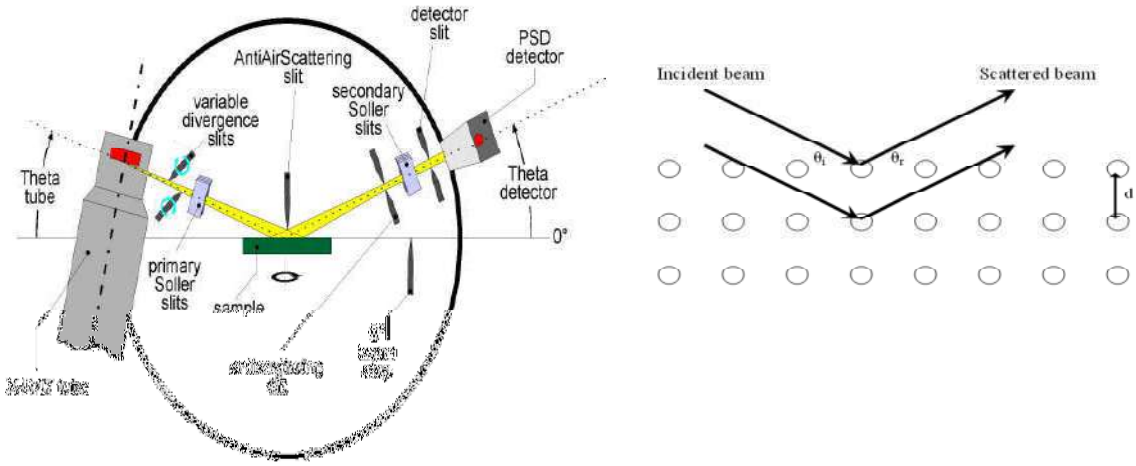

(a) (b)

Fig. 2.3 (a) Schematic diagram of a diffractometer (b) Bragg's diffraction

Taking the intensity of the highest peak to be 100%, the relative intensity of other peaks is measured. The lattice parameters a, b, c were calculated from the observed d-values using the formula:

$$d_{hkl} = 1/\ [(h/a)^2 + (k/b)^2 + (l/c)^2]^{1/2} \qquad (2.3)$$

where h, k, l is the Miller indices corresponding to different planes. The peaks were indexed and the lattice parameters as deduced from the X- ray diffractorgam's data were refined using least square refined using least square refinement method by a

computer program package – Powder X [16]. The structural distortion parameters like tetragonal strain were calculated using the lattice parameters.

2.2.1.2 Scanning Electron Microscopy (SEM)

Electron Microscope

A microscope that uses electrons rather than light to form an image is called an Electron Microscope. The Scanning Electron Microscope (SEM) is a type of electron microscope that images the sample surface by scanning it with a high-energy beam of electrons in a raster scan pattern. The electrons interact with the atoms that make up the sample producing signals that contain information about the sample's surface topography, composition and other properties such as electrical conductivity. It has a large depth of field of view, which allows a large amount of the sample to be in focus at one time. The images produced have high resolution, which means that closely spaced features can be examined.

Working Principle of SEM

In a SEM, an electron beam is thermionically emitted from a tungsten or lanthanum hexaboride (LaB_6) cathode (electron gun) or via field emission gun (FEG) and are accelerated towards an anode. The electron beam, which typically has an energy ranging from 0.5 keV to 40 keV, is focused by one or two condenser lenses to a spot 0.4 nm to 5 nm in diameter. The beam passes through pairs of scanning coils or pairs of deflector plates in the electron column, typically in the final lens, which deflect the beam along the *x*- and *y*- axes so that it scan in a raster fashion over a rectangular area of the sample surface. When the primary electron beam interacts with the sample, the electron lose energy by repeated random scattering and absorption within a teardrop-shaped volume of the specimen known as interaction volume, which extends from less than 100 nm to around 5 μm into the surface. The size of the interaction volume depends on the

electron's landing energy, the atomic number of the specimen and the specimen's density. The energy exchange between the electron beam and the sample results in the reflection of high-energy electrons by elastic scattering, emission of secondary electrons by inelastic scattering and the emission of electromagnetic radiation, each of which can be detected by specialized detectors. The beam current absorbed by the specimen can also be detected and used to create images of the distribution of the specimen current. Electronic amplifiers of various types are used to amplify the signals which are displayed as variations in brightness on a cathode ray tube. The raster scanning of the CRT display is synchronized with that of the beam on the specimen in the microscope, and the resulting image is therefore a distribution map of the intensity of the signal being emitted from the scanned area of the specimen. The image may be captured by photography from a high resolution cathode ray tube, but in modern machines, is digitally captured and displayed on a computer monitor and saved to a computer's hard disc.

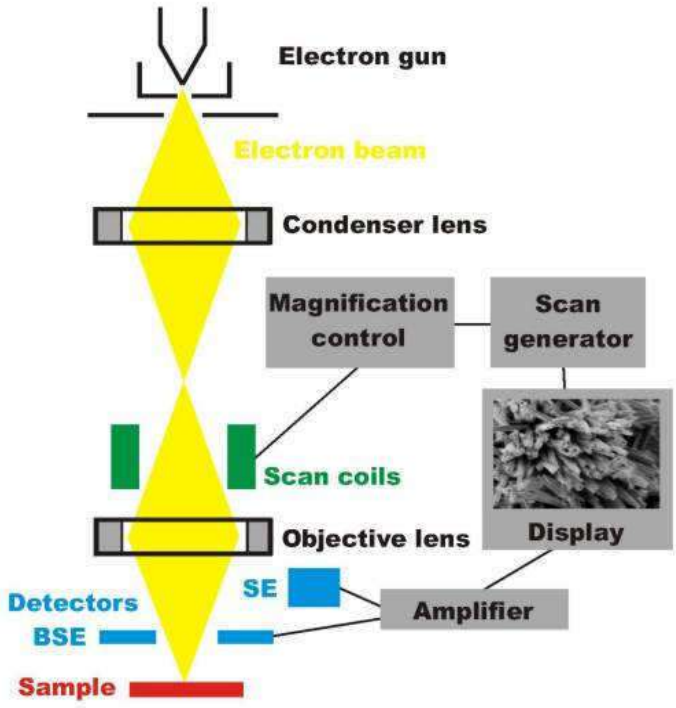

Fig. 2.4 Working principle of SEM

Microstructural Studies

In the present study, SEM (Hitachi S – 3700N, Japan) was used to determine the average grain size and surface morphology of the samples. The parameters of SEM settings used in the present work are listed in Table 2.1. Average grain size was calculated using the linear intercept method.

Table 2.1 Typical SEM settings used

Accelerating voltage	**20kV**
Probe current	**0.4 nA**
Working distance	**10 mm**

2.2.1.3 Transmission Electron Microscopy (TEM)

Transmission electron microscope (Fig. 2.5) is another type of electron microscope whereby a beam of electrons is transmitted through an ultra thin specimen. The electrons interact with the specimen as it passes through. An image is formed from the interaction of the electrons transmitted through the specimen; the image is magnified and focused onto an imaging device, such as a fluorescent screen or on a layer of photographic film or to be detected by a sensor such as CCD camera. It is capable of imaging at a significantly higher resolution enabling the instrument's user to examine fine details even as small as a single column of atoms.

In the present study (TECNAI G^2 30U Twin) was used to view the nanoparticles of $Ba(Ti_{1-x}W_x)O_3$, x = 0.0, 0.05 compound prepared by mechanical activation process at HV = 300 kV.

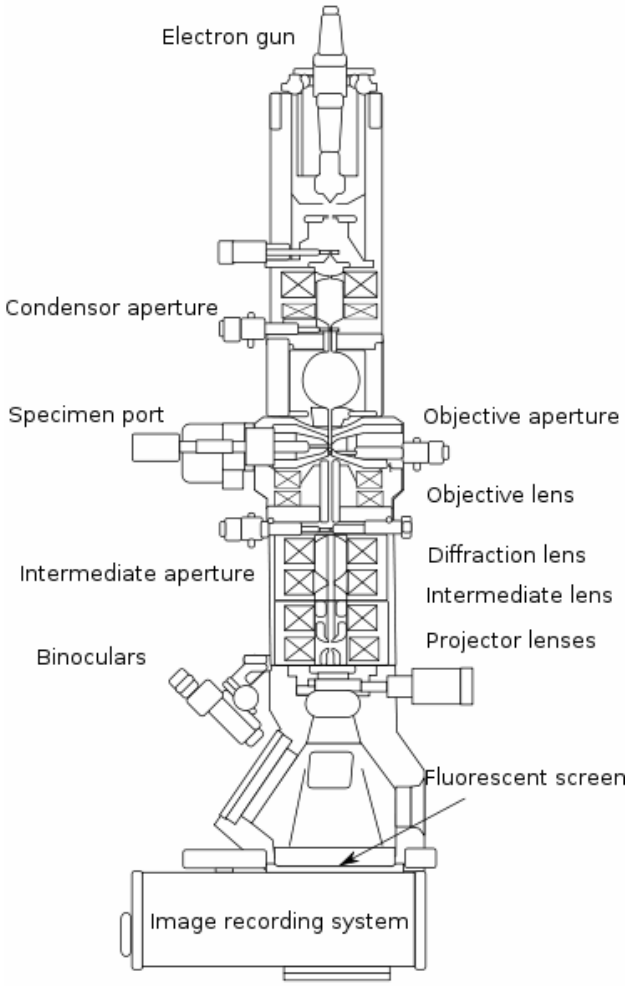

Fig. 2.5 Schematic diagram of TEM

2.2.1.4 Density Measurement

The density measurement was performed employing the Archimedes principle. The Archimedes method is based on hydrostatic weighing and it is the best-known density measurement technique [17]. In this method, the weight of a specimen is measured in two different media, e.g., air and liquid. To calculate the density of the specimen ρ_{exp}, the following equation was used:

$$\rho_{\exp} = \frac{W_{air}\rho_{liq}}{(W_{air} - W_{liq})} \tag{2.4}$$

where ρ_{liq} is the density of the liquid. Weighing in air was done using a precision digital balance (Precisa, Switzerland) and the weight in liquid was determined by suspending the sample in ethylene glycol having density 1.112 g/cm^3.

2.2.2 Electrical Characterization

2.2.2.1 Dielectric Studies

In these classes of materials the dielectric constant and dielectric loss are the two important parameters and the studies of the dielectric properties provide a great deal of information for understanding the behavior and the mechanism of electric polarization [18-22]. Dielectric measurements are most commonly used for the identification of the phase transitions. Since the ability of these materials to polarize quickly is important for their use in memory applications, it is important to have information on the frequency dependence of the dielectric behavior [23, 24].

The capacitance (C), which is a measure of a body to hold electrical charge, is given in a parallel plate capacitor where two parallel metal electrodes, each of area A square meters, separated by a distance d meters filled with a dielectric material of permittivity ε, as

$$C = \varepsilon A/d \tag{2.5}$$

The permittivity ε which is the intrinsic property of a dielectric material is related to the permittivity of free space ε_0 as

$$\varepsilon = \varepsilon_o\varepsilon_r \tag{2.6}$$

where ε_r is the relativity permittivity which is simply a number.

Complex Permittivity

The response of normal dielectrics to externally applied electric fields generally depends on the frequency of the field. The frequency dependence reflects the fact that

a materials polarization does not respond instantaneously to an applied field. For this reason permittivity is often treated as a complex function of the angular frequency (ω) of the applied field and is represented as

$$\varepsilon_r^*(\omega) = \varepsilon'_r(\omega) - j\varepsilon''_r(\omega); \qquad j = \sqrt{-1} \tag{2.7}$$

where $\varepsilon_r^{'}(\omega)$ is the real part of the permittivity representing the lossless permittivity which is related to the electrical energy stored within the medium and is known as dielectric constant, while $\varepsilon_r^{''}(\omega)$ is the imaginary part of the permittivity, which is related to the loss of energy within the medium.

Phasor Diagram

When the applied voltage (V) is sinusoidal, charge stored in the dielectric can be expressed as:

$$Q = CV_0 e^{j\omega t} \tag{2.8}$$

while the current flowing through the capacitor is given by

$$I = j\omega\varepsilon_r C_o V \tag{2.9}$$

If the power is not dissipated in the dielectric of the capacitor "*ideal dielectric*", the phasor of current I through the capacitor would be ahead of the phasor of voltage V precisely by 90°. In real dielectrics, however, the phase angle φ is slightly less than 90°. The total current I through the capacitor can be resolved into two components, i. e., Ic (capacitive current) and I_R (resistive current). This is depicted in the phasor diagram of current and voltage in a capacitor energized by an alternating voltage (Fig. 2.6). The current I_c is proportional to the charge stored in the capacitor and leads the voltage by 90° and the current I_R is conduction current in phase with voltage V, which represents the energy loss or power dissipation in the dielectric.

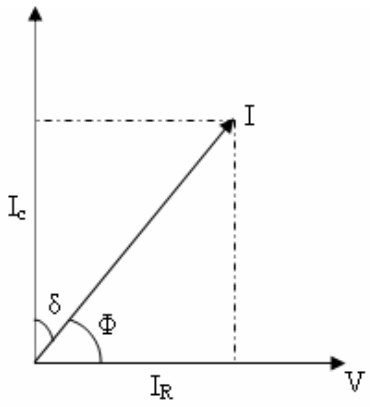

Fig. 2.6 Phasor diagram of I and V in a dielectric

Since the phase angle is very close to 90° in a capacitor with a high quality dielectric, the angle δ is a more descriptive parameter which, when added to the angle φ becomes equal to 90° [25].

$$\delta = 90° - \varphi \tag{2.10}$$

where the angle δ is called the dielectric loss angle. The dielectric loss angle is an important parameter for the material of a dielectric. All other conditions being equal, the dielectric losses grow with this angle [25]. This parameter is usually described by the loss tangent, tan δ.

On choosing the complex form of dielectric constant ε (Eq. 2.7) and using it in Eq. 2.9, we get

$$I = j\omega\varepsilon_r^{'}\varepsilon_0 C_0 V + \omega\varepsilon^{"}{}_r C_0 \varepsilon_o V \tag{2.11}$$

$$I = I_C + I_R \tag{2.12}$$

From the magnitude of these currents, therefore, the dissipation factor, tan δ can be defined as:

$$\text{D (dissipation factor)} = \tan\delta = \left|\frac{I_R}{I_C}\right| = \frac{\varepsilon^{"}{}_r}{\varepsilon^{'}{}_r} \tag{2.13}$$

The quality factor Q is defined as the ratio of the energy stored in a component to the energy dissipated by the component per cycle [25]:

$$Q = \frac{\text{Energy Stored}}{\text{Energy Dissipated}} = \frac{1}{\tan\delta} = \tan\varphi \qquad (2.14)$$

The value of tan δ for a given material is not strictly constant and depends on various external factors.

Frequency Dependence of Permittivity

The dependence of ε on frequency is known as dielectric dispersion and is shown in Fig. 2.7. The total polarization P, the total polarizability α and the relative permittivity ε_r of a dielectric in an alternating field, all depend on the ease with which the dipoles can reverse alignment with each reversal of the applied electric field [26, 27]. There are four frequency ranges in which different polarization mechanism dominates. Since the relaxation frequencies of all the four polarization processes differ, it is possible to separate contributions experimentally.

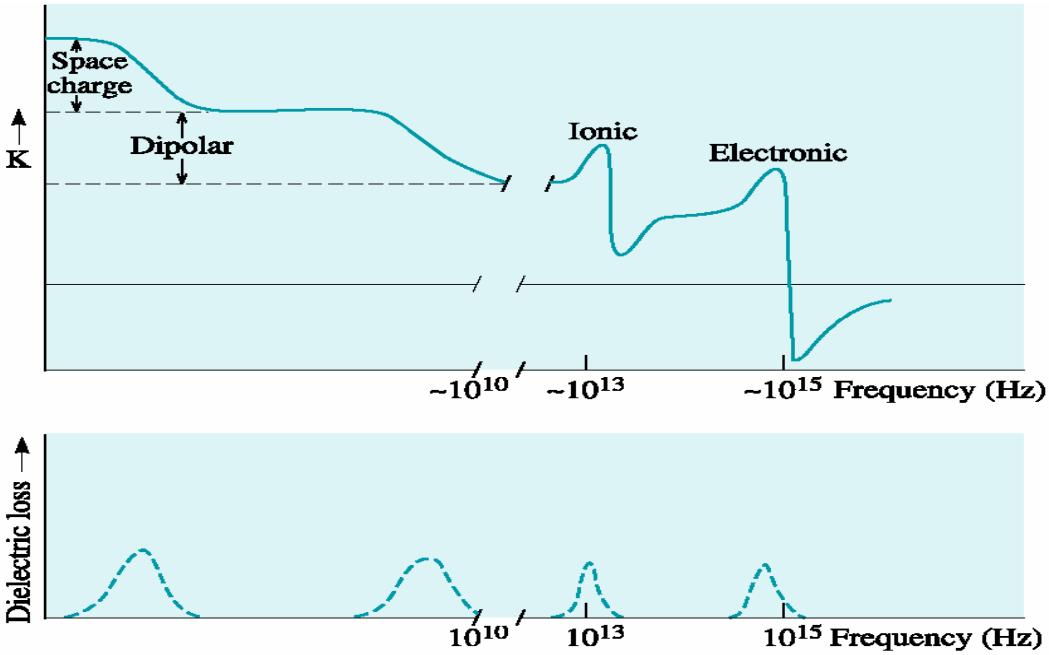

Fig. 2.7 Frequency dependence of the real and imaginary parts of dielectric

Each polarization component has a characteristics relaxation frequency. As the frequency becomes larger, the slower mechanism drops off. This leaves only the faster mechanism to contribute to the observed dielectric constant $\varepsilon'_r(\omega)$. The dielectric loss factor, $\varepsilon''_r(\omega)$ will correspondingly peak at each characteristic frequency.

Temperature Dependence of Permittivity

The effect of temperature on the dielectric constant of ionic and electronic materials is, in general, small at low temperatures, but increases with increasing temperature primarily because at elevated temperatures, ion mobility becomes appreciable [26].

The total permittivity of normal dielectrics increases with increasing temperature. But, in ferroelectric materials, the permittivity increases with increasing temperature going through a maximum at the Curie temperature (T_c) and thereafter reduces as temperature is increased further. Above the Curie temperature, the dielectric constant follows Curie –Weiss law [28].

Generally dielectric loss appreciably increases when temperature rises. In polar dielectrics, apart from dipolar losses, the loss due to the electrical conduction also exists, which grows with increasing temperature [29].

Measurement of Dielectric Parameters

Precision LCR meters (Agilent 4284A and 4285A, USA) were used for measuring the *dielectric constant* and *dielectric loss* in the present work. The frequency dependence of dielectric permittivity and loss was studied in the frequency range 20 Hz- 1 MHz and 100 kHz -1 MHz. The temperature dependence of dielectric properties was measured from room temperature to 200 °C, except for few samples where low

temperature measurement using liquid nitrogen was also carried out to get the Curie temperature, as a function of signal frequency at oscillation amplitude of 1V with no DC bias. The variations in dielectric constant and loss values with temperature were recorded at constant heating rate of 2 °C / minute. For the measurements, the sample was mounted on a laboratory made two probe sampler holder. The schematic diagram of the sample holder is shown in Fig. 2.8.

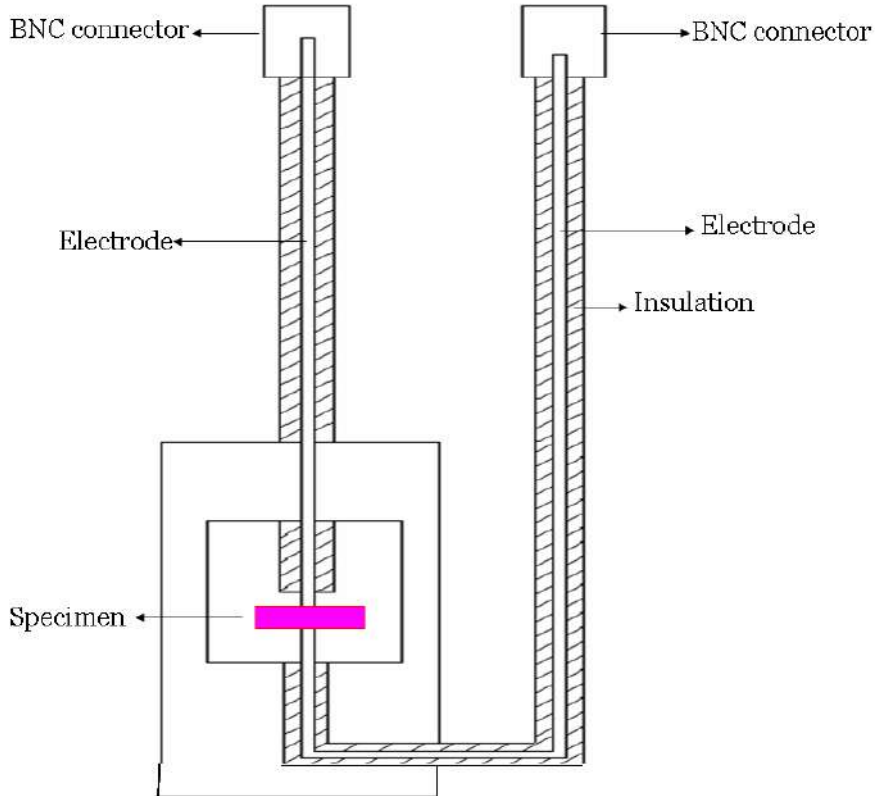

Fig. 2.8 Schematic diagram of the laboratory made sample holder

2.2.2.2 Electrical Conductivity Measurements

Electrical Conductivity was measured by applying a steady voltage across the specimen and measuring the resulting current [25]. Although, dielectrics are the materials that under normal circumstances do not allow current to flow, however, stray charges and defects cause a small conduction current through them. In other

words, the conductivity σ of insulators is extremely small but it is not zero [30]. In 1926, A. Jaffe [29] put forward the idea that the conduction in ionic crystals observed even at low temperature can be caused by the ions tearing themselves away from the lattice points as a result of thermal oscillations. This point of view was developed and quantitatively substantiated by Ya Frenkel [31].

The current density in a parallel plate capacitor can be defined in terms of materials properties as [24],

$$J = \omega\varepsilon_0\varepsilon''_r E + j\omega\varepsilon_0\varepsilon'_r E \tag{2.15}$$

where E is the electric field strength. Thus we have,

$$\frac{J}{E} = \sigma + j\omega\varepsilon_0\varepsilon'_r \tag{2.16}$$

This implies that the real part of the ratio J/E is the electrical conductivity σ in the material, i. e.,

$$\sigma(\omega) = \omega\varepsilon_0\varepsilon''_r(\omega) \tag{2.17}$$

The measured loss in the material ε''_r can be expressed as a function of both dipolar loss (ε''_d) and conductivity (σ) as [24]:

$$\varepsilon''_r = \varepsilon_d'' + \frac{\sigma}{\omega\varepsilon_0} \tag{2.18}$$

Mechanisms of Electrical Conduction in Dielectrics

There are three possible mechanisms of electrical conduction in dielectrics depending on the type of carriers present in the material [30]:

(i) *Ionic conduction* occurs either through the migration of positive and negative ions in an external field or through the motion of ions in vacancies due to the migration of vacancies.

(ii) *Molionic conduction* occurs through the motion of molecular ions (molions) or group of ionized molecules. This conduction is encountered, especially, in amorphous or liquid dielectrics.

(iii) *Electronic conduction* is due to the motion of free charges (electrons and / or holes) in the solid.

Thus, electrical conductivity in these materials can involve both electronic and ionic charge carriers. But in defect-free insulators, the electrons are either tightly bound or located in a filled electronic band. Similarly, in a perfect crystal, since there is no mechanism for ions to diffuse, no current can result from ionic motion.

Ionic Conductivity

The migration of the ionic defects (anion / cation vacancies) in the lattice gives rise to ionic conductivity, when the vacancies move through the lattice under influence of an applied electric field. The number of these ionic defects increases rapidly at elevated temperatures. If the conductivity is plotted against 1/T, one can usually distinguish between a low- temperature region (**I**) and a high-temperature region (**II**) (Fig. 2.9).

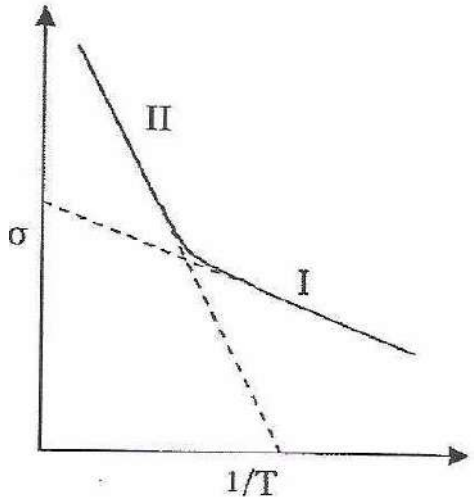

Fig. 2.9 Ionic conductivity σ as a function of 1/T

The low-temperature conduction results from the presence of impurity ions in the lattice and is called the extrinsic region of the conductivity [32]. The high-temperature region involves considerably larger activation energy and is known as intrinsic region of ionic conductivity and is caused by the movement of the component ions in the lattice and / or thermal generation of new defects. This intrinsic conductivity is dominant at high temperatures.

The value of conductivity can be obtained from Arrhenius equation [30]:

$$\sigma = \sigma_0 \exp\left(\frac{-E}{k_B T}\right) \tag{2.19}$$

and

$$E = \frac{w}{2} + \mu \tag{2.20}$$

where w and μ are the activation energies for the defect generation and migration, respectively. For extrinsic conduction w = 0 and E = μ i.e., the ionic mobility becomes the controlling factor in the conduction process of dielectrics.

Electronic Conductivity

The electronic conduction is also known to occur in dielectric materials due to property of ions to exist in more than one oxidation states which leads to the release of electrons. This process is a function of temperature and / or compositional fluctuation [30]. If present, then at low temperatures, the electronic conduction is expected to dominate as low thermal energy is sufficient to energize low mass electrons.

Conductivity Measurement

In the present work, the pellets were pasted with silver for the conductivity measurements using two-probe method. The dc conductivity was measured using a Keithley's 6517A electrometer. The measurement was performed at 1V in the temperature range of room

temperature to 250 °C and for few specimens below room temperature using liquid nitrogen as coolant. Conductivity was calculated using the relation

$$\sigma = \frac{d}{AR} \tag{2.21}$$

where A is the cross-sectional area, d the thickness of the pellet and R is the measured resistance.

2.2.2.3 Impedance Studies

Impedance (Z) is the measure of opposition to the flow of an alternating current (AC) at a given frequency. It is represented as a complex vector quantity (Fig. 2.10). The impedance vector consists of a real part, resistance (R) and an imaginary part, reactance (X) [33]. The electrical properties of a material are often represented in terms of some complex parameters like impedance (Z*), complex admittance (Y*), complex permittivity (ε*) and dielectric loss (tan δ). These frequency dependent parameters are related to each other by the following relations:

$$Z^*(\omega) = Z' - j\,Z'' = R_s - \frac{j}{\omega C_s} = \frac{1}{j\omega C_0 \varepsilon^*} \tag{2.22}$$

$$Y^*(\omega) = Y' + j\,Y'' = \frac{1}{R_p} + j\omega C_p = j\omega C_o \varepsilon^* = \frac{1}{Z^*} \tag{2.23}$$

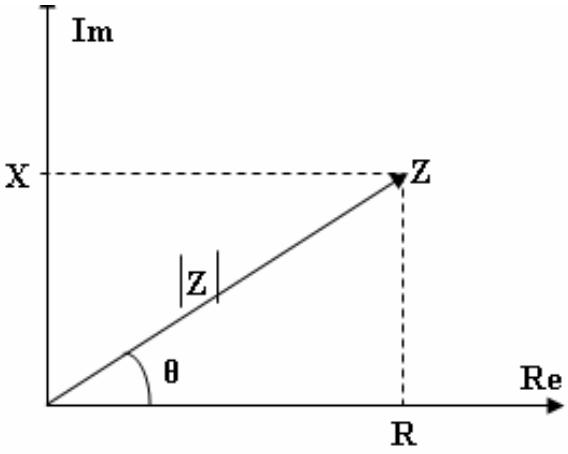

Fig. 2.10 Graphical representation of the complex impedance plane

$$\varepsilon^*(\omega) = \varepsilon' - j\,\varepsilon'' \tag{2.24}$$

$$\tan\delta = \frac{Z'}{Z''} = \frac{Y'}{Y''} = \frac{\varepsilon''}{\varepsilon'} \tag{2.25}$$

where R_s and C_s are the series resistance and capacitance; R_p and C_p are the parallel resistance and capacitance; C_0 is the geometrical capacitance ; (Z′,Y′,ε′) and (Z", Y", ε") are the real and imaginary components of impedance, admittance and permittivity respectively.

The complex impedance spectroscopy (CIS) is a non-destructive powerful technique for the characterization of electrical behaviour of electroceramic materials [34]. The technique is based on the principle of analyzing the response of a specimen to a sinusoidal electrical signal and subsequent calculation of the resulting transfer function (impedance) with respect to the frequency of the applied signal. The output response, when plotted in a complex plane, appears in the form of a succession of semicircles known as Nyquist or Cole- Cole plots in the frequency domain arising as a result of the contribution to the electrical properties due to various components such as the bulk material, grain boundary effect and interfacial phenomenon (at the material electrode interface) as depicted in Fig. 2.11. In view of this specially, the CIS technique enables us to separate the effects due to each component (bulk, grain boundary and electrode interface) in a polycrystalline sample because of the different time constants of these phenomena occurring in the specimen [35]. The first semicircle in the high frequency region manifests the effect of grain interior, while the second semicircle represents the grain boundary effects. In some cases, a third semicircle appears at very low frequencies which can be represented by an equivalent circuit consisting of a parallel resistance and capacitance (RC circuit) connected in series, each circuit being responsible for a semicircle in the Cole-Cole plot.

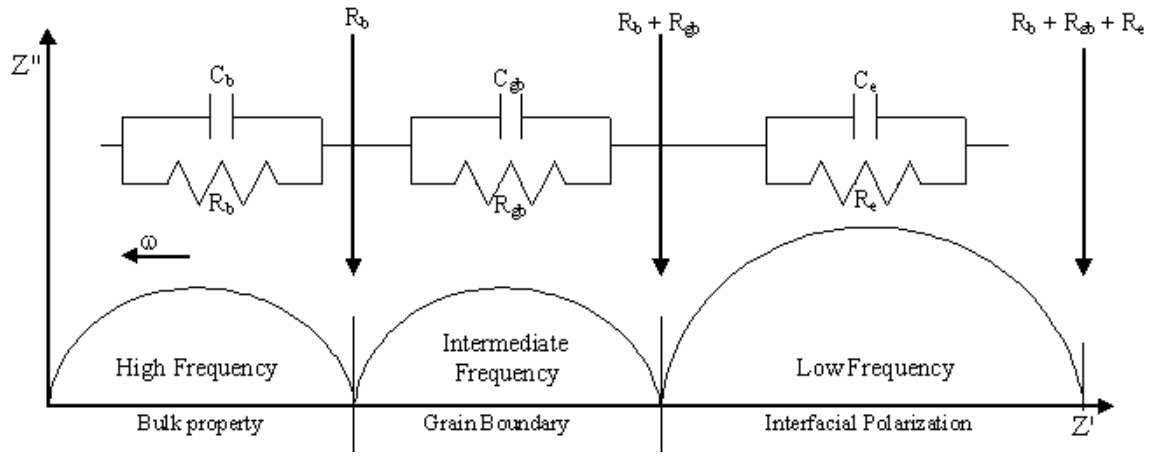

Fig. 2.11 Various components in complex impedance

Impedance Measurements

Impedance analysis was performed on the samples using LCR meter (Agilent 4284A, USA) in the frequency range of 20 Hz – 1 MHz at oscillation amplitude of 1V. The studies were performed at temperatures much higher than the Curie temperature of the samples as the semicircles starts manifesting only at the higher temperatures in the samples. The various parameters computed from the impedance plots are grain resistance (R_b), grain boundary resistance (R_{gb}), grain capacitance (C_b), grain boundary capacitance (C_{gb}) and the relaxation time. The second intercept of each semicircle on real (Z′) - axis gives the respective value of resistance (e.g. R_b and R_{gb}). The semicircles in the impedance spectrum have a characteristics peak occurring at a unique relaxation frequency frequency ($\omega_r = 1/2\pi f_r$). It can be expressed as: $\omega_r RC = \omega_r \tau = 1$. Therefore,

$$f_r = \frac{1}{2\pi\tau} = \frac{1}{2\pi RC} \tag{2.26}$$

where τ is the relaxation time. The respective capacitances (C_b and C_{gb}) due to the grain and grain boundary effect can be calculated using this relation.

The bulk conductivity (σ_{bulk}) was also calculated from the complex-impedance spectroscopy data using the following equation [32]:

$$\sigma_{bulk} = \frac{d}{R_b A} \tag{2.27}$$

where d is the thickness of the pellet and A is the area of the conducting surface of the pellet.

2.2.2.4 Ferroelectric Studies

The hysteresis loop or Polarization- Electric field (P-E) loop using Sawyer-Tower Circuit (Fig. 2.12), is widely used for the ferroelectric characterization of materials [36].

Sawyer- Tower Circuit

The ferroelectric device under test (DUT) is placed in series with a sense capacitance C_s and resistor R_s. A computer- controlled waveform generator produces an AC signal, which is applied to the DUT. The voltage at the input and the output of the DUT is measured and is analyzed by the computer (Fig. 2.12). The capacitance of the sensing capacitor must be significantly larger than the capacitance of the device under test to minimize its effect on the measurement.

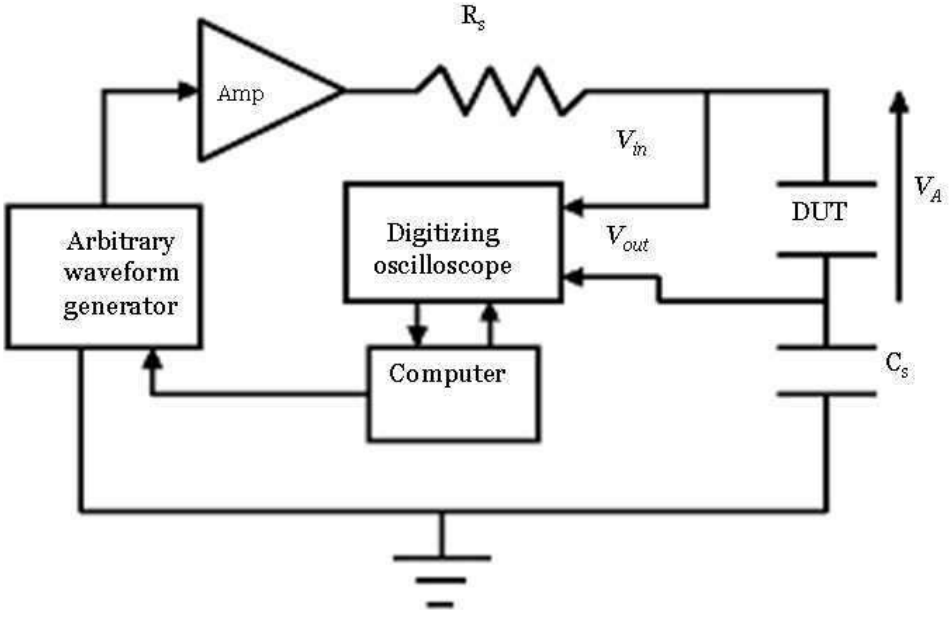

Fig. 2.12 Block diagram of Sawyer –Tower circuit

The external charge on the sense capacitor which is proportional to the external charge on the DUT, is calculated from the value of C_S and the voltage measure across C_S,

$$q = CsV_{out} \tag{2.28}$$

The voltage applied to the DUT is the difference between the voltage measured at the input and the output of the DUT,

$$V_A = V_{in} - V_{out} \tag{2.29}$$

The polarization (or charge per unit area) is calculated by dividing the total charge by the area of the pellet. The electric field is calculated by dividing the applied voltage by the thickness of the pellet.

P-E Hysteresis Loops

Hysteresis loops were recorded at room temperature (expect for few samples where temperature was lowered by using liquid nitrogen as their Curie temperature is below room temperature) using an automatic P-E loop tracer (Marine- India) based on Sawyer -Tower circuit at switching frequency of 100 Hz during the measurement. The devices under test (DUT), i.e, the pellet were placed in silicon oil bath during the measurement. The measurement gives P-E hysteresis loops from which remanent polarization (P_r) and coercive field (E_c) were determined.

2.2.2.5 Piezoelectricity

In 1880, Jacques and Pierre Curie discovered an unusual characteristic in certain crystalline minerals that when subjected to a mechanical force become electrically polarized [37]. Subsequently converse of this relationship was also observed, i.e., if an electric field is applied to the crystal, it lengthened or shortened according to the polarity of the field in proportion to the strength of the applied field.

These phenomenons are known as the piezoelectric effect and the inverse piezoelectric effect, respectively, from the Greek word "piezein", meaning to press or squeeze [37].

The composition, shape and dimensions of piezoelectric material can be tailored to meet the requirements of a specific purpose. Ceramics based on of lead zirconate / lead titanate exhibit greater sensitivity, and higher operating temperatures compared to other compositions. Lead Zirconate Titanate (PZT) is currently the most widely used piezoelectric ceramic material [38].

2.2.2.6 Poling

The piezoelectric properties is manifested in a ferroelectric ceramic material after "poling" it [39]. The domains are reoriented and aligned by applying a strong dc electric field, usually at an elevated temperature just below the Curie temperature.

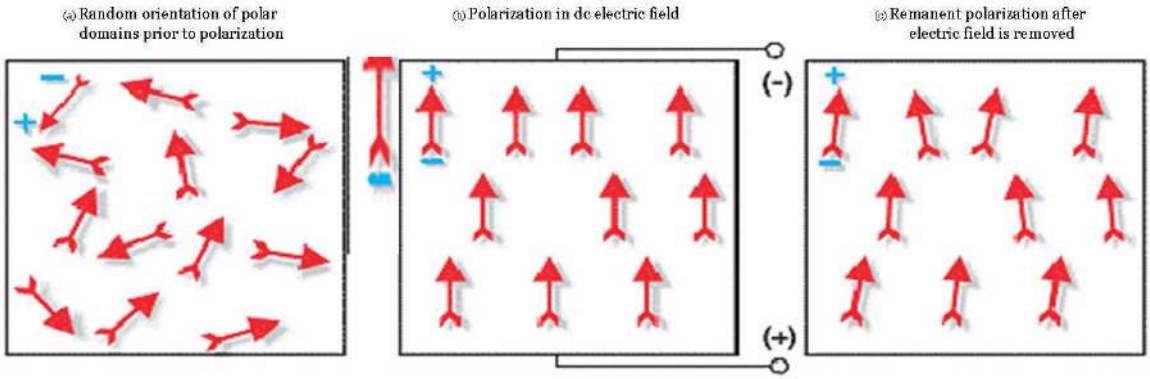

Fig. 2.13 Poling of a ferroelectric ceramic

An illustration of this process is shown in Fig. 2.13. Through this polarizing (poling) treatment, domains that are almost nearly aligned in the direction of the electric field expand at the expanse of the domains that are not favorably aligned relative to the applied field. When the electric field is removed most of the dipoles are

locked into a configuration of "near alignment" (Fig. 2.13 c). The specimen now has a permanent polarization called the remanent polarization.

d_{33} measurement

In the present work, the pellets were electrically poled by applying a high d.c. electric field (10-20 kV/ cm) in silicon oil bath at around 70-80 °C for 8 h. The d_{33} measurements of the samples were done using a piezometer system (PiezoTest PM300, UK) at room temperature.

References

[1] J. S. Reed, *Introduction to the Principles of Ceramic Processing* (John Wiley & Sons, New York, 1988).

[2] D. W. Richerson, *Modern Ceramic Engineering* (Marcel Dekker, New York, 1982).

[3] J. S. Reed and R. B. Runk, *Ceramic fabrication Processes, Treatise on Materials Science & Technology,* Vol. **9** (Editor F. F. Y. Wang, Academic Press, New York, 1976).

[4] K. G. Ewsuk and L.W. Harrison, *Ceramic Powder Science III, Ceramic Transactions*, Vol. **12** (The American Ceramic Society, Westerville, Ohio, 1990).

[5] D. Baker, D.C. Koehler, W. O. Fleckenstein, G. E. Roden and R. Sabia, *Materials Technology, Vol. **II*** (Prentice- Hall Inc., Englewod Cliffs, New Jersey).

[6] W. D. Kingery and B. D. François, *Sintering and related phenomena* (Gordon Breach Science Publishers, New York, 1965).

[7] K. G. Ewsuk and G. L. Messing, *Hot Isostatic Pressing: Theory and Applications* (ASM International Materials Park, Ohio, 1991).

[8] R. L. Coble and J. E. Burke, *Progress in Ceramic Science*, Vol. **3** (Macmillan New York, 1963).

[9] N. B. Hannay, *Reactivity of Solids: Treatise on Solid State Chemistry*, Vol. **4** (Plenum Press, New York, 1976).

[10] B. D. Cullity, *Elements of X- ray Diffraction* (Addison –Wesley Publishing Co.Inc., California, 1978).

[11] S. O. Kasap, *Principles of Electronic materials and Devices*, 2nd Edition (Tata McGraw- Hill Inc., New York, 2002).

[12] R. K. Puri and V. K. Babbar, *Solid State Physics* (S. Chand & CO. Ltd., New Delhi, 2001).

[13] V. Shrivastava, A. K. Jha and R. G. Mendiratta, Solid state Comm. **133**, 125, (2005).

[14] B. Su and W. Button, J. Appl. Phys. **95,** 1382 (2004).

[15] K. Uchino, *Ferroelectric Devices* (Marcel Dekker Inc., New York, 2000).

[16] C. Dong, *J. Appl. Cryst*. **32** , 838, (1999).

[17] H. A. Bowman and R. M. Schoonover, *J. Res. Nat. Bur. Stand*., **69 C**, 217, (1965).

[18] H. D. Megaw, *Ferroelectricity in Crystals* (Methen & Co. LTD., London, 1957).

[19] W. Kanzig, *Ferroelectric and Antifreeoelectrics* (Academic Press, New York, 1957).

[20] F. Jona and G. Shirane, *Ferroelectric Crystals* (Pergamon Press, Oxford, London, 1962).

[21] J. C. Burfoot, *Ferroelectrics* (Van Nostrand, New York, 1967).

[22] J. B. Grindlay, *An Introduction to Phenomenological Theory of Ferroelectricity* (Pergamon Press, Oxford, London, 1970).

[23] J. C. Anderson and K. D. Leaver, *Materials Science* (Thomas nelson & Sons Ltd., London, 1969).

[24] Y. H. Xu, *Ferroelectricity Materials* (Elsevier Science Publisher, Amsterdam, 1991).

[25] R. C. Buchanan, *Ceramic Materials for Electronics: Processing, Properties & Applications* (Marcel Dekker inc., New York, 1991).

[26] S. B. Lang, *Source Book of Pyroelectricity* (Gordon & breach Science Publishers, New York, 1965).

[27] R. M. Rose, L. A. Shepard and J. Wulff, *Electronic properties* (Wiley eastern Pvt. Ltd., New York, 1965).

[28] C. Kittle, *Introduction to solid State Physics*, 7th edition (John Wiley & Sons Inc., New Jersey, 1996).

[29] B. Tareev, *Physics of Dielectic Materials* (Mir Publishers, Moscow, 1979).

[30] I. Bunget and M. Popenscu, *Physics of Solid Dielectrics* (Elsevier, New York, 1984).

[31] Y. I. Frenkel, Elecktrichestro (Physics of Electrets), **8** (1974) 5.

[32] I. S. Zheludev, *Physics of Crystalline dielectrics: Crystallography and Spontaneous polarization*, Vol. I (Plenum press, New York, 1971).

[33] R. N. P. Choudhary and A. K. Thakur, *Complex impedance Analysis: A tool for ferroelectric Materials* (Proceedings of NSFD – XIII) Nov. 23-25, 2004.

[34] E. Barsoukov and J. R. Macdonald, *Impedance Spectroscopy: theory, experiment and applications* (John Wiley & Sons Inc., New Jersey, 2005).

[35] W. P. Mason, *Piezoelectric Crystals and their Application to Ultrasonics* (Van Nostrand, New York, 1950).

[36] C. B. Sawyer and C. H. Tower, *Phys. Rev*. **35**, 269 (1930).

[37] S. Ikegami & I. Ueda, *Jpn. J. Appl. Phys*., **13**, 1572, (1974)

[38] H. Jaffe & D. A. Berlincourt, *Proc. IEEE*, **53**, 1372 (1965)

[39] G. H Heartling, *J. Am. Ceram. Soc*. **82**, 797, (1999)

Chapter 3

Chapter 3

Optimization of Preparation Conditions

3.1 Introduction

Optimization of preparation conditions is essential for getting enhanced microstructural, dielectric and ferroelectric properties of the synthesized compounds [1-6]. Therefore, the calcination temperature, sintering temperatures and sintering durations for the preparation of a compound by solid-state reaction method is very important. Beside these sintering conditions, knowledge of reaction kinetic parameters such as reaction rate and activation energy are very important for the determination of the reaction mechanism. Generally, the ferroelectric compositions are synthesized by chemical reaction between mixed oxides, hydroxides or carbonates in a temperature range of 600 °C to 1600 °C [7-10]. The characteristics of synthesized compounds are dependent on the heat treatment conditions, such as processing temperature, rate of heating, soaking time and activation energy [10-11]. The effect of sintering temperature, duration and rate of heating on the microstructure, dielectric, conductivity, ferroelectric and piezoelectric properties of $BaTi_{0.85}W_{0.15}O_3$ compound have been investigated with an objective of identifying the optimized sintering conditions. The optimized sintering condition is one which results in high dielectric constant, low dielectric loss, good ferroelectric and piezoelectric properties and maintaining the desired pervoskite phase. In order to optimize the preparation conditions, $BaTi_{0.85}W_{0.15}O_3$ compound was synthesized by

varying sintering temperature and durations and rate of heating. This optimized calcination, sintering and rate of heating effect were used to prepare all the tungsten substitution barium titanate and barium strontium titanate specimens discussed in the following chapters.

3.2 Results and Discussions

3.2.1 Optimization of Sintering Condition

3.2.1.1 Structural Characterization

(i) X-ray diffraction

Samples of composition $BaTi_{0.85}W_{0.15}O_3$ were calcined at 1150 ^oC for 2 hours and sintered at 1200 ^oC, 1250 ^oC and 1300 ^oC for 2 hours and 5 hours. The X-ray diffractograms of the samples sintered at various temperatures are shown in Fig. 3.1.

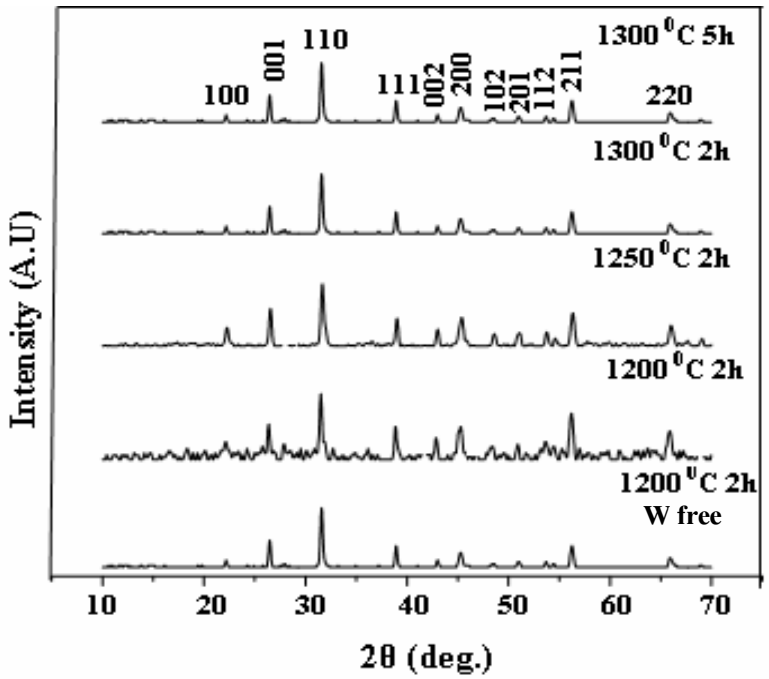

Fig. 3.1 XRD patterns of sintered samples at different temperatures and durations

It is observed that tetragonal pervoskite structure is formed in the samples. The strongest peak in all the diffraction patterns is near $2\theta = 31^{o}$ corresponding to the line (110). However, some additional peaks are seen in the sample sintered at 1200 ^{0}C for 2h which is possibly due to the unreacted tungsten oxide but disappear when the sample is sintered at higher temperature. A small variation in position of peaks is observed in the samples indicating changes in the lattice parameters.

Lattice Parameters

The peaks have been indexed using the observed interplanar spacing d and the lattice parameters so obtained were refined using the least square refinement method by a computer program Powder-X [12]. The lattice parameters, unit cell volume and tetragonal strain (c/a) calculated for $BaTi_{0.85}W_{0.15}O_3$ compound is observed to decrease with increase in sintering temperature. The decreased cell volume and lattice parameter implies that the substituted W ion exists in a oxidation state of +6, as the size of W^{6+} is smaller than Ti^{4+}. It is also observed that for the above mentioned sintering conditions the samples at room temperature have tetragonal pervoskite structures.

Table 3.1: Variation of lattice parameters, tetragonal strain, co-ordination number, unit cell volume and density at different sintering conditions

Sintering conditions	**a (A^o)**	**c (A^o)**	**c/a**	**Volume $(A^o)^3$**	**Ionic radii**	**Density (g/cc)**	**CN**
1200 ºC 2 h W- free	3.999	4.038	1.009	64.57	Ti^{4+}= 0.68	6.031	6
1200 ºC 2 h	3.996	4.031	1.008	64.36	W^{6+}= 0.60	6.025	6
1250 ºC 2 h	3.994	4.019	1.006	64.11		6.030	
1300 ºC 2 h	3.986	4.012	1.005	63.74		6.016	
1300 ºC 5 h	3.984	4.002	1.004	63.52		6.008	

(ii) SEM Analysis

Fig. 3.2 (a)-(e) shows the surface morphology of the samples sintered at different sintering conditions using scanning electron microscope.

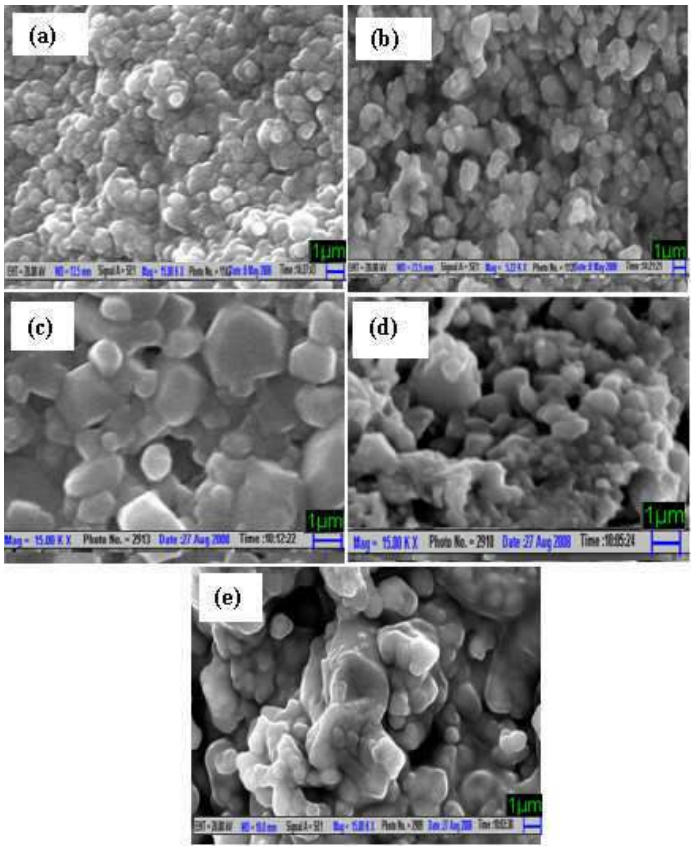

Fig. 3.2 SEM micrographs of the samples sintered at (a) 1200 ^{o}C; 2h W-free (b) 1200 ^{o}C; 2h (c) 1250 ^{o}C; 2h (d) 1300 ^{o}C; 2h (e) 1300 ^{o}C; 5 h

It is observed that there is increase in grain size when sintering temperature is increased to 1250 ^{0}C. The average grain size is observed to be in the range of 0.5 -2.5 μm. At higher sintering temperature grain boundaries are not sharp and partial melting of grains is observed. The observed variations in the average grain size and morphology can be correlated with observed density as shown in Table 3.1. It is reported that variation of density due to variation in sintering temperatures can be associated with two factors, grain size and porosity [13, 14]. At sintering temperature 1250 ^{o}C the observed increase in density is basically due to larger grain size and a packed structure.

3.2.1.2 Electrical Characterization

(i) Dielectric Studies

The dielectric properties including the dielectric constant (ε') and dielectric loss (tan δ) have been studied. The variation of ε' and tan δ as a function of temperature at 100 Hz, 1 kHz, 10 kHz and 100 kHz frequencies and the variation of ε' and tan δ with frequency at room temperature for different sintering conditions were measured and is presented below.

Variation of ε' with Temperature: Curie Temperature

Fig. 3.3 shows the temperature dependence of dielectric constant at 100 Hz, 1 kHz, 10 kHz, 100 kHz for the samples sintered at different sintering conditions. For all the sintering conditions, the compound show dielectric anomaly at a temperature called the Curie temperature (T_c) indicating the occurrence of ferroelectric-paraelectric phase transition. The Curie temperature is the same at all the frequencies indicating the non-relaxor behavior of the compounds at all the sintering conditions.

It is seen that the dielectric constant increases as the sintering temperature increases in the tungsten containing sample and decreases at higher sintering duration. It is known that in barium titanate oxygen vacancies are major structural defects [15]. These vacancies are produced due to the loss of oxygen during sintering at high temperature in accordance with the following equation [16].

$$O_o \rightarrow \frac{1}{2}O_2 + V_o^{\bullet\bullet} + 2e^-$$

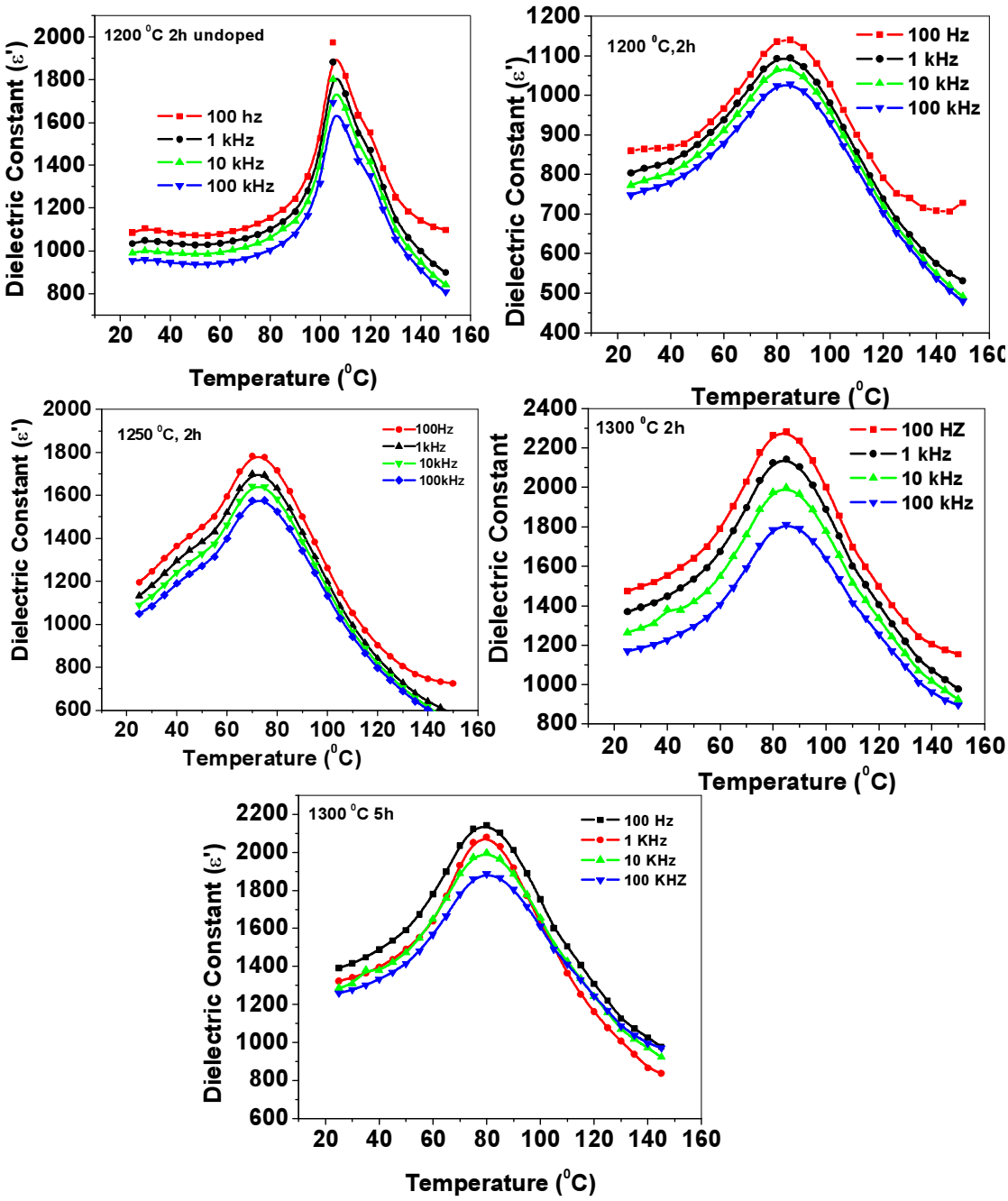

Fig. 3.3 Variation of dielectric constant (ε') with temperature at different sintering conditions

The above equation is in accordance with Kroger – Vink notation of defects [17]. These oxygen vacancies $V_o^{\bullet\bullet}$ act as doubly positively charged ion above 850 K and singly ionized at room temperature [18]. These defects act as space charge [19]. As sintering temperature and duration is increased more and more oxygen vacancies

are formed. The increase in dielectric constant value is known to depend on the number of oxygen vacancies [20].

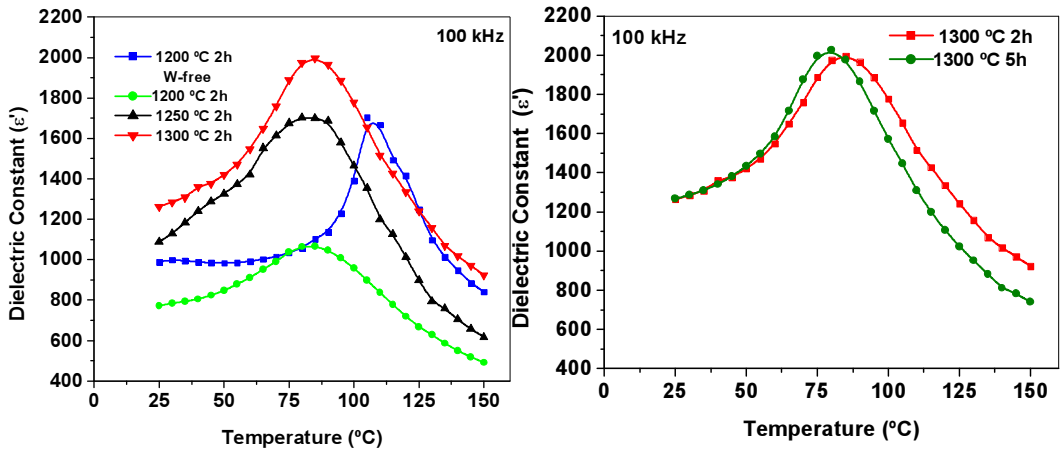

Fig. 3.4 Variation of dielectric constant (ε') with temperature at 100 kHz

Also, the variation of dielectric constant (ε') with temperature at 100 kHz is plotted in Fig. 3.4. It is observed that the Curie temperature decreases in tungsten substituted samples. The reduction of Curie temperature is due to the decrease in bond strength between W-O as compared to Ti-O. This decrease in bond energy leads to weaker distortion of octahedron, which also decrease c/a ratio, resulting in the decrease in Curie temperature [21].

In the samples, the broad dielectric peaks indicate the diffuse nature of the phase transition. The diffusivity constant or degree of disorderness (γ) has been calculated using the following formula [22]:

$$\ln (1/\varepsilon - 1/\varepsilon_{max}) = \gamma \ln (T - T_c) + \text{constant} \qquad (3.1)$$

where ε_{max} is the maximum value of ε at T = T_c. The values of γ have been calculated from the slopes of ln (1/ ε – 1/ ε_{max}) versus ln (T- T_c) curve (Fig. 3.5) and are given in Table 3.2. For all the samples, γ is found to be between 1 (obeying Curie-Weiss law) and 2 (for completely disordered system) confirming the diffuse phase transition in all the samples.

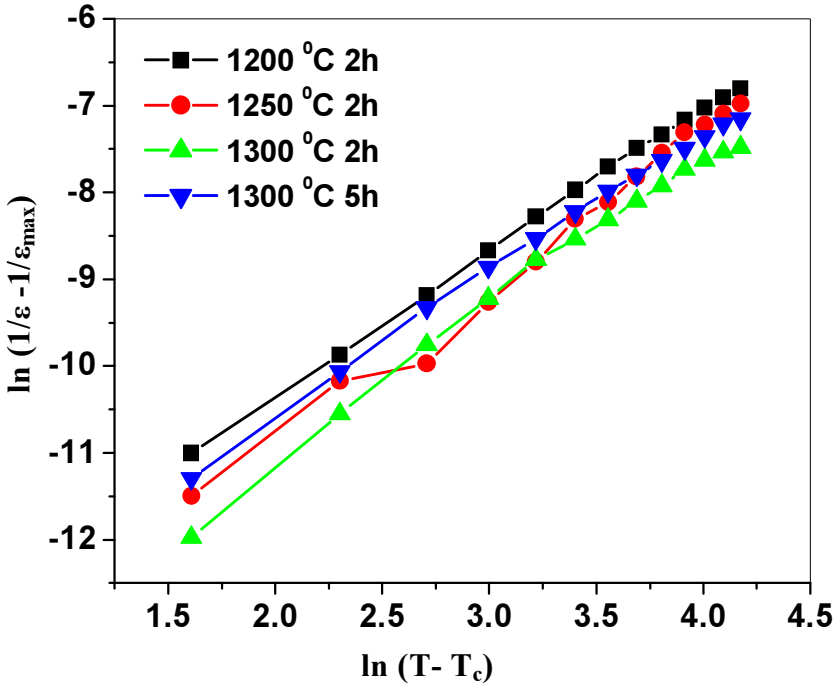

Fig. 3.5 Variation of ln $(1/\varepsilon - 1/\varepsilon_{max})$ with ln $(T-T_c)$ at different sintering conditions

Table 3.2 Values of diffusivity constant (γ) at different sintering conditions

Sintering Conditions	Diffusivity Constant (γ)
1200 ^{0}C;2h	1.65
1250 ^{0}C;2h	1.75
1300 ^{0}C; 2h	1.74
1300 ^{0}C; 5h	1.59

Variation of Dielectric Loss with Temperatures: tan δ

Fig. 3.6 shows the variation of dielectric loss (tan δ) with temperature at frequencies 100 Hz, 1 kHz, 10 kHz and 100 kHz for different sintering conditions.

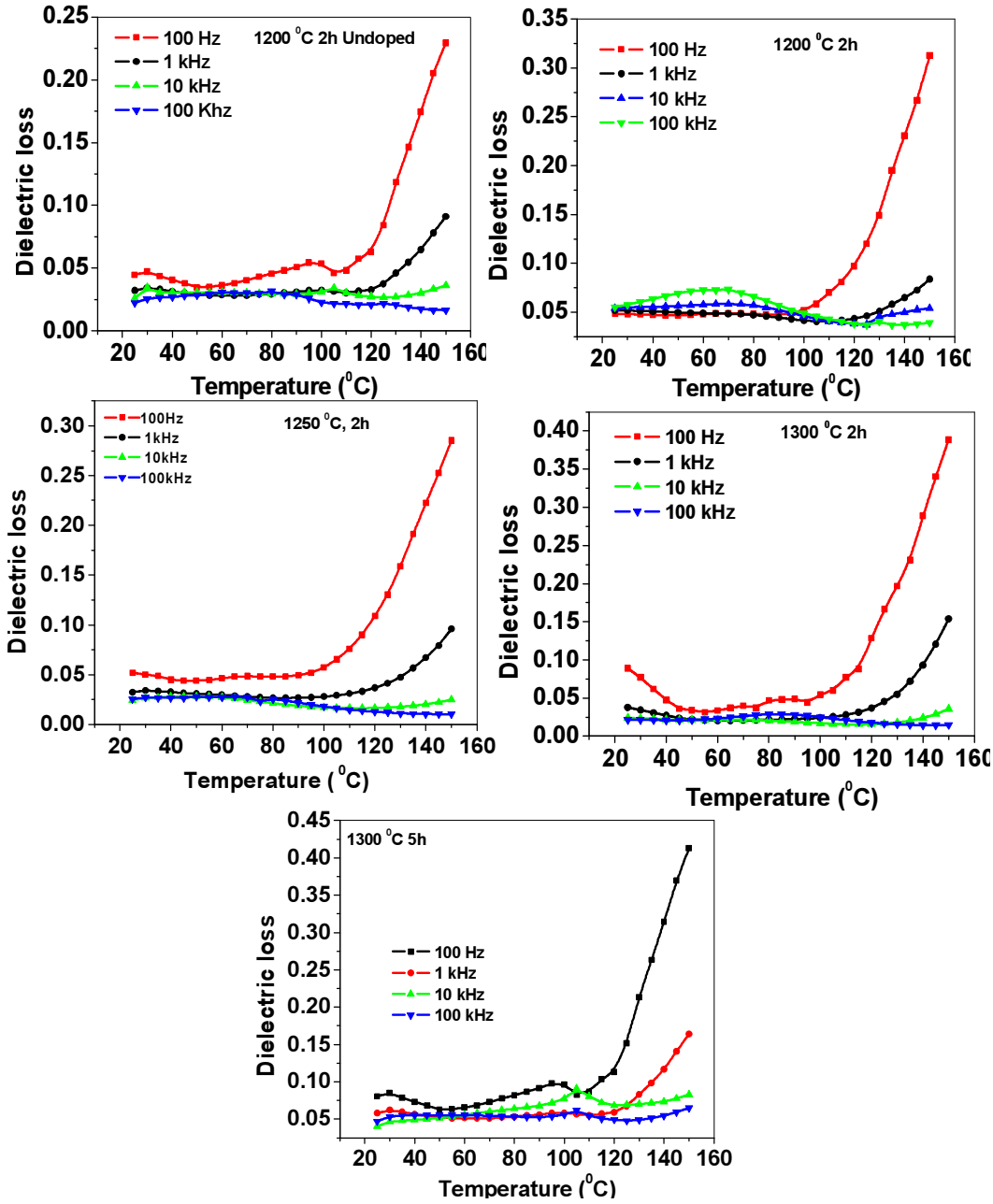

Fig. 3.6 Variation of dielectric loss with temperature at different sintering conditions

It is observed that the loss initially remains almost independent of temperature upto nearly 90 °C and thereafter it increase with the increase in temperature. This sharp increase in dielectric loss in high temperature region may be attributed to the increased mobility of space charges arising from the oxygen vacancies or defects in the samples [23].

To see the effect of sintering temperature and duration on the variation of dielectric loss with temperature, the curves have been plotted in Fig. 3.7 at 100 kHz. It is observed that loss decreases in the samples sintered at 1250 ^{0}C for 2h and increases at higher sintering temperature and duration. The source of dielectric loss in these materials is the space charge polarization / domain wall relaxation [24]. It is known that the space charges which exist as oxygen vacancies are primarily responsible for an appreciable increase in dielectric loss. Also, on increasing sintering temperature and duration, loss increases as oxygen vacancies induced polarization becomes dominant [25].

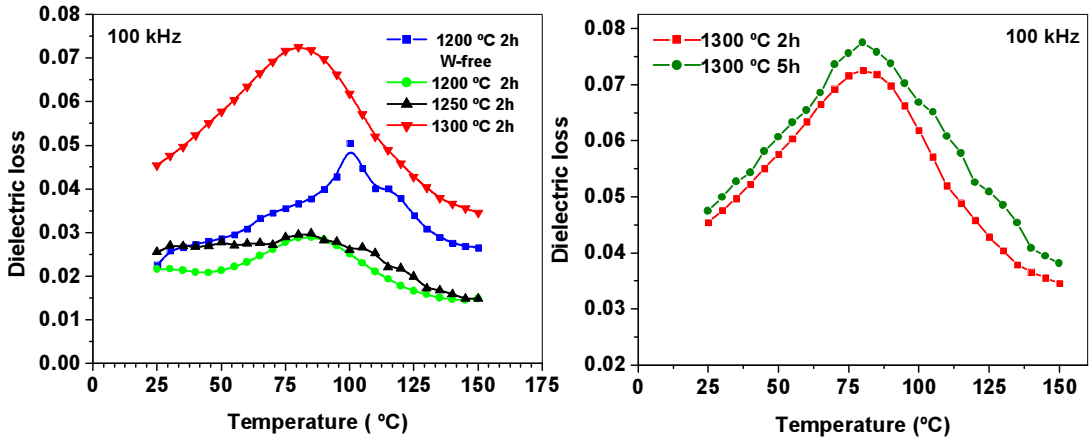

Fig. 3.7 Variation of dielectric loss with temperature at 100 kHz

Variation of ε_r and tan δ with Frequency

Fig. 3.8 and Fig. 3.9 show the variation of dielectric constant (ε′) and dielectric loss (tan δ) as function of frequency in the range from 20 Hz to 1 MHz at room temperature respectively.

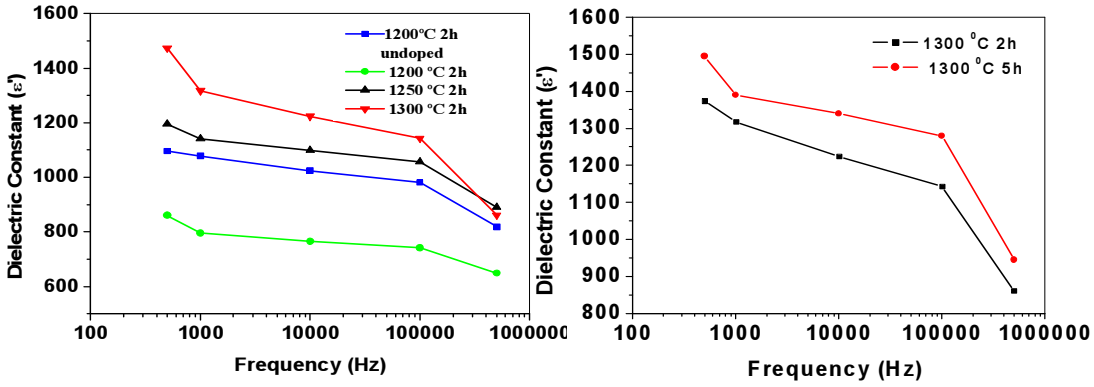

Fig. 3.8 Variation of dielectric constant (ε′) with frequency

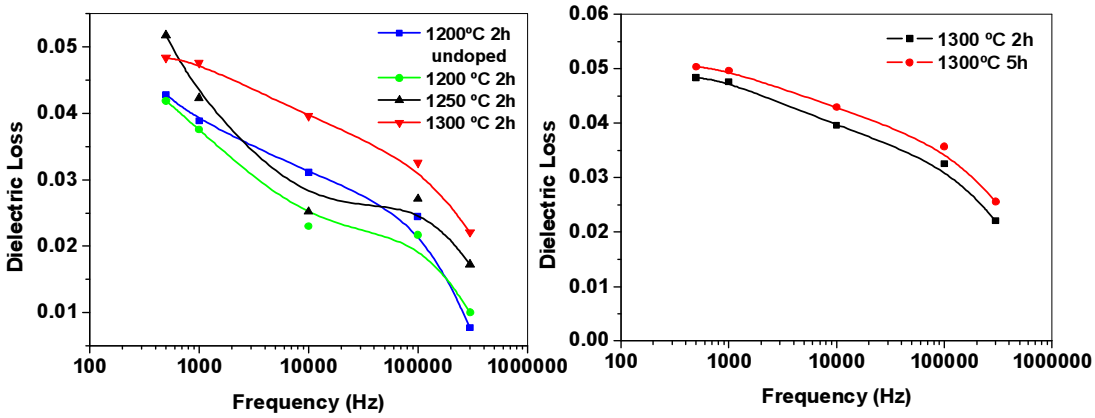

Fig. 3.9 Variation of dielectric loss (tan δ) with frequency

It is observed in all the studied samples both the dielectric constant and dielectric loss decreases upto about 1 kHz and remains nearly constant beyond this frequency. The dielectric constant of a material has polarization contributions from electronic, ionic, dipolar and space charge [26]. Response frequencies for ionic and electronic polarizations are ~ 10^{13} and 10^{15} Hz, respectively; and at frequencies beyond 1 kHz, contribution from space charge polarization is not expected [26]. Thus, the higher values of dielectric constant at lower frequencies can be attributed to the presence of defects such as oxygen vacancies, $V_o^{\bullet\bullet}$. These vacancies act as space charge which plays an important role in the polarization at lower frequencies [27, 28].

Moreover, at lower frequencies, the dipoles can follow the field resulting in higher values of dielectric constant while at higher frequencies, the dipoles are unable to follow the rapidly changing field leading to the reduction in the values of dielectric constant.

The observed variation of dielectric loss can also be understood as explained above because the source of dielectric loss in insulating ceramics is space charge polarization and / or domain wall relaxation [24]. Higher value of dielectric loss at lower frequency can be understood in terms of oxygen vacancies which act as space charge whose contribution as space charge polarization is dominant in lower frequency [26].

(ii) DC Conductivity

Fig. 3.10 shows the variation of dc resistivity as a function of temperature at different sintering temperatures. The curves show PTCR behaviour. The resistivity increases on tungsten substitution. The observed variation can be understood as follows. When W^{6+} ions substitute in $BaTiO_3$ lattice, the defect equation is

$$Ba^{2+}Ti^{3+}_{x}Ti^{4+}_{1-x}W^{6+}O_3 \qquad (3.2)$$

in the above equation Ti^{3+} makes low donor energy level and in Ti^{4+} ($Ti^{3+} \leftrightarrow Ti^{4+} + e^-$) electrons can contribute to conduction by jumping over the potential barriers at grain boundaries. The potential barrier height at the grain boundary is closely related with the PTCR property [29]. It is dependent on the degree of charge compensation and can increase the electrical resistivity.

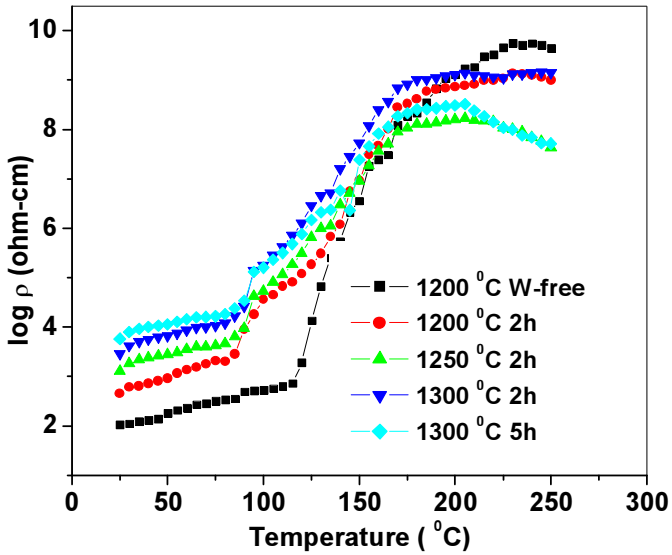

Fig. 3.10 Variation of dc resistivity with temperature at different sintering temperatures

When the sample is sintered at higher temperature, higher number of oxygen vacancies is formed in the specimen, these oxygen vacancies involving conduction electron make W-doped barium titanate ceramic semiconducting. The conduction electrons are generated from the oxygen vacancies as per following equation;

$$O_0 \leftrightarrow \tfrac{1}{2} O_2 + V^{\circ\circ}{}_0 + 2e^- \qquad (3.3)$$

The PTCR behaviour is the due to the negative charge carrier conduction under the external electric field [30].

(iii) Ferroelectric Studies

Fig. 3.11 shows the room temperature P-E hysteresis loops of $BaTi_{0.85}W_{0.15}O_3$ compound sintered at different sintering conditions. The corresponding values of remanent polarization (P_r) and coercive field (E_c) are given in Table 3.3. On comparing the loops, it is observed that a well- saturated hysteresis loop is obtained in the sample sintered at 1250 ^{0}C for 2 hrs having lower coercive field.

It is known that ferroelectric properties are affected by the composition, microstructure and lattice defects like oxygen vacancies in the structure of the materials [30-31]. A densely packed microstructure with uniformly distributed grains and distinct grain boundaries in the sample results in the formation of well-defined hysteresis loop. In soft ferroelectric materials, with higher- valent substituent, the defects are cation vacancies. Higher valent substituent and associated cation vacancies tend to form dipolar defects and random field around these dipolar defects lowers the activation barrier required for the nucleation of new domains, leading to lower E_c [32, 33].

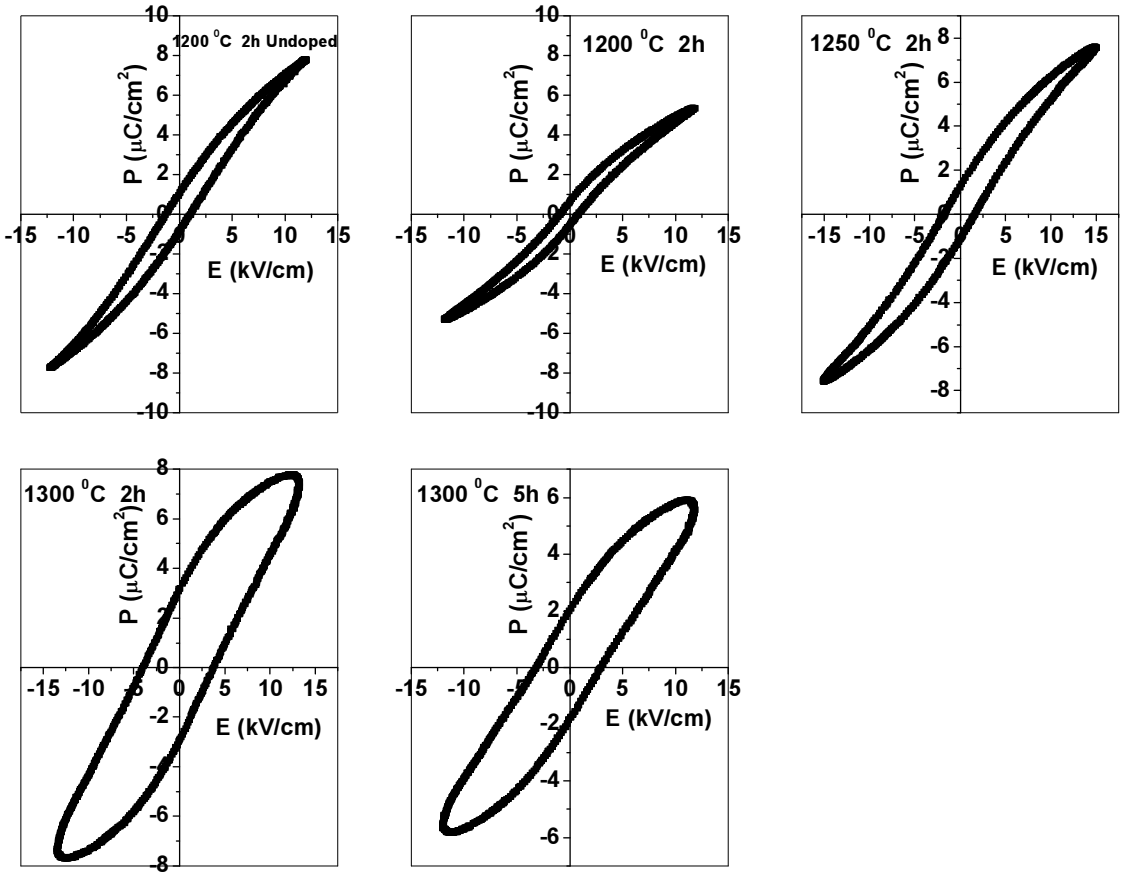

Fig. 3.11 P-E Hysteresis loops of the studied samples

Table 3.3 P_r and E_c values of the samples sintered at different sintering conditions

Sintering Temperature	P_r (μC/cm^2)	E_c (kV/cm)
1200 ^{0}C 2 h undoped	1.37	1.11
1200 ^{0}C 2h	1.04	1.15
1250 ^{0}C 2h	1.80	2.20
1300 ^{0}C 2h	3.35	3.51
1300 ^{0}C 5h	2.12	2.70

Temperature Variation of P-E Hysteresis Loops

Fig. 3.12 shows the temperature variation of the P-E hysteresis loops of $BaTi_{0.85}W_{0.15}O_3$ compound sintered at different sintering temperature.

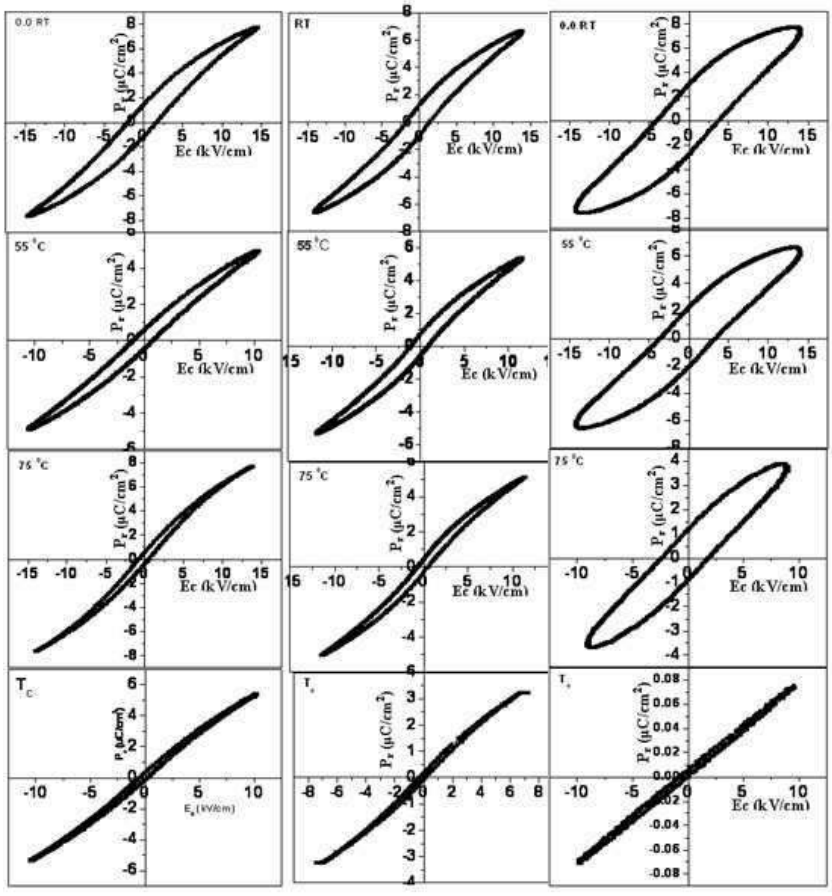

(a) (b) (c)

Fig. 3.12 Temperature variation of P-E hysteresis loops of $BaTi_{0.85}W_{0.15}O_3$ at (a) 1200 ^{0}C for 2h W-free (b) 1200 ^{0}C for 2h (c) 1300 ^{0}C for 2 h

It is observed that on increasing temperature from room temperature to Curie temperature polarization decreases and no loop is obtained at the Curie temperature which indicates that the samples become paraelectric at Curie temperature.

(iv) Piezoelectric Studies

Table 3.4 shows the piezoelectric coefficient, d_{33}, of the $BaTi_{0.85}W_{0.15}O_3$ samples sintered at different temperature and duration. It is observed that d_{33} value increases with increase in sintering temperature to 1250 ^{0}C. The maximum observed value of d_{33} is 112.87 pC/N.

Table 3.4 Piezoelectric coefficient (d_{33}) at different sintering temperature

Sintering conditions	**Piezoelectric coefficient (d_{33}) pC/N**
1200 ^{0}C 2h W-free	87.52
1200 ^{0}C 2h	76.89
1250 ^{0}C 2h	112.87
1300 ^{0}C 2h	110.21
1300 ^{0}C 5h	107.54

The Piezoelectric coefficients have been reported to increase with increase in grain size [34]. Since in the present work, the grain size increases on increasing the sintering temperature, it is reasonable to believe that it is the increased grain size which increase the observed d_{33} values.

3.2.2 Effect of Heating Rate on Properties

3.2.2.1 Structural Characterization

(i) X-ray Diffraction

Samples of composition $BaTi_{0.85}W_{0.15}O_3$ were calcined at 1150 ^{0}C for 2 hrs and sintered at 1250 ^{0}C for 2 hrs at various heating rates. The room temperature X-ray

diffractograms of the studied samples are shown in Fig. 3.13. It is observed that the perovskite tetragonal structure is formed in all the samples. A small variation in the position of peaks is observed in the samples which is due to change in lattice parameters.

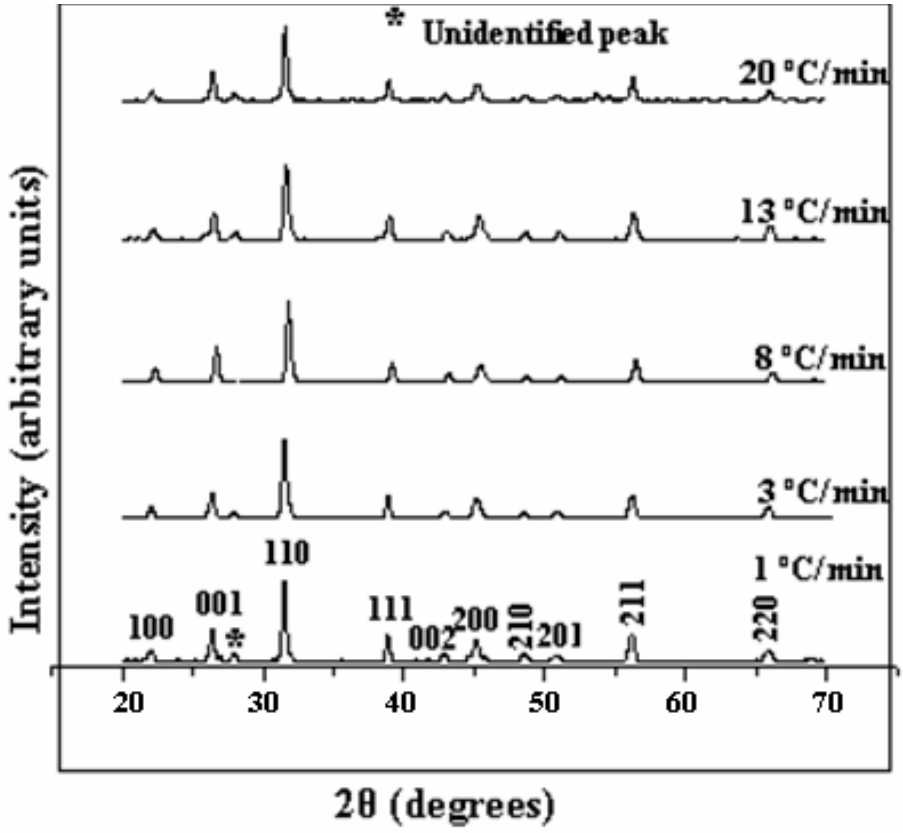

Fig. 3.13 XRD patterns of the studied samples at various heating rate

Also, it is important to note that after (001) peak, an unidentified peak representing some secondary phase is present in all the samples except the one prepared at a heating rate of 8 ^{0}C/min.

Tetragonal Strain (c/a)

Variation of tetragonal strain (c/a) of the sample sintered with various heating rate is shown in Fig. 3.14. It is observed that tetragonal strain decreases from 1.0045 to

1.0005 as the heating rate is increased from 1 ^{0}C/min to 8 ^{0}C/min. However, beyond this heating rate the tetragonal strain again increases to 1.0032 as the heating rate is increased to 20 ^{0}C/min.

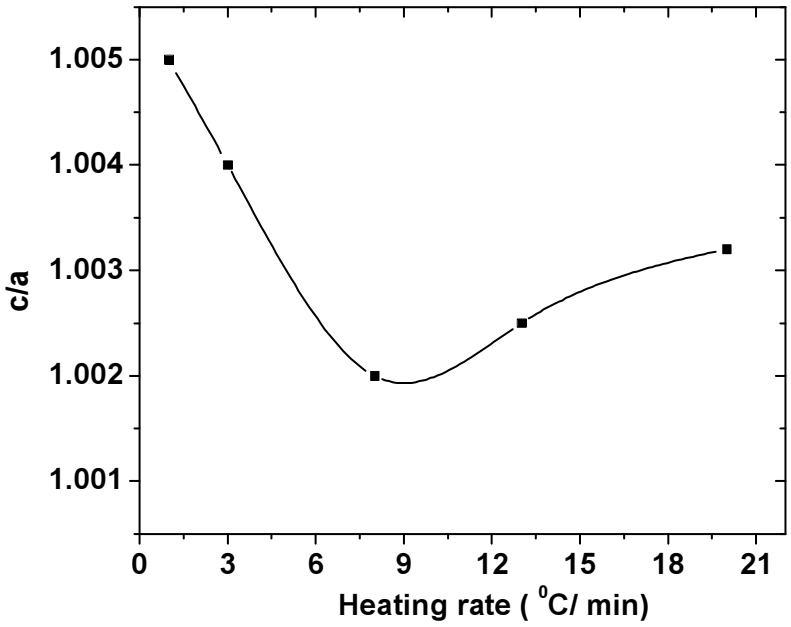

Fig. 3.14 Variation of tetragonal strain at various heating rates

(ii) SEM Analysis

Fig. 3.15 (a) - (e) shows the surface morphology of the samples with varied heating rates using scanning electron microscope. The grain size becomes fairly uniform with clear grain boundaries as heating rate is increased from 1 to 8 ^{0}C/min. It is also clearly observed that at the higher heating rate the edges of grains are not so sharp and the grains are observed to be inter-diffusing into each other. Grain size was calculated by linear intercept method and they are found to be in the range 0.5-1.5 μm. A careful observation of the values of the densities (Table 3.5) and SEM micrographs reveal that the specimen sintered at higher heating rate has lower density due to a porous microstructure.

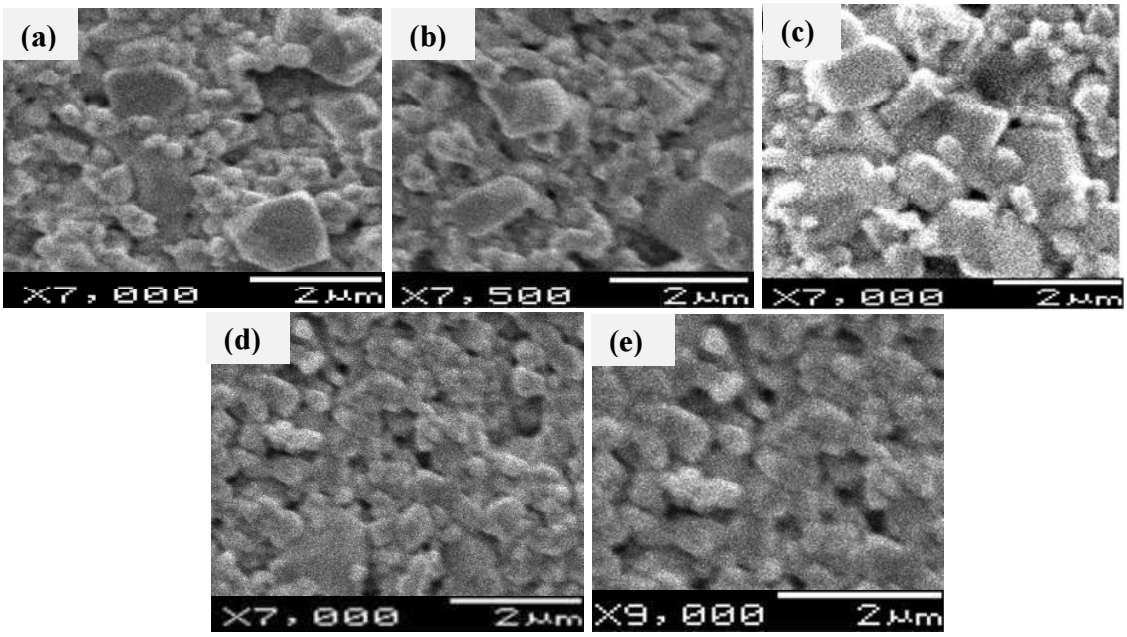

Fig. 3.15 Scanning Electron Micrographs of the studied samples with heating rate of (a) 1^0C/min, (b) 3 ^{0}C/min, (c) 8 ^{0}C/min, (d) 13 ^{0}C/min and (e) 20 ^{0}C/min.

3.2.2.2 Electrical Characterization

(i) Dielectric Studies

Fig. 3.16 shows the variation of dielectric constant (ε') and dielectric loss (tan δ) with temperature at 100 Hz, 1 kHz, 10 kHz and 100 kHz of the samples sintered with varied heating rates. It is observed that all the samples have same T_c at all the above mentioned frequencies, suggesting that the specimens do not show any relaxor behaviour. It is also observed that dielectric constant as well as dielectric loss decreases with increasing frequency. It can be understood as follows. The dielectric constant of a material has four polarization contributions: electronic, ionic, dipolar and space charge [24]. Response frequencies for ionic and electronic polarizations are ~ 10^{13} and 10^{16} Hz, respectively; and at frequencies beyond 1 kHz, contribution from space charge polarization is not expected [24].

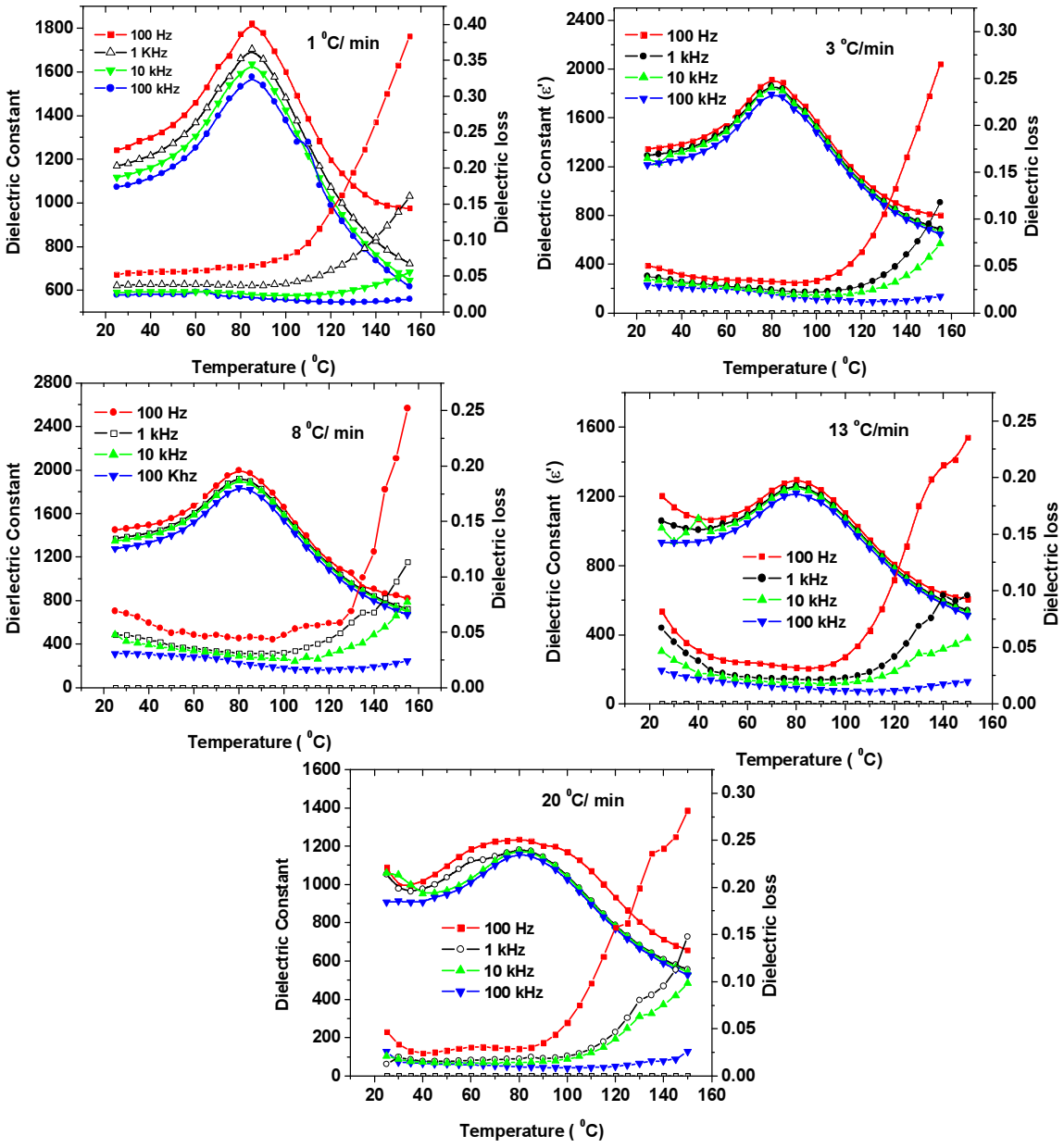

Fig. 3.16 Variation of dielectric constant (ε') and dielectric loss (tan δ) with temperature of the specimens sintered with varied heating rates at 100 Hz, 1 kHz, 10 kHz, 100 kHz frequencies

Thus, the higher values of dielectric constant at lower frequencies can be attributed to the presence of defects such as oxygen vacancies. These vacancies act as space charge which plays an important role in the polarization at lower frequencies [25, 26]. At lower frequencies, the dipoles can follow the field resulting in higher

values of dielectric constant while at higher frequencies; the dipoles are unable to follow the rapidly changing field leading to the reduction in the values of dielectric constant. Increase in dielectric constant is observed as the heating rate increases upto 8 ^{0}C/min and decreases with heating rate above 8 ^{0}C/min. It is known that dielectric properties of a specimen are affected by both crystalline structure of the phase and its microstructure [35]. It is known that the variation of tetragonality (c/a) is an indirect measure of dielectric constant in a ferroelectric material [36]. Also, a decrease in c/a is reported to be related to a increased dielectric constant [37, 38].

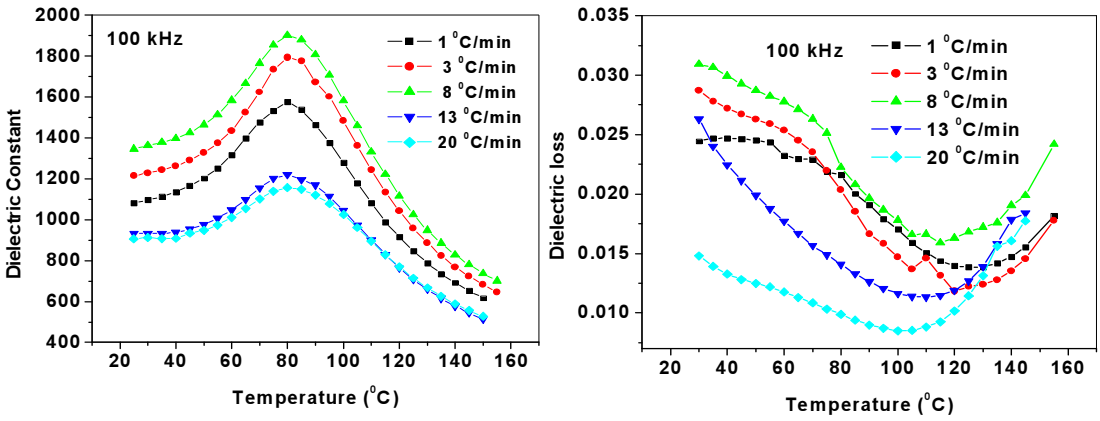

Fig. 3.17 Variation of dielectric constant (ε') and dielectric loss (tan δ) at 100 kHz at different heating rate

This decrease in tetragonality leads to 90^0 domain orientations thereby increasing dielectric constant. The increase in dielectric constant can also be explained by increased grain size of the specimen [39, 40]. It is also believed that when the grain size is large and fairly distributed, the domain wall movement is relatively easier and regular increasing the dielectric constant. For all the samples studied at the above mentioned frequencies (Fig. 3.16) the loss is almost constant in lower temperature region but at higher temperature region it increases sharply. This sharp increase of dielectric loss in high temperature region may be attributed to the increased mobility of space charges [21].

In all the samples, the broad dielectric peaks indicate the diffuse nature of the phase transition. The diffusivity constant or degress of disorderness (γ) has been calculated using the formula [22]:

$$\ln (1/\varepsilon - 1/\varepsilon_{max}) = \gamma \ln (T-T_c) + \text{constant} \qquad (3.4)$$

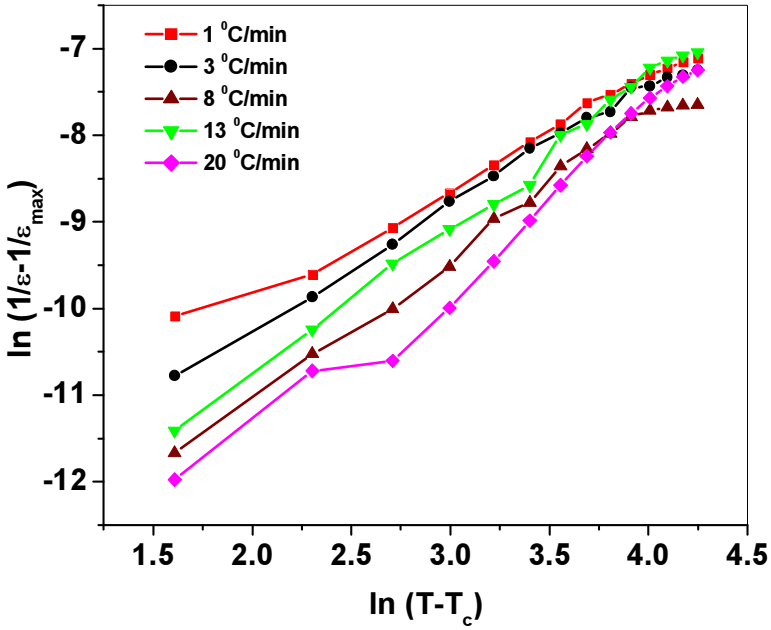

Fig. 3.18 Variation of ln (1/ ε – 1/ ε_{max}) as a function of ln (T- T_c) in the sample sintered with varied heating rate.

where ε'_{max} is the maximum ε′ value at T = T_c. The value of γ have been obtained from the slope of ln (1/ ε – 1/ ε_{max}) versus ln (T- T_c) curve and are listed in Table 3.5.

Table 3.5 Values of density, dielectric constant, remanent polarization and diffusivity parameters of the studied samples

Heating rate (^{0}C/min)	Density (gm/cc)	Dielectric constant (ε')	$2P_r$ (μC/cm^2)	$2E_c$ (kV/cm)	Diffusivity (γ)
1	6.53	1703.37	3.72	24.02	1.23
3	6.51	1913.74	5.96	37.96	1.38
8	6.55	1997.41	6.72	32.28	1.61
13	6.46	1295.45	3.08	20.32	1.71
20	6.42	1181.85	1.62	10.94	1.91

The value of diffusivity increase with increasing heating rate indicating disorderness in the system.

(ii) Ferroelectric Studies

The P-E loops of the studied specimen, recorded at room temperature, at a frequency of 100 Hz, are shown in Fig. 3.19. The observed values of remanent polarization ($2P_r$) and the coercive field ($2E_c$) for all the compounds are given in Table 3.5. It is observed that $2P_r$ first increases with heating rate but decreases at higher heating rate. The maximum observed value of $2P_r$ is ~ 6.72 $\mu C/cm^2$ in the sample prepared with heating rate of 8 ^oC/min.

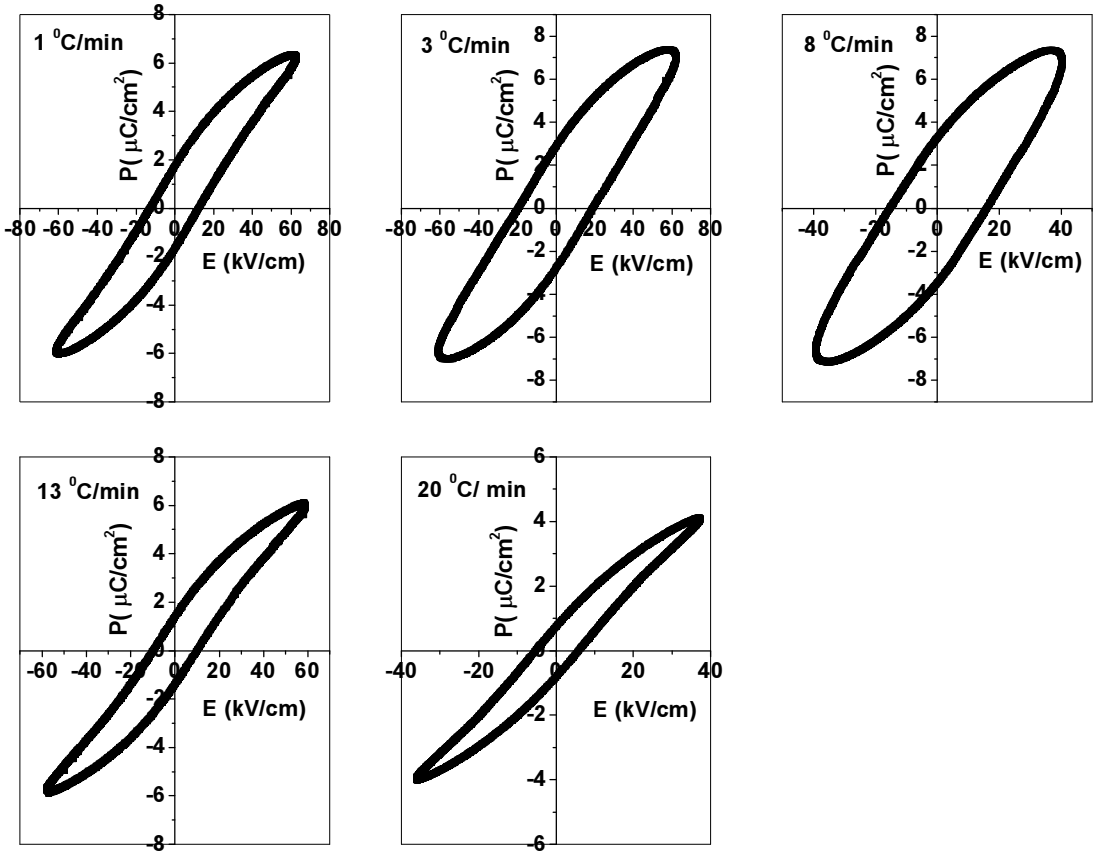

Fig. 3.19 P-E hysteresis loops of the studied samples

It is known that ferroelectric properties are affected by microstructural variation, lattice defects and the heating rate of the specimen [41, 42]. The observed reduction in the polarization values at higher heating rate is possibly due to not proper formation of the grains and the presence of secondary phase making the polarization reversal difficult. The hysteresis loops, look rather lossy, and the loss indicated by the area of the loops, decrease with the increasing heating rate. The lossy nature of the observed P-E loops may be attributed to the porous microstructure and the presence of secondary phase. Further, in the specimen synthesized with higher heating rate, it is likely that there will be lesser number of oxygen vacancies which is possibly the reason for the observed lower loss, as manifested by the area of the P-E loop as well as the measured value of loss (Fig. 3.17), in the sample synthesized at higher heating rate.

3.3 Conclusions

Based on the above observations and discussions the following conclusions can be drawn.

- Tetragonal perovskite structure is formed in the samples.
- Scanning electron micrographs indicate that the average grain size is in the range of 0.5 -2.5 μm
- The unit cell volume and tetragonal strain decrease on increasing sintering temperature and duration.
- Curie temperature decreases on tungsten substitution.
- Curie temperature remains the same in all the samples at all frequencies indicating non-relaxor behaviour .
- Diffuse kind of ferro-paraelectric phase transitions are observed.

- Dielectric constant as well as loss decreases with increase in frequencies which is a normal behavior in the ferroelectric materials.
- The maximum value of piezoelectric coefficient is observed to be 112.48 pC/N in the sample sintered at 1250 ^{0}C 2h the sample.
- Well defined hysteresis loops are observed in the samples.
- When the temperature approaches Curie temperature, polarization decreases and the ferroelectric phase disappear from the sample.
- X-Ray diffraction patterns confirm the formation of perovskite tetragonal structure in the specimens at different heating rates.
- Dielectric constant increases upto 8 ^{0}C/min and decrease when sintered at higher heating rate.
- Dielectric constant as well as loss decrease with increasing frequency.
- Remanent polarization is highest for the sample sintered with heating rate at 8 ^{0}C/min and decrease at higher heating rate.
- Diffusivity increases on increasing the heating rate.
- From the present work, it is concluded that 1250 ^{0}C is the best sintering temperature and 8 ^{0}C/min is the optimum heating rate.

References

[1] J. W. Kim, J.G. Heinrich, *J. Euro. Ceram. Soc.* **25** (2005) 1637.

[2] H. Kungla and M. J. Hoffmann, *J. Appl. Phys*. **107** (2010) 054111-1.

[3] A. Yang, C.A.Wang, R. Guo, Y. Huang, C.W. Nan, *Ceram. Int.* **36** (2010)549.

[4] B. Su, J.E. Holmes, B.L.Cheng and T.W. Button, *J. Electroceramic*. **9** (2002) 111.

[5] S. M. Rhim, H. Bak, S. Hong and O.K. Kim. *J. Am. Ceram. Soc*. **83** (2000) 3009.

[6] B. Zhang, D.Q.Xiao, W.J. Wu, J. Li,X.L. Huang,Y. Pei, L.Wu, J.G.Zhu and Z. J.He, *IEEE International Symposium on Application of Ferroelectrics,* art. No. 5307593 (2009)1.

[7] Malic B, Cilensek J, Mandeljc M & Kosec M, *Acta Chim. Slov*. **52** (2005) 259.

[8] Waser R, Schneller T, Eifert S H & Ehrhart P, *Ferroelectrics*, **36** (2001) 3.

[9] K. L Yadav & R. N. P. Choudhary, *J. Mater Sci. Lett*. **12** (1993) 561.

[10] R. Tipakontitikul & S. Ananta, *Mater. Lett*, **58**, (2004) 449.

[11] M Cerqueira, R S Nasar, E R Leite, E Longo & J. A Varela, *Ceram. Int.,* **26** (2000) 231.

[12] C. Dong, "PowderX: Window-95 based Program for Powder X-ray diffraction data Processing". *J. Appl Cryst*. **32** (1999) 838.

[13] R. Jain, V. Gupta and K. Sreenivas, *Mat. Sci. Engi*. **B78** (2000) 63.

[14] G. S. Murugan and K. B. R. Varma, *J. Electroceram*., **8** (2002) 37.

[15] Om Prakash, Devendra Kumar, R. K. Dwivedi, K. Srivastava, Prakash, Singh, Sindhu Singh, *J, Mater Sci*, **42** (2007) 5490-5496.

[16] B. I. Neirman, *J. Material Science* **17** (1982) 3510-3524.

[17] F. A Kroger, H. J Vink, *Solid state Physics, Academic Press, New York*, 1956

[18] N. Hirose, J. M. S. Shakle, A.R. West, *Journal of Electroceramics,* **3** (1999) 233- 238.

[19] R. Moos, K. H. Hardlt, *J.Amer.Ceramic Society* **80** (1997) 2549-2562.

[20] D. Bahadur, Om Prakash *J. Solid state Chemistry* **46** (1983) 197-203.

[21] Sheela Devi, Prasun Ganguly, Sameer Jain and A. K. Jha, *Ferroelectric* **381** (2009) 120- 129.

[22] S.M. Pilgrim, A. E. Sutherland and S.R. Winzer, *J. Am. Ceram. Soc*. **73** (1990) 3122.

[23] T. Friessnegg, S. Aggarwal, R. Ramesh, B. Nilesen, E.H. Poindexter and D. J. Keeble, *Appl. Phys. Lett*. **77** (2000) 127.

[24] I.S. Zheludev, *Physics of Crystalline Dielectrics, Vol 1: Crystallography & Spontaneous Polarization (Plenum Press, New York (1971).*

[25] Sining Yun, Xiaoli Wang, Bo Li and Delong Xu, *Solid State Communications* **143** (2007) 461- 465.

[26] R. C. Buchanan, *Ceramic Materials for Electronic: Processing, Properties and Applications (Marcel Dekker Inc., New York, 1986)* 38.

[27] Y. Noguchi and M. Miyayama, *Appl. Phys. Lett*. **78** (2001) 1903.

[28] A. Chen, Y. Zhi and L.E. Cross, *Phys. Rev. B* **62** (2000) 228.

[29] S.W Ding, G. Jia, J. Wang, Z.Y He, *Ceramics International,* In press 2007.

[30] Y.H. Xu (Ed.) *Ferroelectric Materials, Elsevier Science Ceramics, New York*: Marcel Dekkar; 1991.

[31] H. Watanabe, T. Mihara, H. Yoshimori and C. A. Paz. De Arauja, *Jpn, J. Appl. Phys*, **34** (1995)5240 .

[32] Wei Wang, Jun Zhu, Xiang Yu Mao, Xiao-Bing Chen, *Materials Research Bulletin* **42** (2007)274-280.

[33] M. Miyayama, T. Nagamoto and O. Omoto, *Thin Solid Films*, **300** (1997) 299.

[34] H. T. Martirena and J. C. Burfoot, *J. Phys. C: Solid State Physics* **7** (1974) 3182.

[35] T. M. Shaw, S. Mckinstry, P. C. Mcintry, *Annul. Rev. Mater. Sci*. **30** (2000) 263.

[36] Dang –Hyok Yoon, *Journal of Ceramic Processing Research* **7** (2006) 343-354.

[37] W. Cochran, *Adv. Phys*. **9** (1960) 387-406.

[38] Hongli Guo, Wei Gao, Juhyun Yoo, *Materials Letters* **58** (2004) 1387-1391.

[39] Z. Wei, H. Xu, M. Noda, M. Okuyama, *J. Crystal Growth* **237** (2002) 443-447.

[40] Sheela Devi and A. K. Jha, *Physica B*, **404** (2009) 4290–4294.

[41] Y. Noguchi, I. Miwa, Y. Goshima, M. Miyayama *Jpn. J. Appl. Phys*. **39** (2000) 1259.

[42] W. L. Warren, D. Dimos, B. A. Tuttle, D. M. Smyth, *J. Am. Ceram. Soc*. **77** (1994) 2753-2757.

Chapter 4

Chapter 4

Effect of Tungsten (W) Substitution in Barium Titanate

4.1 Introduction

Defects in crystals significantly influence the physical properties of materials [1]. For the last several decades, defect engineering has been playing an important role in the field of ferroelectrics, and various kinds of defects have been introduced mainly into ABO_3- type ferroelectrics such as $BaTiO_3$, Pb (Ti, Zr)O_3 (PZT), etc. [2-3]. A practical advantage of pervoskite structure is that large number of different cations can be substituted on both A and B- sites without drastically changing the overall structure. Complete solid solutions are easily formed between many cations, often across the entire range of composition. Tungsten is known to have considerable effect on the structural, dielectric and ferroelectric properties in Strontium Bismuth Tanatalate, lead titanate, PZT, bismuth titanate ceramics [4-10]. The defect engineering through donor- modified barium titanate is thus an effective way to control various structural and electrical properties. With the objective to improve structural, dielectric and ferroelectric properties, the hexavalent W^{6+} was chosen as a donor cation for substitution onto the tetravalent Ti^{4+} sites. Moreover, hardly any report on W substitution in barium titanate was available in the literature. In this chapter, the effects of tungsten substitution in barium titanate (BT), on the microstructural, electrical and ferroelectric properties have been studied. The results including the improvement in dielectric and polarization properties in tungsten (W) - modified barium titanate have been discussed.

4.2 Results and Discussions

4.2.1 Structural Characterization

4.2.1.1 X-ray Diffraction

The observed XRD patterns of the studied samples having different tungsten content are shown in Fig. 4.1. It is observed that a pervoskite tetragonal structure is formed in all the samples. The peaks have been indexed with the help of a computer program – powder X [11] using the observed interplanar spacing d. The calculated lattice parameters were used to find the unit cell volume and tetragonal strain (c/a) of the specimens.

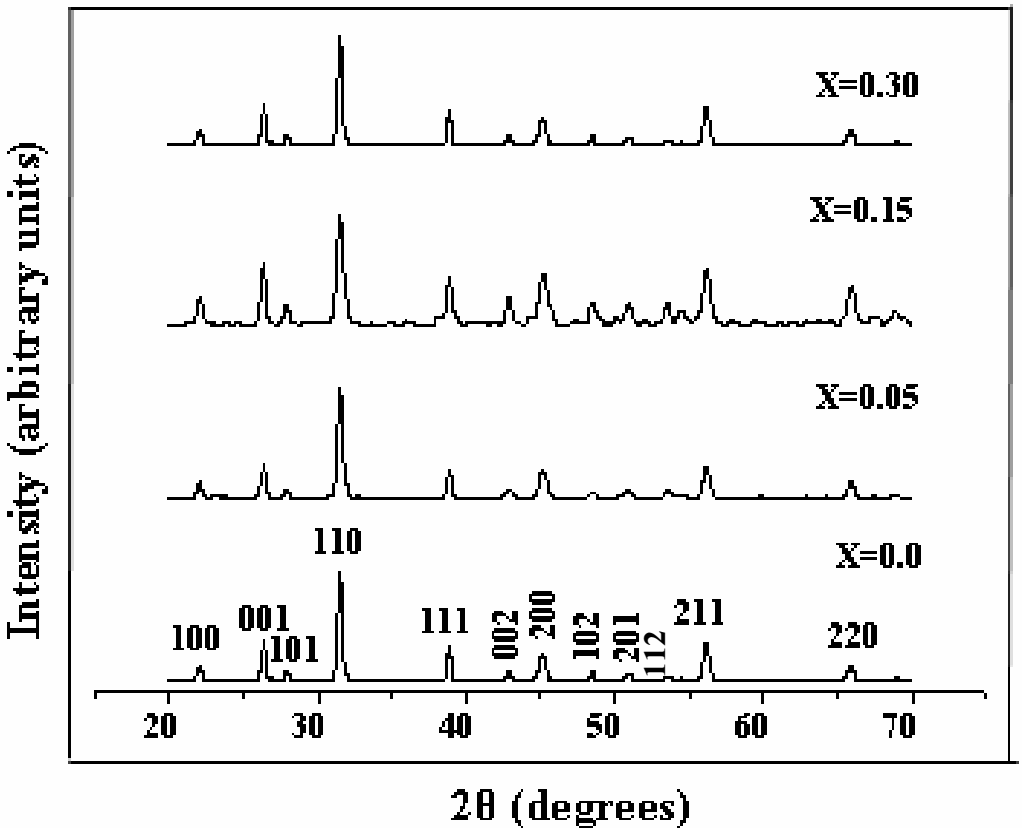

Fig. 4.1 XRD patterns of $(BaTi_{1-x}W_x)\ O_3$; x = 0.0-0.3

Lattice Parameters

The values of lattice parameters a and c as a function of x in $Ba(Ti_{1-x}W_x)O_3$ samples are listed in Table 4.1. On the basis of ionic radii of atoms and co-ordination number (Table 4.1), it is expected that tungsten should occupy titanium sites. Also, due to the smaller ionic radius of W^{6+} (0.60A˚) than that of Ti^{4+} (0.68A˚), a decrease in lattice parameters is expected. Lattice parameters (Table 4.1) are indeed observed to decrease with increasing tungsten content, confirming the occupation of W^{6+} ions onto the Ti^{4+} sites. A decrease in unit cell volume is observed in the samples. It is observed that there is a marginal decrease in tetragonal strain on the substitution of tungsten.

Table 4.1 Lattice parameters, ionic radii, tetragonal strain and unit cell volume of the studied samples

Composition	**a (A^0)**	**c (A^0)**	**c/a**	**Volume $(A^0)^3$**	**Ionic Radii**	**CN**
x = 0.0	3.999	4.038	1.009	64.575		
x = 0.05	3.996	4.025	1.007	64.271	Ti^{4+}= 0.68	6
x = 0.15	3.994	4.019	1.006	64.111	W^{6+}= 0.60	6
x = 0.30	3.989	4.010	1.005	63.807		

4.2.1.2 SEM Analysis

Fig. 4.2 shows the SEM micrographs of the studied samples. It is observed that the grains size is homogeneously and uniformly distributed. In general, composition and sintering temperature influences the microstructural features such as grain growth and densification which in turn control other properties of the materials [12-14]. The average grain size, determined by linear intercept method, increases on tungsten substitution; the grain size increases upto ~ 3 μm in the sample with x = 0.3. As seen in Fig. 4.2, tungsten substitution promotes grain growth and bigger grains are formed.

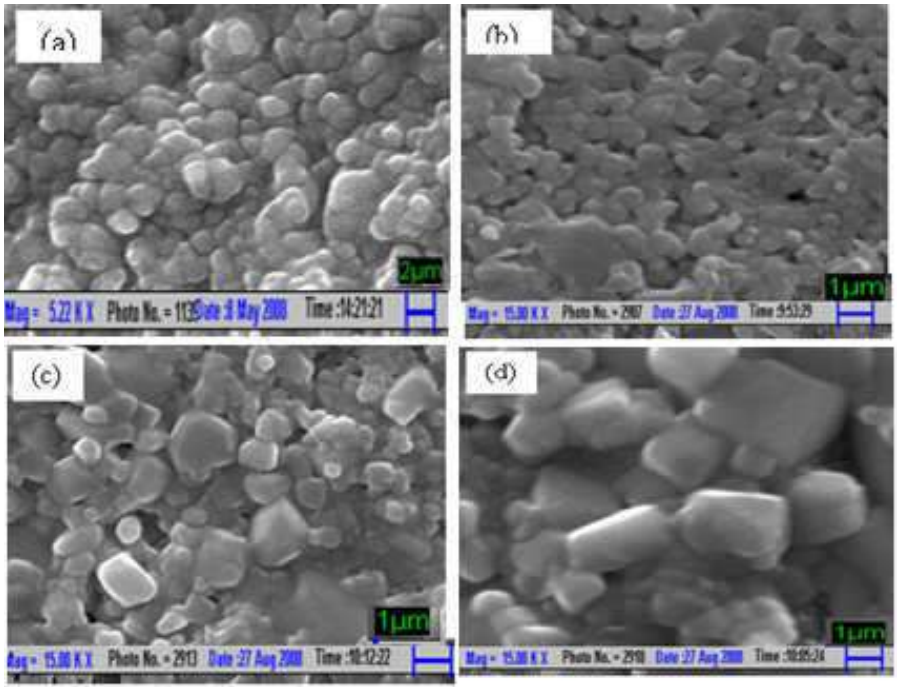

Fig. 4.2 SEM micrographs of the $Ba(Ti_{1-x}W_x)O_3$; x = 0.0-0.3

4.2.2 Electrical Characterization

4.2.2.1 Dielectric Studies

It is well known that the dielectric constant and dielectric loss of the ferroelectric materials in most cases depend upon the composition, grain size, secondary phases, etc. [15]. In this section, the influence of tungsten substitution in barium titanate on dielectric properties is presented.

Variation of ε' with Temperature: Curie Temperature

All ferroelectric materials are characterized by a transition temperature known as Curie temperature (T_c) at which the dielectric constant is maximum. At temperatures $T > T_c$, the crystal does not exhibit ferroelectricity while for $T < T_c$ it is ferroelectric [16].

Fig. 4.3 shows the temperature dependence of dielectric constant (ε') at selected frequencies of 100 Hz, 1 kHz, 10 kHz, 100 kHz. In tungsten free sample,

there is a sharp transition in the dielectric constant at Curie temperature T_c, where dielectric constant is maximum. Diffuse kind of ferro-para phase transition is observed in W-substituted samples.

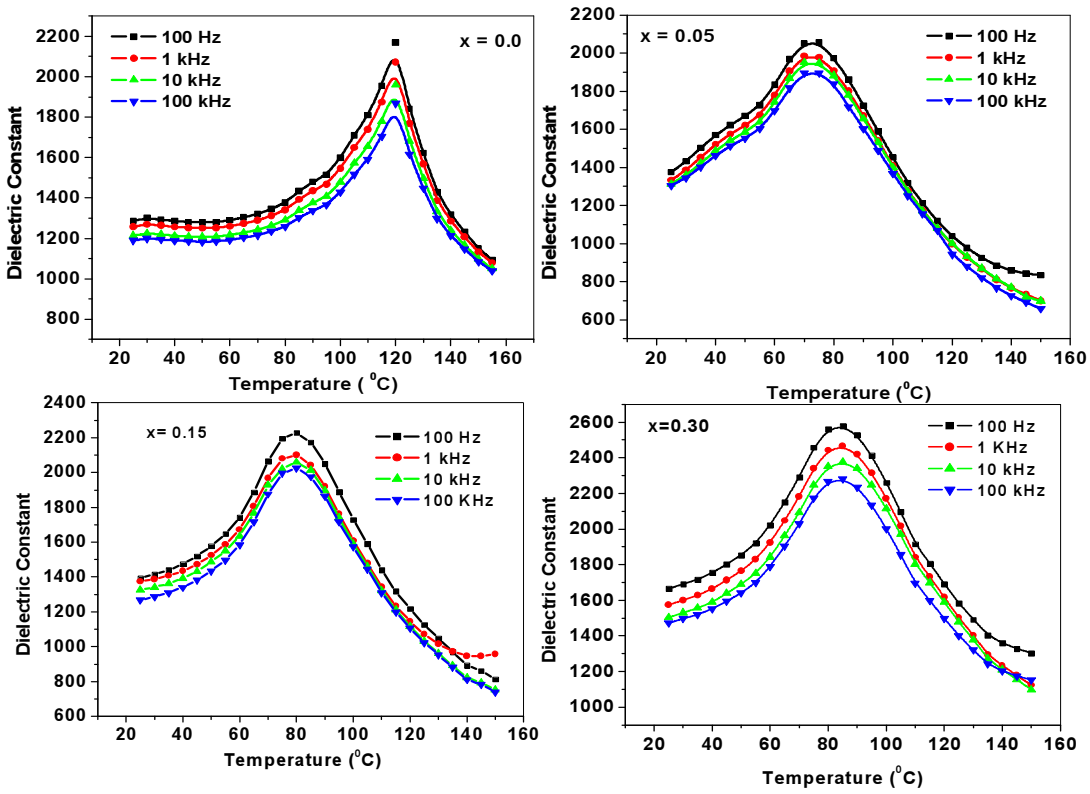

Fig. 4.3 Variation of dielectric constant with temperature at 100 Hz, 1 kHz, 10 kHz and 100 kHz in $Ba(Ti_{1-x}W_x)O_3$; x = 0.0-0.3

In the tungsten substituted samples the phase transitions getting broader with increasing tungsten content. Further, it is observed that the Curie temperature decreases from 120 °C to 75 °C (x = 0.05) on tungsten substitution. However, as tungsten content is increased to x = 0.30, the Curie temperature again increases to 85 °C, as seen in Fig. 4.4. The observed reduction in T_c and its subsequent increase can be understood as follows. It is known that when a higher valent ion replaces titanium, this leads to a decrease in the bond energy between tungsten and oxygen atoms [17].

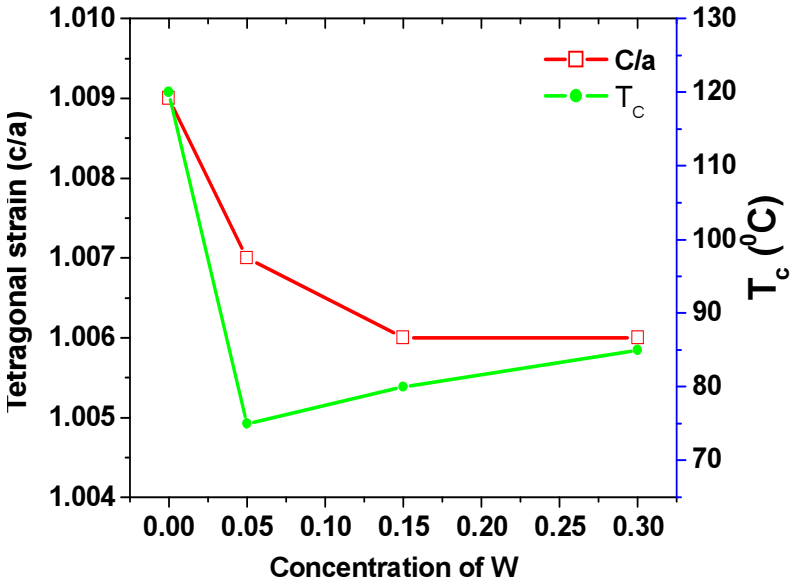

Fig. 4.4 Variation of tetragonal strain and Curie temperature as a function of W content

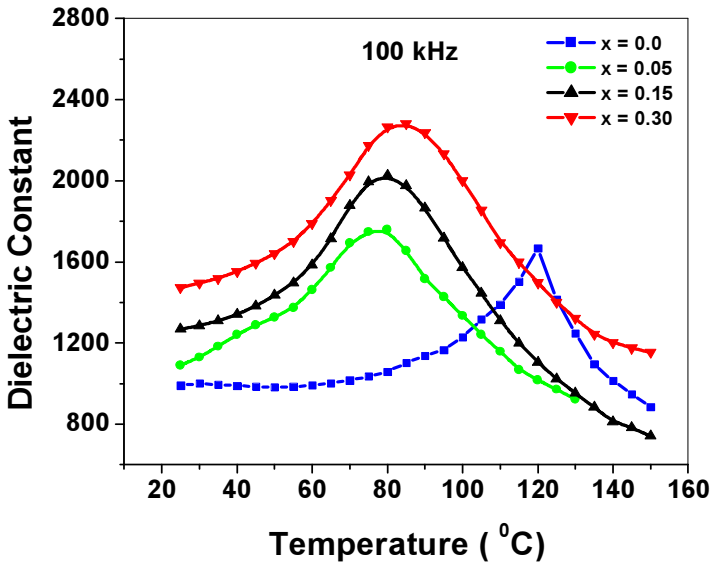

Fig. 4.5 Variation of dielectric constant vs. temperature at different concentration

This decrease in the bond energy leads to lesser distortion of the octahedron resulting in a decreased c/a ratio which is responsible for the reduction in Curie temperature [12]. However, for higher concentration of tungsten, a shift in T_C to higher temperature and the corresponding increase in peak dielectric constant of

tungsten substituted samples are also observed. In perovskite ferroelectric materials, substitution at B-site (located inside an oxygen octahedron) and the subsequent observed increase in dielectric constant and Curie temperature owing to higher polarization can be well explained by the enlarged "rattling space" available to the smaller B- site ions [18, 19]. Further, it is known [20] that the substitution of tungsten introduces cation vacancies at B-site, which possibly lead to an enhancement of ferroelectric structural distortion and an eventual increase in T_c. Another possible reason for the increase in dielectric constant is that these cation vacancies make the movement of the domains easier resulting in an increased dielectric permittivity [21, 22]. This can also be understood in terms of larger grains in the sample containing higher concentration of tungsten as observed in the SEM micrographs (Fig.4.2). It is known that the domain walls are comparatively free in the larger grains resulting in higher polarization. It is reasonable to believe that the observed variations in dielectric constant and T_c are due to the cumulative effect of all the above mentioned causes.

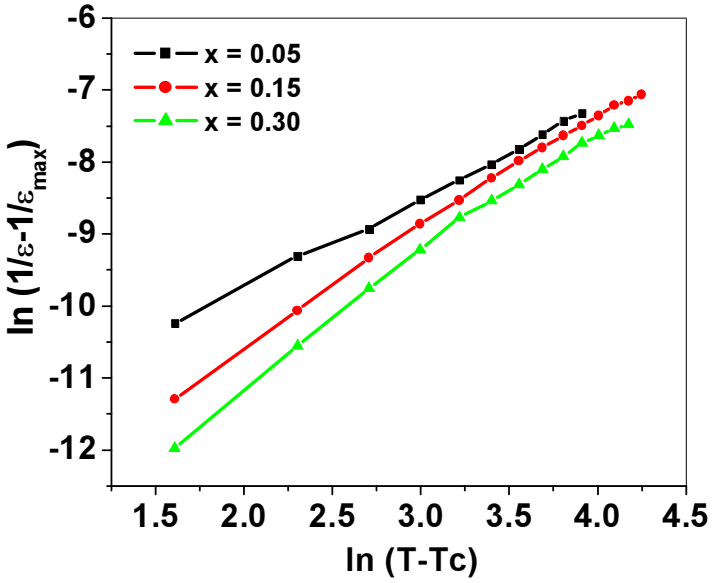

Fig. 4.6 Variation of ln ($1/\varepsilon - 1/\varepsilon_{max}$) with ln (T- Tc) at different tungsten concentration

The quantitative evaluation of the diffusivity or disorderness in an specimen can be made using the expression [23]:

$$\ln (1/\varepsilon - 1/\varepsilon_{max}) = \gamma \ln (T - T_c) + \text{constant} \quad (4.1)$$

where γ is a measure of diffusivity or disorderness of the ferroelectric to paraelectric phase transition and ε_{max} is the maximum dielectric constant at the Curie temperature (T_c).

Table 4.2 Dielectric constant (ε'), Curie temperature (T_c) and diffusivity (γ) of $Ba(Ti_{1-x}W_x)O_3$; x = 0.0-0.3

Composition	**Dielectric constant (ε')**	**T_C (^0C)**	**Diffusivity (γ)**
x = 0.0	1667.48	120	
x = 0.05	1759.17	75	1.26
x = 0.15	2025.83	80	1.59
x = 0.30	2281.37	85	1.74

The variation of $\ln (1/\varepsilon - 1/\varepsilon_{max})$ versus $\ln (T - T_c)$ (at 100 kHz) is shown in Fig. 4.6 and the calculated value of γ is given in Table 4.2. It is found that γ lies between 1 (normal Curie – Weiss behaviour) and 2 (for completely disordered system) confirming the diffuse type phase transitions in the specimens, as indeed observed [24]. The observed value of γ increases with increase in the tungsten content of the sample. This observation is in confirmity with the observed phase transitions in Fig. 4.5.

Variation of Dielectric Loss (tan δ) with Temperature

Fig. 4.7 depicts the dielectric loss (tan δ) as a function of temperature at various frequencies ranging from 100 Hz to 100 kHz for the studied samples. It is observed

that the loss initially remains largely independent of temperature up to nearly 90 ^{0}C and thereafter it increases with the increase in temperature. Further, it is observed that the loss increases more rapidly in the tungsten containing samples than that in the tungsten free sample.

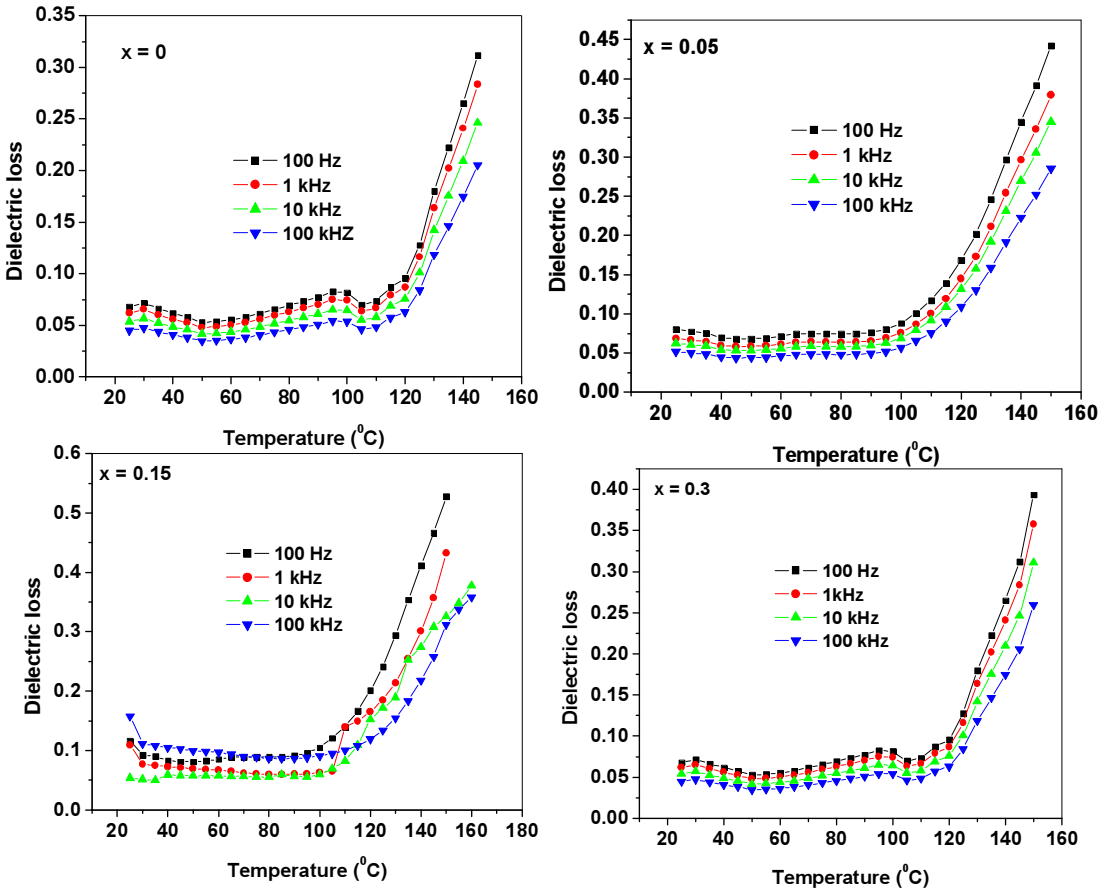

Fig. 4.7 Variation of dielectric loss with temperature at different frequencies

The observed variation of dielectric loss can be understood as follows. As discussed earlier, the substitution of W^{6+} for Ti^{4+} results in the formation of cation vacancies, leading to the soft characteristics in the material [20]. In the soft materials, high loss takes place due to the domain boundary vibrations or excitations that are readily stimulated even under the weak a.c. drive conditions [25].

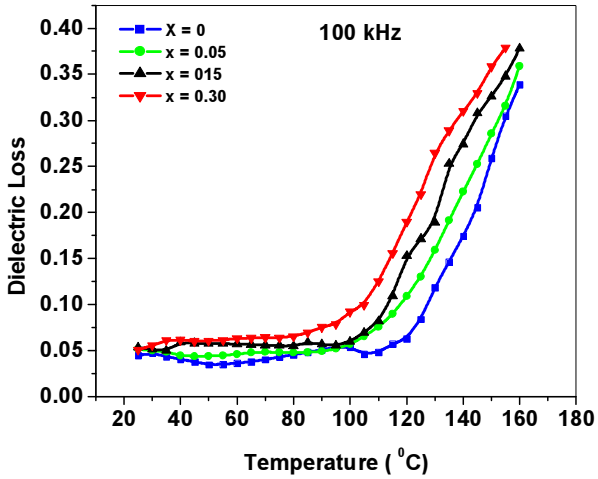

Fig. 4.8 Variation of dielectric loss (tan δ) with temperature.

Variation of Dielectric Constant (ε′) and Dielectric Loss (tan δ) with Frequency

Fig. 4.9 (a) and (b) shows the variation of dielectric constant (ε') and dielectric loss (tan δ) as a function of frequency at room temperature. In all the compositions, the dielectric constant and dielectric loss decreases upto about 1 kHz and remains nearly constant beyond this frequency. The dielectric constant of a material has polarization contributions from electronic, ionic, dipolar and space charge [26]. Response frequencies for ionic and electronic polarizations are ~ 10^{13} and 10^{15} Hz, respectively; and at frequencies beyond 1 kHz, contribution from space charge polarization is not expected [26]. Thus, the higher values of dielectric constant at lower frequencies can be attributed to the presence of defects such as oxygen vacancies. These vacancies act as space charge which plays an important role in the polarization at lower frequencies [27, 28]. Moreover, at lower frequencies, the dipoles can follow the oscillating electric field resulting in higher dielectric constant while at higher frequencies the dipoles are unable to follow the rapidly changing field leading to the reduction in the values of dielectric constant. The same reasons also hold for the variation of dielectric loss as the source of dielectric loss in insulating ceramics is space charge polarization and /or domain wall relaxation [29].

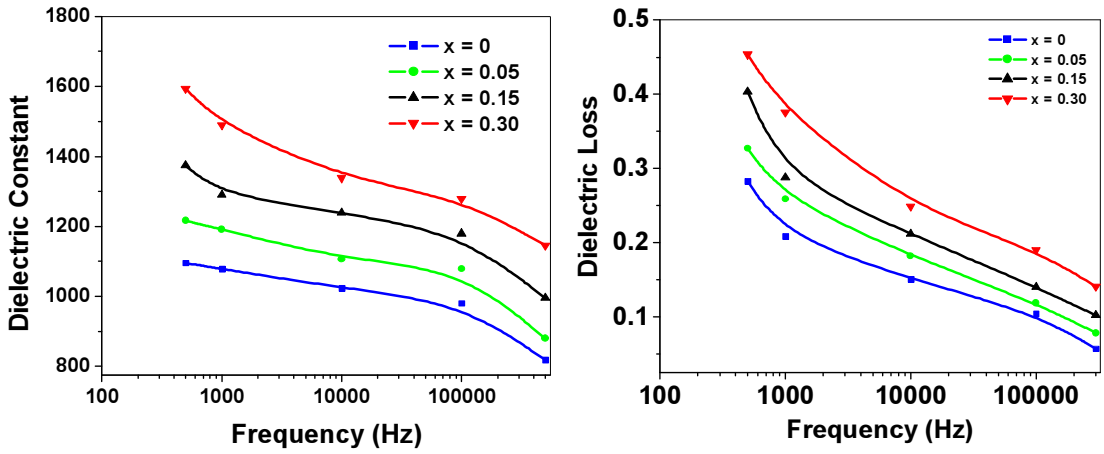

(a) (b)

Fig. 4.9 Variation of (a) dielectric constant (ε') and (b) dielectric loss (tan δ) with frequency

4.2.2.2 Conductivity Studies

DC Conductivity

Fig. 4.10 shows the variation of dc resistivity with temperature for the studied specimens. The curve shows PTCR behavior and there is an increase in resistivity with temperature. It is observed that resistivity of tungsten containing samples is higher than that of tungsten free sample.

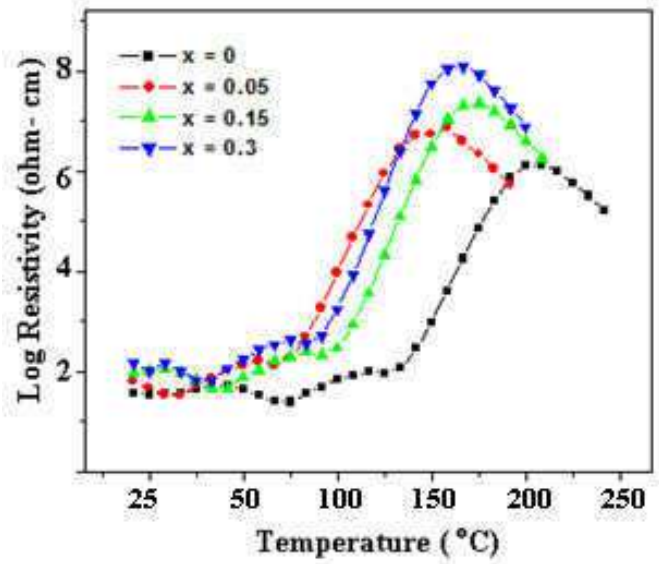

Fig. 4.10 Variation of dc resistivity with temperature

4.2.2.3 Impedance Analysis

Fig. 4.11 shows the impedance (Z'-Z") plots at different temperatures for Ba $(Ti_{1-x}W_x)$ O_3; x = 0.0 - 0.3 samples. The impedance spectra are characterized by the appearance of semicircular arcs, with some degree of decentralization (i.e., having their centers below the real axis). This decentralization or Non- Debye type relaxation obeys the Cole- Cole formalism [30], where the depressed semicircle represents typically relaxation phenomena with a spread of relaxation time.

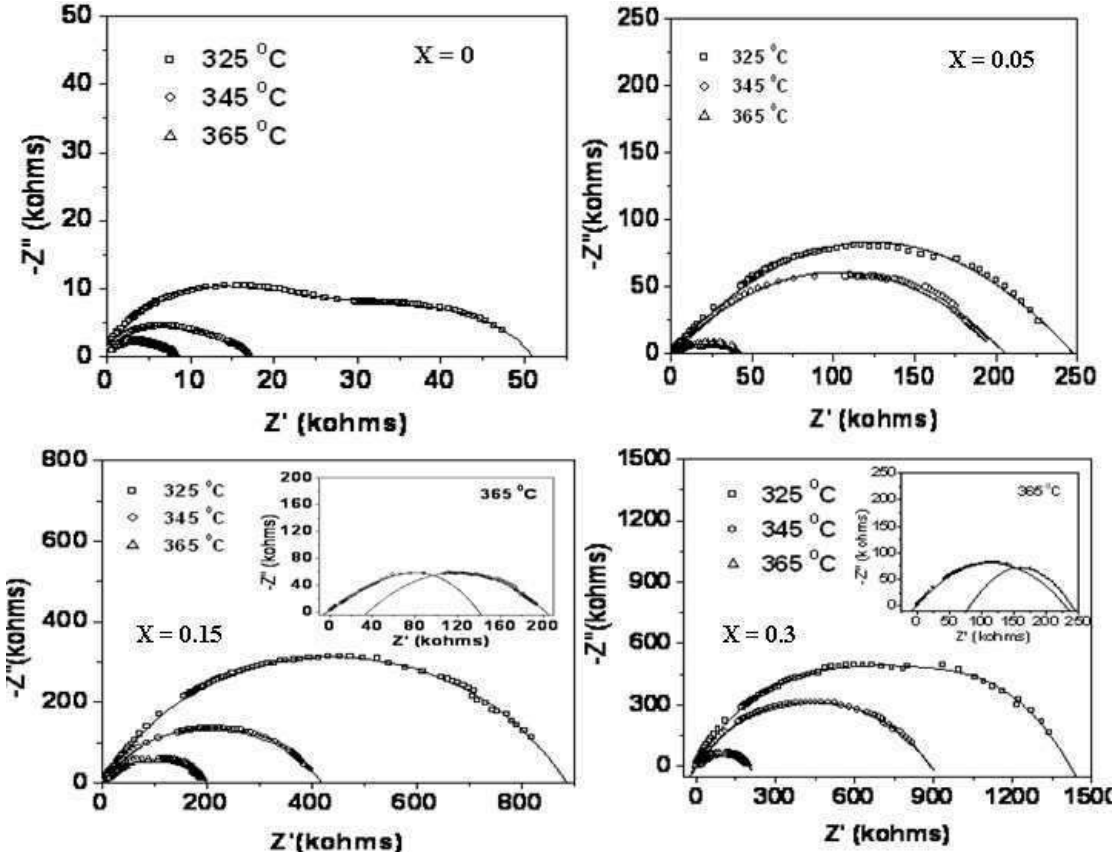

Fig. 4.11 Complex impedance spectrum (Cole-Cole or Nyquist plots) of $Ba(Ti_{1-x}W_x)O_3$ x = 0.0-0.3 at different temperatures

The Z'-Z" plots of the W substituted samples for small tungsten content are dominated by a single semicircle which represents the impedance contribution of the grains. However, at higher temperature (365 ^{0}C) and higher concentration of tungsten,

the contribution from grain boundaries is also significant (Table 4.3). This is indicated by the presence of two semicircles, exhibiting both grain (bulk property) and grain boundary effects. The high frequency semicircle corresponds to grain contribution, and the low frequency semicircle corresponds to the grain boundary effect (magnified view given in the inset) [31]. From these values of R_b (bulk resistance), σ_{bulk} (bulk conductivity) has been obtained by using Eq. (2.27) and its variation with temperature is shown in Fig. 4.13 for all the samples. The respective capacitance (C_b and C_{gb}) due to the grain and grain boundary effect can be calculated using the Eq. (2.26). The values of R_g, R_{gb}, C_b and C_{gb} obtained from cole-cole plots at different temperatures for various tungsten concentration samples are listed in Table 4.3.

Table 4.3 Grain resistance, grain boundary resistance, activation energy from relaxation time and bulk conductivity and capacitance of the studied compositions

Composition	**Temperature (^{0}C)**	**R_g (kΩ)**	**R_{gb} (kΩ)**	**E_a (eV) Relaxation time**	**E_a (eV)**	**C_b (nF)**	**C_{gb} (nF)**
x = 0.0	325	51	-	1.30	1.36	0.70	-
	345	18				0.25	
	365	8.5				0.11	
x = 0.05	325	250	-	1.25	1.39	0.56	-
	345	210				0.43	
	365	45				0.26	
x = 0.15	325	885	-	1.53	1.51	0.74	-
	345	420				0.68	-
	365	140	200			0.12	0.83
x = 0.30	325	1450	-	1.48	1.47	0.88	-
	345	275				0.41	-
	365	200	315			0.27	1.02

Fig. 4.12 shows the temperature variation of τ_b for all the studied samples. The relaxation time due to bulk effect (τ_b) has been calculated using Eq. (2.26). It is observed that the value of τ_b decreases with increase in temperature for all the samples and its temperature dependence follows the Arrhenius relation:

$$\tau_b = \tau_o \left(\frac{-E_a}{k_B T} \right) \tag{4.2}$$

where τ_o is the pre- exponential factor, k_B is Boltzmann constant and E_a is activation energy. The values of activation energy (E_a) calculated using Eq. (4.2) are summarized in Table 4.3.

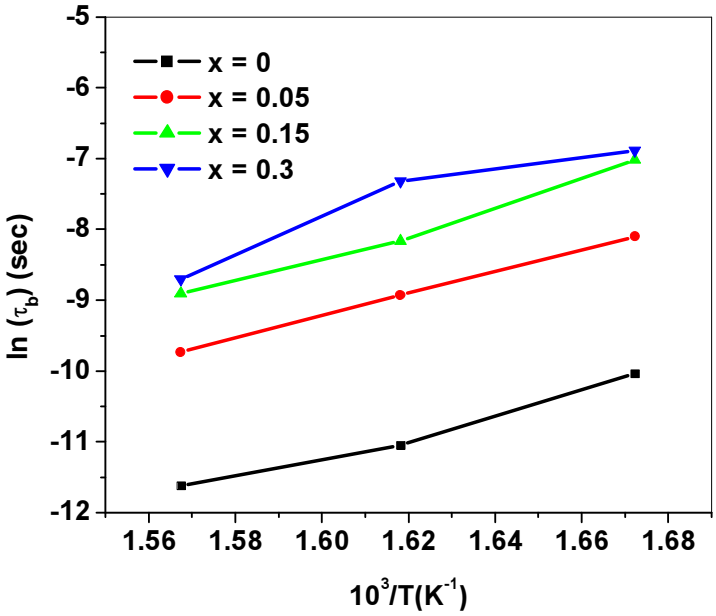

Fig. 4.12 Variation of relaxation time with temperature

Fig. 4.13 shows the variation of σ with 10^3/ T (K^{-1}) for all the samples. The dc (bulk) conductivity, σ, of the samples have been evaluated from the impedance spectrum using the relation

$$\sigma = \frac{t}{R_b A} \tag{4.3}$$

where R_b is the bulk resistance, K_B is Boltzmann constant, t is the thickness and A is the cross-sectional area of the sample. The observed variation of ln σ_{dc} vs. 10^3/ T is a straight line and follows the Arrhenius relationship

$$\sigma = \sigma_0 \exp\left(\frac{-E_a}{k_B T}\right) \tag{4.4}$$

where, σ_0 is the pre- exponential factor, k_B is Boltzmann constant, E_a is the activation energy of the mobile charge carriers and T is the absolute temperature.

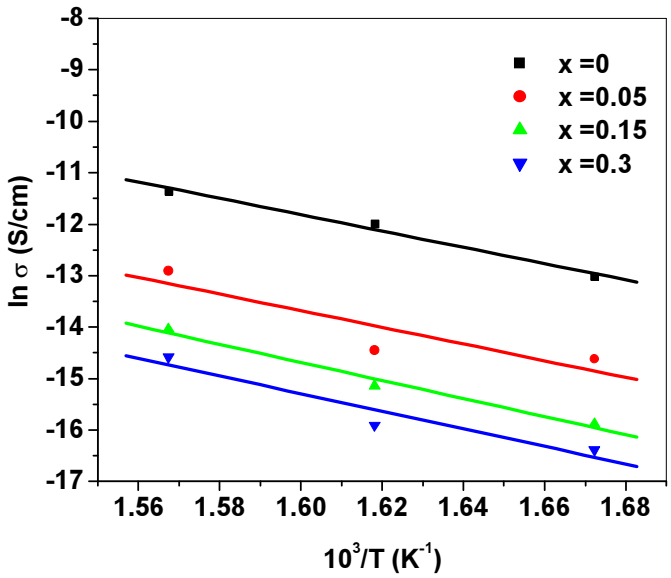

Fig. 4.13 Variation of bulk conductivity with temperature

The values of activation energy (E_a) as calculated from the of ln σ with 10^3/ T (K^{-1}) curve are shown in Table 4.3. The values of activation energy calculated from conductivity and relaxation time is nearly the same. It is also observed that with the increase in tungsten concentration, the bulk resistance increases. The oxygen vacancies are considered to be the most mobile ionic charge carriers in the perovskite oxides [32]. In the W- containing samples the substitution of W^{6+} onto

Ti^{4+} sites is accompanied by the formation of cation vacancies and subsequent elimination of oxygen vacancies. It is the decrease in the concentration of the oxygen vacancies that a decrease in conductivity with increasing concentration of tungsten is observed.

4.2.2.4 Ferroelectric Studies

P-E hysteresis loops of $Ba(Ti_{1-x}W_x)O_3$ samples recorded at 50 Hz and room temperature using a Sawyer- Tower circuit are shown in Fig. 4.14. The observed variation of remanent polarization and coercive field is shown in Fig 4.15. It is seen that P_r increases with increase in tungsten content of the sample. The maximum $P_r \sim 2.67\ \mu C/cm^2$ is observed in the sample with x = 0.30.

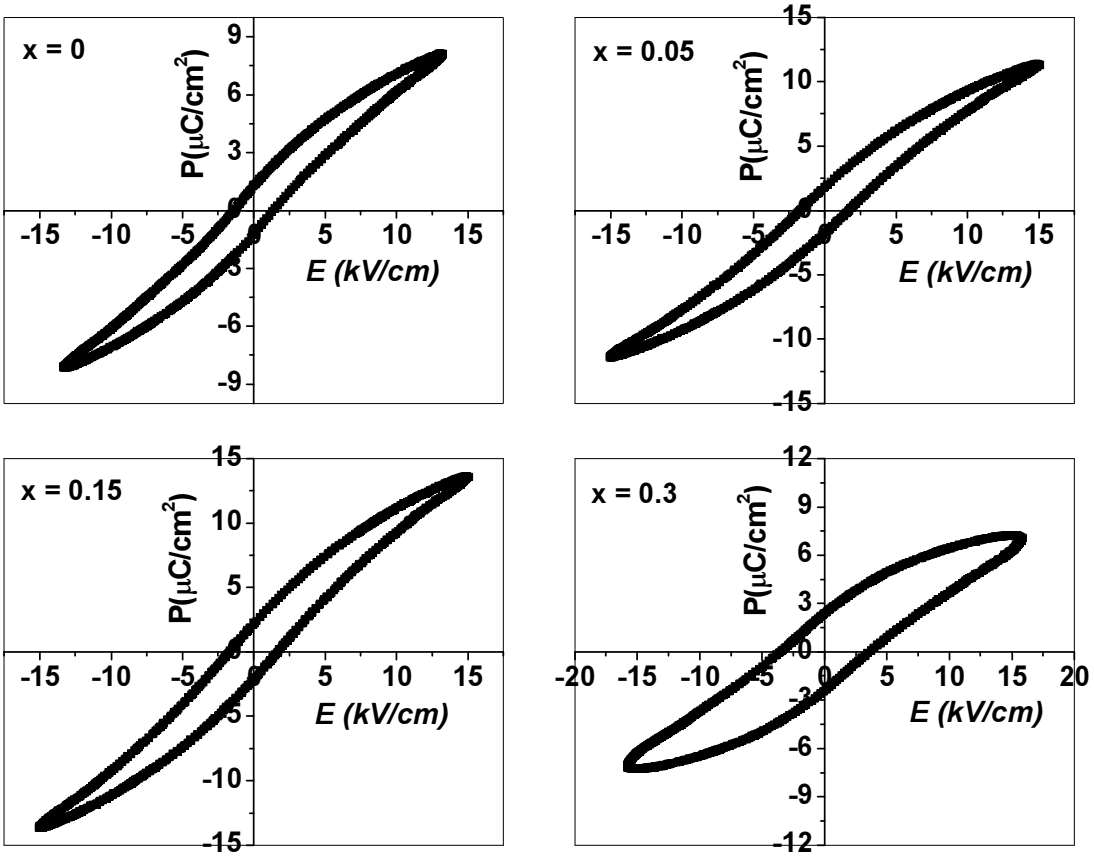

Fig. 4.14 P-E hysteresis loops of $Ba(Ti_{1-x}W_x)O_3$; x = 0.0-0.3 samples at room temperature

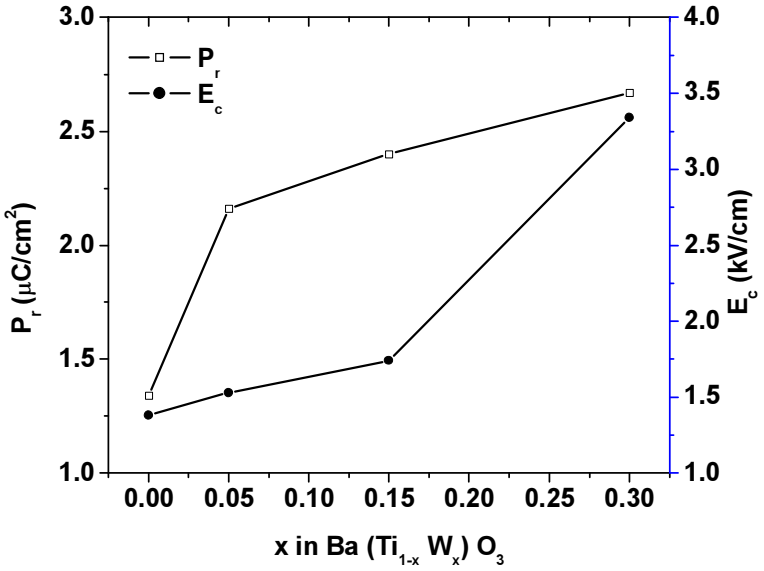

Fig. 4.15 Variation of P_r and E_c with tungsten content in $Ba(Ti_{1-x}W_x)O_3$.

It is known that ferroelectric properties are affected by compositional modification, microstructural variation and lattice defects like oxygen vacancies [33-35]. In *hard* ferroelectrics, with lower-valent substituents, the generated vacancies are likely to assemble in the vicinity of domain walls [36-37]. This produces hindrance in the polarization switching process and consequently the switching becomes difficult, leading to an increase in E_c and decrease in P_r [37]. On the other hand, in *soft* ferroelectrics, with higher-valent substituents, the defects are cation vacancies whose generation in the structure generally increases P_r [34, 27, 38]. The observed increase in P_r can be understood in terms of the fact that it is known that in barium titanate oxygen vacancies are major structural defects [39-41]. There are many reports, which confirm, the defects such as oxygen vacancies ($V_o^{\cdot\cdot}$), act as space charge and cause strong domain pinning, leading to smaller P_r [34, 37]. However, in the studied samples, W^{6+} acts as a donor and cation vacancies are formed. The defect equation can be represented by Kroger -Wink notation [42]

$$WO_3 \leftrightarrow W^{\circ\circ}{}_{Ti} + 3O_0 + 2e^-$$

$$O_2 + V_o^{\cdot\cdot} + 2e \leftrightarrow Oo$$

where $W^{\circ\circ}_{Ti}$ is W ion with +2 effective charge at the core of the oxygen octahedron, $V_o^{\cdot\cdot}$ indicates vacant oxygen site with +2 effective charge and O_o is an oxygen atom on the oxygen site. In the W substituted samples, the cation vacancies are formed due to the substitution of W^{6+} at Ti^{4+} site. These generated cation vacancies suppresses the concentration of oxygen vacancies. A reduction in the number of oxygen vacancies reduces the pinning effect on the domain walls, leading to an enhanced remanent polarization. Also, the increased grain size (Fig. 4.2) is another factor causing the observed increased in P_r values. It is known that domain walls are relatively free in large grains as compared to smaller grains [12]. In the larger grains domain motion is easier which results in larger P_r values.

4.2.2.5 Piezoelectric Studies

Fig. 4.16 shows the variation of piezoelectric coefficient d_{33} with tungsten content in the studied samples. It is observed that the piezoelectric coefficient (d_{33}) increases from 92.45 pC/N in the sample with x = 0.0 to 112.8 pC/N in the sample with x = 0.15. It has been known that an increase in grain size and the formation of cation vacancies associated with substitution by donor doping ion improves the piezoelectric properties [43, 44].

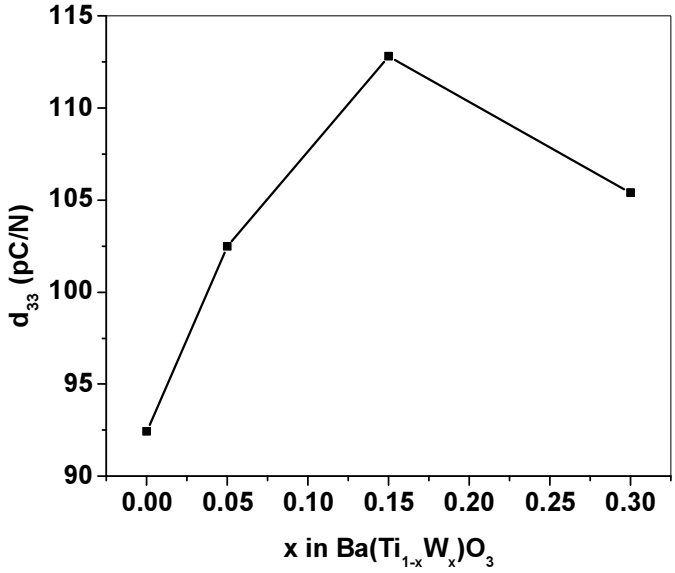

Fig. 4.16 Variation of d_{33} in $Ba(Ti_{1-x}W_x)O_3$ x = 0.0-0.3 samples

4.3 Conclusions

Based on the above observations and discussions the following conclusions can be drawn:

- X- Ray diffractograms of the samples confirm the formation of the materials with pervoskite single phase tetragonal structure.
- SEM micrographs reveal that the average grain size increases with increase in W concentration and the grain size increases upto ~ 3μm.
- Unit cell volume and tetragonal strain decrease with the increase in the tungsten content of the sample.
- Curie temperature decreases on tungsten substitution but it again increases on increasing the tungsten content.
- The peak dielectric constant is found to increase on tungsten substitution.
- The compounds show diffuse kind of ferro-para phase transitions with the diffusivity increasing with the increasing tungsten content.
- At higher temperature and W-content the grain boundary contribution to the overall impedance becomes significant.
- Tungsten substituted barium titanate show PTCR behaviour.
- Substitution of tungsten is found to be effective in eliminating oxygen vacancies which decreases the conductivity of the studied samples.
- Polarization- Electric field hysteresis loops confirm the ferroelectric nature of the synthesized specimen at room temperature and the remanent polarization increases with increases in tungsten content.
- The d_{33} value is observed to increase with increasing W content up to x = 0.15 and maximum value is observed to be 112.48 pC/N.

References

[1] Y. Noguchi, M. Miyayama, K. Oikawa, T. Kamiyama, M. Osada & M. Kakihana, *Jpn. J. Appl. Phys*., **41** (2002) 7062.

[2] D. Berlincourt, D. Curran & H. Jaffe, Physical Acoustics, ed. W. Cady (vol. 1, Academic Press, New York, 1964).

[3] G. H. Heartling & C.E. Land, *J. Amer. Ceram. Soc*., **54** (1971) 1.

[4] JIIN-JYH SHYU and CHIH- CHUNG LEE , *Ferroelectrics* **287** (2003) 21.

[5] Wei Wang, Jun Zhu, Xiang –Yu Mao, Xiao- Bing Chen, *Materials Research Bulletin* **42** (2007) 274-280.

[6] Ni Zhong, Xianlin Dong, Dazhi Sun, Hui Du, Hong Yang, *Material Science & Engineering B* **106** (2004) 263-268.

[7] M. Villegas, T. Jardiel, G. Farias, *Journal of European Ceramic Society* **24** (2004) 1025-1029.

[8] Lina Zhang, Suchuan Zhao, Hanfeng Yu, Liaoying Zheng, Guorong Li and Qingrui Yin, *Japn. J. of Applied Physics* **43** (2004) 7613-7617.

[9] Indrani Coondoo, A. K. Jha and S. K. Agarwal, *Ferroelectrics* **356** (2007) 31-39.

[10] Indrani Coondoo, A. K. Jha and S. K. Agarwal, *J. European ceramics* **16** (2006) 393-398.

[11] C. Dong, J. *Appl. Crystallogr*. **32** (1999) 838.

[12] Sheela Devi and A. K. Jha, *Physica B* **404** (2009) 4290-4294.

[13] T. Atsuki, N. Soyama, T. Yonezawa, K. Ogi, *Japan J. Appl. Phys*. **34** (1995) 5096.

[14] M. Noda, Y. Matsumuro, H. Sugiyama, M. Okuyama, *Japan J. Appl. Phys*. **38** (1999) 2275.

[15] R. R. Das, P. Bhattacharya, W. Perez and R.S. Katiyar, *Ceram. Inter*. **30** (2004) 1175.

[16] M. Deri, Ferroelectric Ceramics (Akademiai Kiado, Budapest) 1966.

[17] Cao Wanqiang, Junwen Xiong, Sun Juanpin, *Materials Chemistry and Physics*, **106** (2007) 2-3, 338-342.

[18] Indrani Coondoo, A. K. Jha, S. K. Agarwal, *Ceramics international*, **33** (2007) 41-47.

[19] K. Singh, D.K. Bopardikar and D.V. Atkare, *Ferroelectric*, **82** (1988) 55-67.

[20] Ni Zhong, Xian – Lin Dong, Da- Zhi Sun, Ping- hua Xiang, Hui Du, *Material Research Bulletin* **39** (2004) 175-184.

[21] Y. Wu, S. J. Limmer, T.P. Chou and C. Nguyen, *J. Material. Sci. Lett.* **21** (2002) 947-949.

[22] S. Takahashi and M. Takahashi, *Jpn. J. Appl. Phys*. **11** (1972) 31-35.

[23] S. M Pilgrim, A. E Sutherland, S. R Winzer, *J. Am. Cer. Soc*. **73** (1990) 3122-3125.

[24] J. Daniels, K. H Harlet, R. Wernicke, *Philips Res. Rep*. **36** (1976) 487-559.

[25] Ximei Zong, Zupei Yang, Hui Li, M ingbo Yuan, *Materials Research Bulletin,* **41** (2006) 1447-1454.

[26] R. C. Buchanan, *Ceramic Materials for Electronic: Processing, properties and Applications* (Marcel Dekker Inc., New York, 1986) 38.

[27] Y. Noguchi and M. Miyayama, *Appl. Phys. Lett*. **78** (2001) 1903.

[28] A. Chen, Y. Zhi and L.E. Cross, *Phys. Rev. B* **62** (2000) 228.

[29] I.S. Zheludev, *Physics of crystalline Dielectrics, Vol 1: Crystallography & Spontaneous polarization* (Plenum Press, New York (1971).

[30] M.A.L. Nobre, S. Lanfredi, *J. Physics and Chemistry Solids* **64** (2003) 2457.

[31] B. Behera, P. Nayak, R.N.P. Choudhary, *J. Alloys Comp*. **436** (2007) 226.

[32] D. M. Smyth, *Ferroelectrics*, **117** (1991) 117-124.

[33] H. Watanabe, T. Mihara, H. Yoshimori, C. A, Paz, De, Araujo. *Jpn. J. Appl. Phys*., **34** (1995) 5240-5244.

[34] Y. Noguchi, I. Miwa, Y. Goshima, M. Miyayama, *Jpn. J. Appl. Phys* (2000) **39** L11259-1262.

[35] Sheela Devi and A. K. Jha, *Asian Journal of Chemistry* **21** (2009) 10, S117-124.

[36] W. Wang, Zhu J. Mao X.Y. Chen *Mater. Res. Bull*. **42**(2007) 274-280.

[37] T. Friessnegg, S. Aggarwal, R. Ramesh, B. Nielsen, E.H. Poindexter, D. Keeble. *J. Appl. Phys. Lett.* **77** (2000) 127-129.

[38] B.H. Park, B.S. Kang, S.D. Bu, T.W. Noh, L. Lee, W. Joe. *Nature* (London) **401** (1999) 682-684.

[39] Om Prakash, Devendra Kumar, R.K. Dwivedi, K. Srivastava, Prakash Singh, Sindhu Singh. *J. Mater Sci* **42** (2007), 5490-5496.

[40] J.Q. Qi, W.P. Chen, Y.J. Wu, L.T. Li, *J. Am. Ceram. Soc.* **81** (1998) 2 437-438.

[41] Bin Cui, Yu Pengfei, Jing, Tian, Guo Huilin, Jing Chang Jing, *Material Science and Engineering A*. **454-455** (2007) 667-672.

[42] F. A. Kroger, H. J. Wink *Solid State Physics*, Academic Press, New York; 1956.

[43] C. Fujioka, R. Aoyagi, H. Takeda, S. Okamura, T. Shiosaki. *J. Eur. Ceram Soc.* **25** (2005) 2723-2729.

[44] H. T. Martirena, J. C. Burfoot. *J. Phys. C: Solid State Phys*, **7** (1974) 3182-3185.

Chapter 5

Chapter 5

Effect of Tungsten Substitution in Barium Strontium Titanate

5.1 Introduction

Barium strontium titanate $Ba_{1-x}Sr_xTiO_3$ (BST) has attracted a great deal of attention for its use in dynamic random access memories (DRAM) due to its relatively high dielectric constant, low leakage current, high dielectric breakdown strength and low dissipation factor [1,2]. BST solid solution belongs to A- site substituted pervoskite barium titanate. The Curie temperature of $Ba_{1-x}Sr_xTiO_3$ single crystals decrease linearly with increasing strontium concentration [3]. The transition temperature of BST from ferroelectric to paraelectric state or the Curie temperature (T_c) varies as a function of Ba/Sr ratio [4]. By modifying the composition, the Curie temperature can be tuned for the particular application and optimal values of permittivity can be obtained [5]. The suitable of Ba/Sr ratio makes material available to be used in the non-polar phase at different ambient temperatures. Many rare earths and transition–metals elements such as Mn, Y, Nb, La, Fe and Zn have been used as substituent [6-11]. However, hardly any report was available in the literature on the W- substitution in barium strontium titanate (BST) ferroelectric material. In this chapter, the effect of tungsten substitution in barium strontium titanate (BST) on the microstructural, electrical and ferroelectric properties is discussed.

5.2 Results and Discussions

5.2.1 Structural Characterization

5.2.1.1 X-ray diffraction

Fig. 5.1 shows the XRD patterns of the studied samples of composition $Ba_{0.8}Sr_{0.2}(Ti_{1-x}W_x)O_3$ sintered at 1250 ^{0}C for 2 hours. It is observed that single phase pervoskite tetragonal structure is formed in the specimen up to x = 0.05.

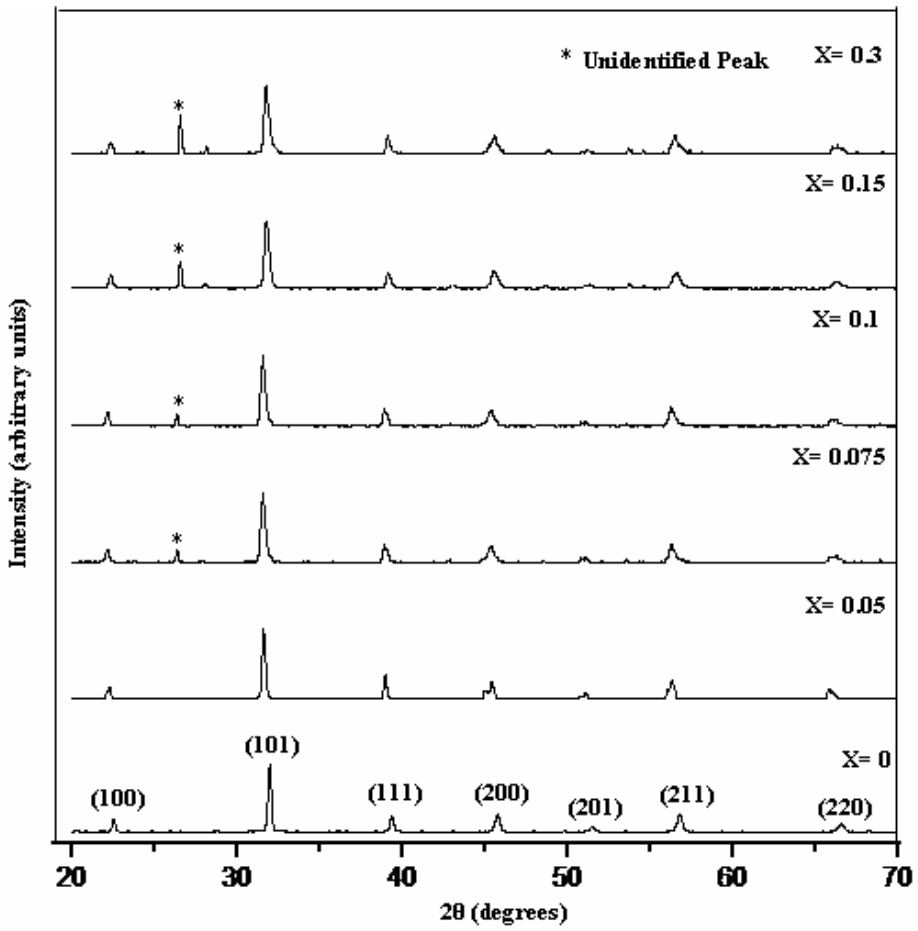

Fig. 5.1 XRD patterns for $Ba_{0.8}Sr_{0.2}(Ti_{1-x}W_x)O_3$ samples

However, as the concentration of W is increased, secondary peak is observed and intensity of this peak continuously increases with increasing W content in the samples.

Lattice Parameters

The lattice parameters of the samples have been calculated using the observed d-values from the diffratograms [12]. The peaks have been indexed using the observed interplanar spacing d and the lattice parameters so obtained were refined using the least square refinement method by a computer program Powder -X [13]. The obtained lattice parameters are listed in Table 5.1. According to the principles of crystal chemistry [14] and radius- matching rule, it is most likely that W ions occupy the B-sites (Ti) and serve as the donor – dopant.

Table 5.1 Lattice parameters, unit cell volume and tetragonal strain of $Ba_{0.8}Sr_{0.2}(Ti_{1-x}W_x)O_3$ samples

x (W conc.)	a (A°)	c (A°)	Unit cell volume $(A°)^3$	c/a
0	4.0115	4.0352	64.934	1.0059
0.05	4.0073	4.0242	64.622	1.0042
0.075	3.9871	4.0012	63.606	1.0035
0.1	3.9890	4.0016	63.673	1.0031
0.15	3.9912	4.0022	63.753	1.0027
0.3	3.9951	3.9973	63.800	1.0005

The decrease in the values of lattice parameters and tetragonal strain in the tungsten substituted BST is observed.

5.2.1.2 SEM Analysis

SEM micrographs of tungsten substituted samples are shown in Fig. 5.2. It is observed that grains are randomly distributed with porosity increasing at higher W concentration. At higher W concentration, it is observed that interdiffusion of grains takes place and the boundaries of the grains are not so sharp. The average grain size,

determined by the linear intercept method, is found to be approximately in the range of 0.5 to 1 μm.

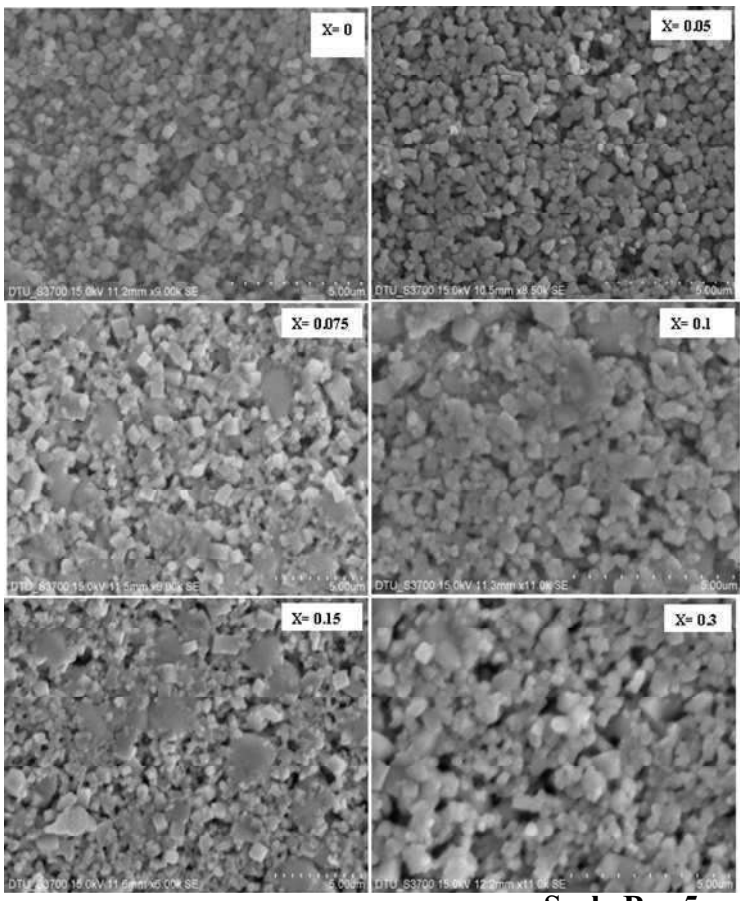

Fig. 5.2 SEM micrographs of $Ba_{0.8}Sr_{0.2}(Ti_{1-x}W_x)O_3$ samples

5.2.2 Electrical Characterization

5.2.2.1 Dielectric Studies

It is well known that the dielectric constant (ε′) and dielectric loss (tan δ) of the ferroelectric materials depend upon the composition, grain size, secondary phases, etc. [15]. In this section, the effects of tungsten substitution in barium strontium titanate compound on dielectric properties are presented.

Variation of Dielectric Constant (ε′) with Temperature: Curie Temperature

Fig. 5.3 shows the variation of dielectric constant of the studied samples as function of temperature measured at different frequencies ranging from 100 kHz to 700 kHz. It is observed that Curie temperature (T_c) remains the same at all the frequencies indicating non-relaxor behavior in the samples.

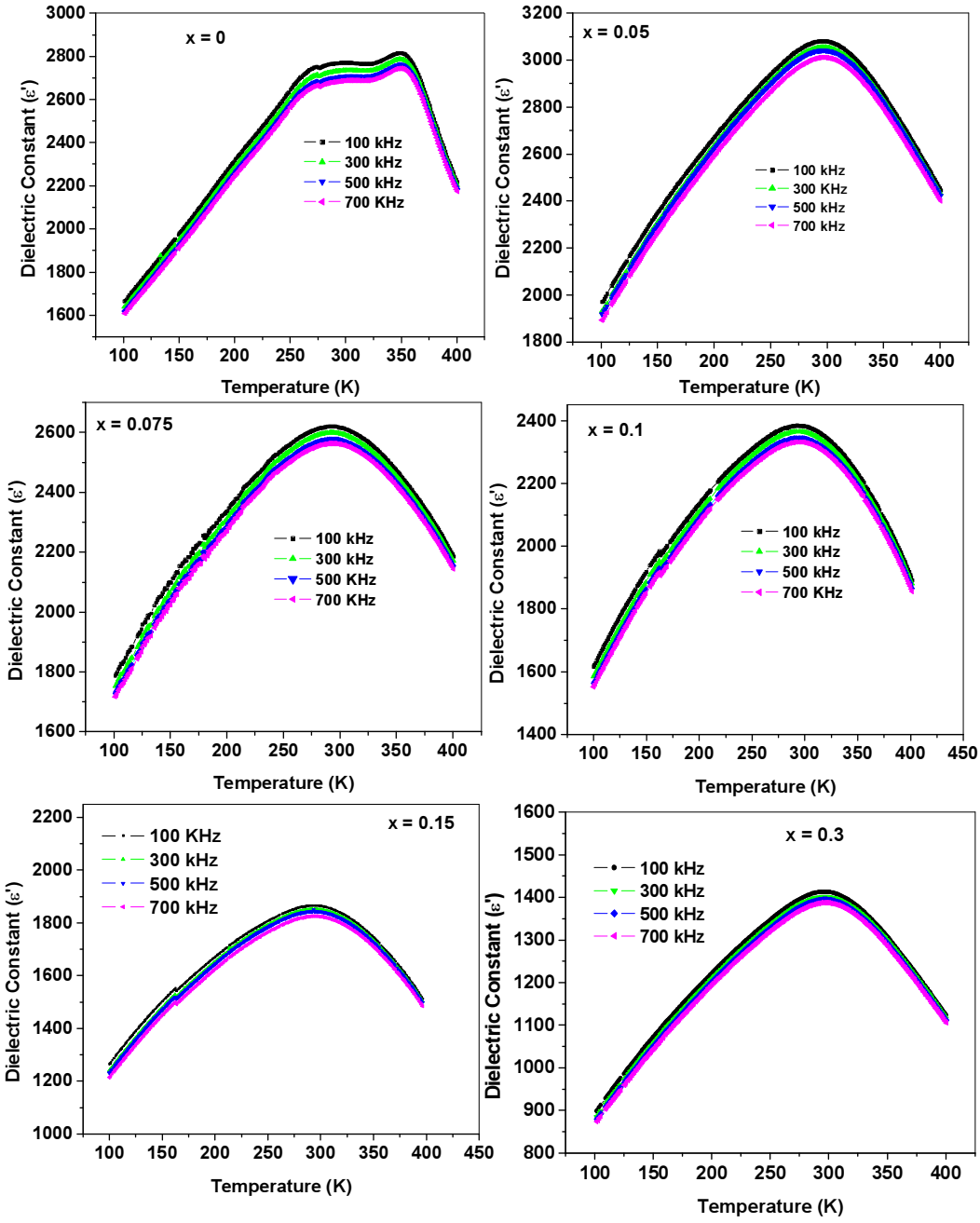

Fig. 5.3 Variation of dielectric constant with temperature at different frequencies

It is observed that the dielectric constant increases gradually with increasing temperature up to the transition temperature T_c and then decreases with a broadened peak near the transition. The broadened peaks, as observed in Fig. 5.3, indicates that transition in all the samples is of diffuse type [16]. The broad peaks imply that the ferroelectric-paraelectric phase transitions do not occur at a discrete temperature but over a temperature range [17]. The broadening or diffuseness of peak occurs mainly due to two the following causes. First, due to the substitution disordering in the arrangement of cations at one or more crystallographic sites in the lattice structure leading to heterogonous domains [18]. Second, is due to the defect induced relaxation at a high temperature [18, 19]. Fig. 5.4 shows the temperature dependence of dielectric constant for all the compounds at a frequency 100 kHz. It is observed that the Curie temperature decreases from 347 K (x = 0) to 295 K (x = 0.05) on W substitution. The reduction in Curie temperature can be explained as follows. Substitution by smaller W^{6+} ions in place of larger Ti^{4+} ions, leads to a decrease in the bond energy between tungsten and oxygen atoms [20].

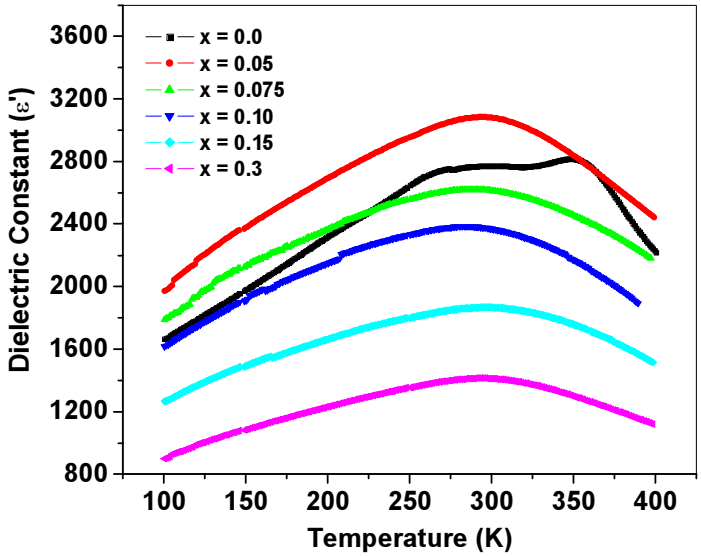

Fig. 5.4 Variation of dielectric constant with temperature at 100 kHz

This decrease in the bond energy leads to lesser distortion of the octahedron resulting in a decreased c/a ratio which is responsible for the reduction in Curie temperature. The observation can also be understood in terms of the observed tetragonal strain (c/a) variation [21]. Tetragonal strain is the internal strain in the lattice which affects the phase transition temperature [22]. Smaller value of strain indicates a lesser amount of thermal energy is required for the phase transition and therefore a decrease in T_c is expected as indeed observed. Similar observation has been made in W substituted lead complex pervoskite [23]. It is also observed that dielectric constant increases for small concentration of W while for higher x = 0.075-0.3, the dielectric constant decreases and curves becomes flatter i. e, the transition becomes broader. The broadening or diffuseness of the peak occurs mainly due to compositional fluctuation or substitution disordering [24] in the arrangement of cations at one or more crystallographic sites in the lattice structure.

Table 5.2 Crystallite size, dielectric constant and Curie temperature of the studied specimens

Composition	**Crystallite Size (nm)**	**Dielectric Constant**	**T_c (K)**
x = 0	32.36	2825.50	347
x = 0.05	32.90	3082.38	295
x = 0.075	29.77	2620.79	293
x = 0.1	29.76	2384.79	294
x = 0.15	30.77	1866.37	292
x = 0.3	32.89	1412.75	296

It is known that [25] the substitution of tungsten introduces cation vacancies at B-sites, these induced cation vacancies result in the increased dielectric constant [26]. Also, only a small amount of W^{6+} can occupy Ti^{4+} sites. As W content increases and exceeds the solid solubility limit of the compound, secondary phase is formed, as

revealed in XRD diffractogram. The formation of these secondary phases is responsible for the reduction of dielectric constant.

Variation of Dielectric Loss with Temperature: tan δ

Fig. 5.5 shows the variation of dielectric loss (tan δ) with temperature at different frequencies of 100 kHz, 300 kHz, 500 kHz and 700 kHz. It is observed that tungsten substitution in barium strontium titanate reduces dielectric loss significantly.

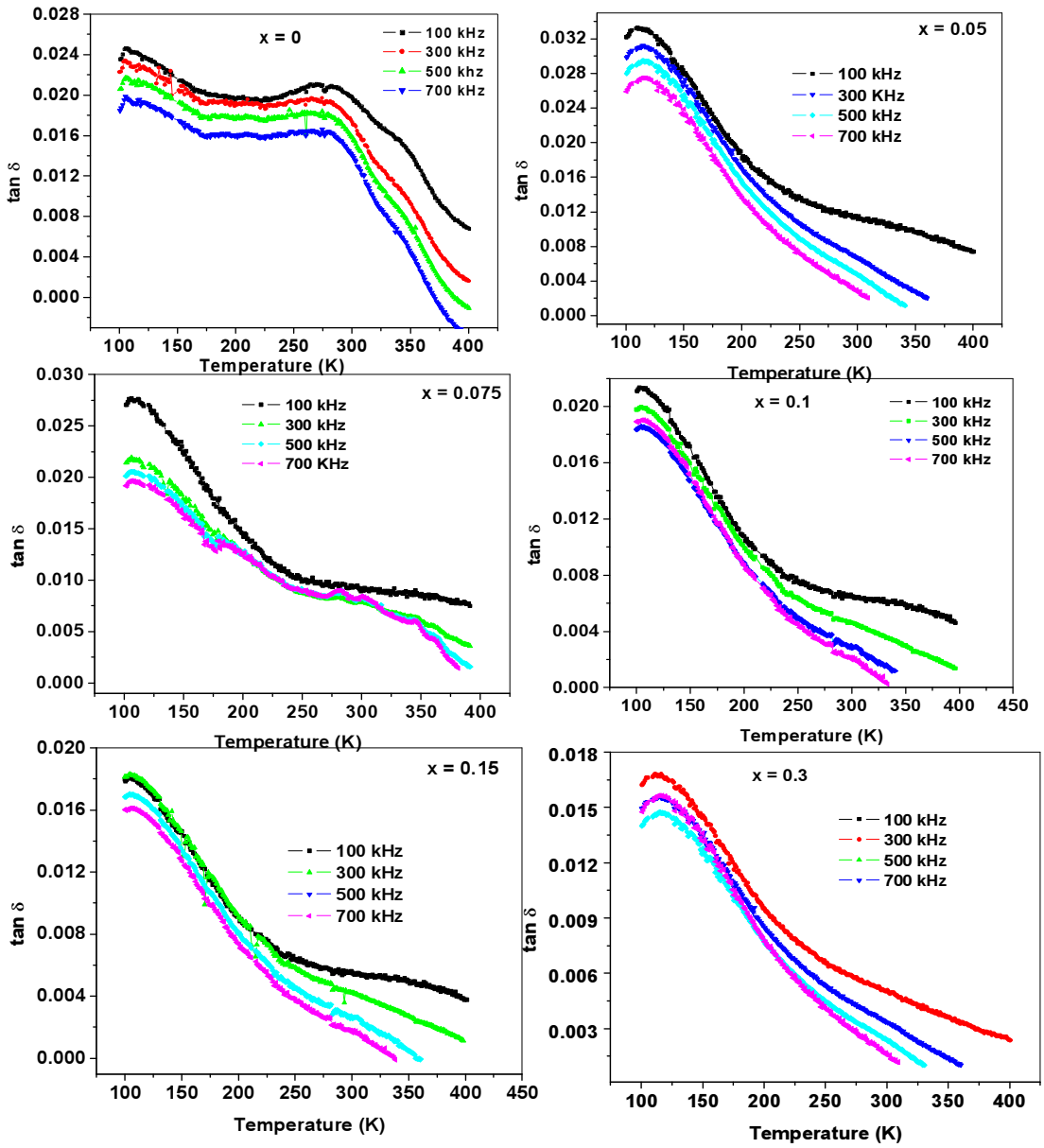

Fig. 5.5 Variation of tan δ with temperature at various frequencies in $Ba_{0.8}Sr_{0.2}(Ti_{1-x}W_x)O_3$ samples

The dissipation in ferroelectric materials occurs due to various causes such as domain wall relaxation, space charge accumulation at grain boundaries, dipolar losses etc. [15, 21]. The presence of oxygen vacancies, which act as space charge and contribute to the electrical polarization, can be related to the dielectric loss [22]. The substitution of higher valent W^{6+} for Ti^{4+} leads to the formation of cation vacancies which effectively reduces the concentration of oxygen vacancies [23]. This reduction in oxygen vacancies is responsible for the reduction in the observed loss as shown in Fig. 5.6.

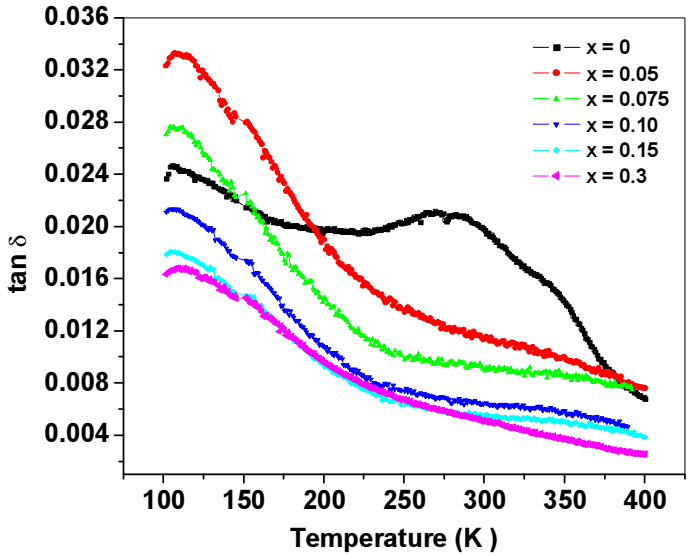

Fig. 5.6 Variation of dielectric loss with temperature at 100 kHz

5.2.2.2 Conductivity Studies

DC Conductivity

The temperature dependence of the resistivity of tungsten- substituted barium strontium titanate is depicted in Fig. 5.7. Such an irregular variation has also been observed by others [27-30]. The curves show PTCR behavior. Also, it can be seen that resistivity increases on addition of tungsten in barium strontium titanate and it is dependent on the dopant content. It is observed that the microstructure variation by doping affect the electrical resistivity [31].

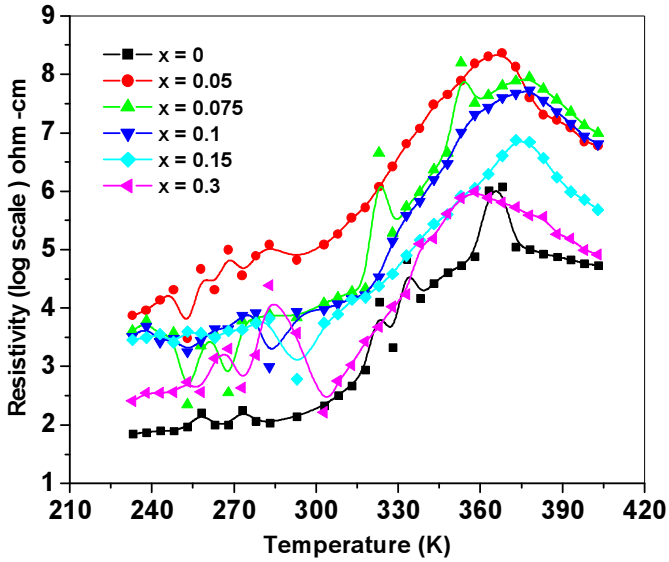

Fig. 5.7 Variation of dc resistivity with temperature.

5.2.2.3 Impedance Analysis

Fig. 5.8 shows the complex impedance plots of the $Ba_{0.8}Sr_{0.2}(Ti_{1-x}W_x)O_3$ samples with different tungsten content and temperatures. The impedance spectra are characterized by the appearance of semicircular arcs, with some degree of decentralization (i.e., having their centers below the real axis). This decentralization or Non- Debye type relaxation obeys the Cole- Cole formalism [32], where the depressed semicircle represents typically relaxation phenomena with a spread of relaxation time. The Z'-Z" plots of the W substituted samples at small tungsten concentration contain a single semicircle which represents the impedance contribution of the grains. However, at higher temperature two semicircles are formed indicating that the contribution from grain boundaries is also significant (Table 5.3). The high frequency semicircle corresponds to grain contribution and the low frequency semicircle corresponds to the grain boundary effect (magnified view given in the inset) [33]. The calculated values of R_b and R_{gb} of the samples are given in Table 5.3.

The values of bulk resistance R_b and grain boundary resistance R_{gb} were calculated from intercept of the semicircle on the real axis.

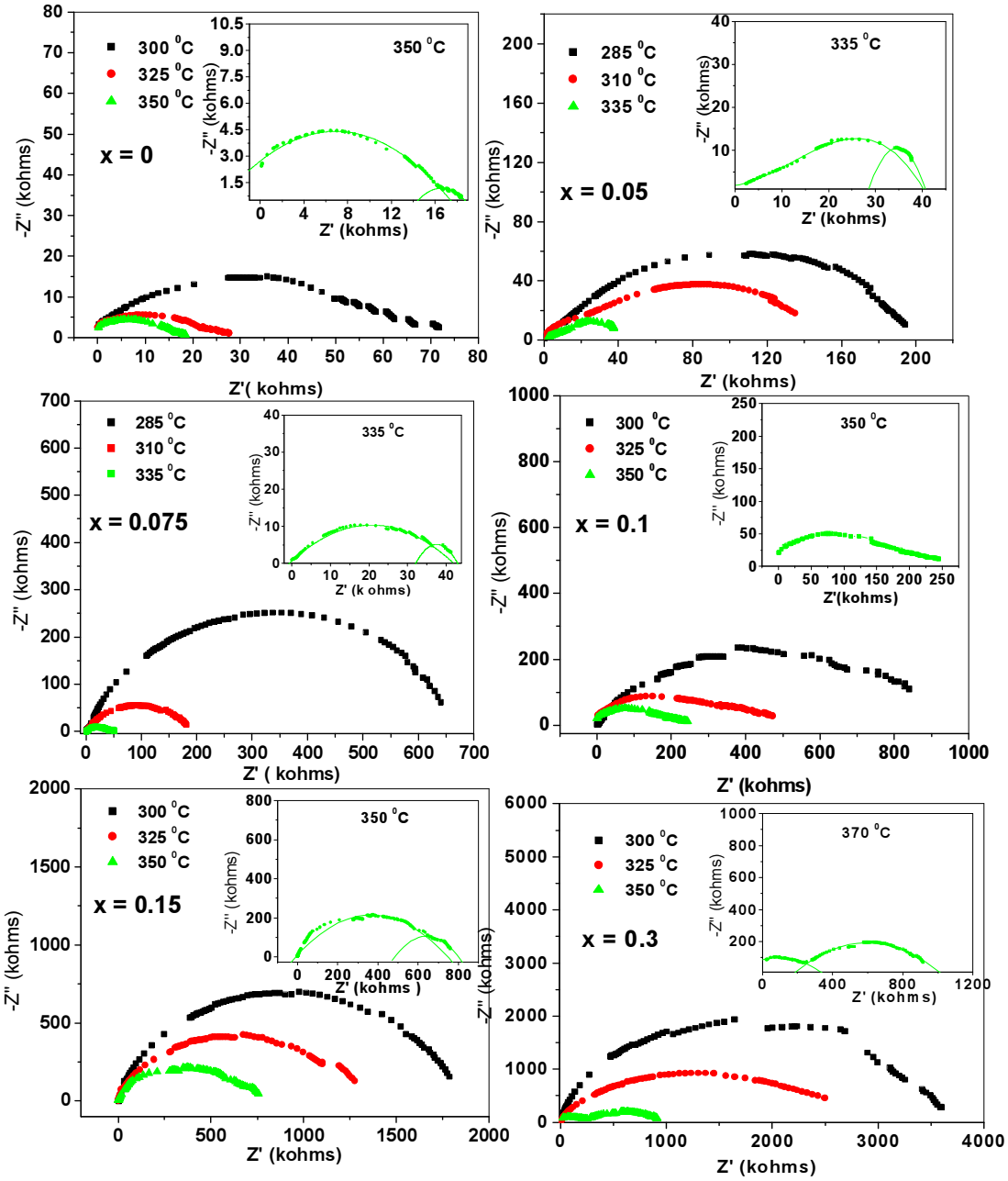

Fig. 5.8 Cole-Cole (Nyquits) plots of $Ba_{0.8}Sr_{0.2}(Ti_{1-x}W_x)O_3$, x = 0.0-0.3

It is also observed that with the increase in tungsten content, the bulk resistance of the specimen increases. The oxygen vacancies are considered to be the most mobile ionic charge carriers in the pervoskite oxides [34]. In the W- containing

samples the substitution of W^{6+} onto Ti^{4+} sites is accompanied by the formation of cation vacancies and subsequent elimination of oxygen vacancies [35]. It is due to the decrease in the concentration of the oxygen vacancies that a decrease in conductivity with increasing concentration of tungsten is observed.

Table 5.3 Grain resistance R_g, grain boundary resistance R_{gb} and capacitance of $Ba_{0.8}Sr_{0.2}(Ti_{1-x}W_x)O_3$; x = 0.0-0.3

Composition	**Temperature (^{0}C)**	**R_g (kΩ)**	**R_{gb} (kΩ)**	**C_g (nF)**	**C_{gb} (nF)**
x = 0	300	73.275	-	0.43	-
	325	28.055	-	0.40	-
	350	17.390	18.751	0.35	0.36
x = 0.05	285	204.48	-	0.70	-
	310	163.36	-	0.62	-
	335	40.51	-	0.41	-
x = 0.075	285	658.97	-	0.86	-
	310	183.75	-	0.37	-
	335	41.725	42.997	0.22	0.28
x = 0.1	300	846.42	-	0.77	-
	325	476.65	-	0.42	-
	350	256.55	-	0.31	-
x = 0.15	300	1799.55	-	0.24	-
	325	1117.06	-	0.21	-
	350	766.162	819	0.20	0.33
x = 0.3	300	3659.59	-	0.18	-
	325	2722.14	-	0.16	-
	350	332.414	1001.51	0.11	1.85

Fig. 5.9 shows the variation of relaxation time {ln (τ_b)} with 10^3/ T (K^{-1}) for all the samples. It is observed that the value of τ_b decreases with increase in temperature for all the samples and its temperature dependence follows the Arrhenius relation,

$$\tau_b = \tau_o \exp\left(\frac{-E_a}{k_B T}\right)$$

where τ_o is the pre-exponential factor, k_B is Boltzmann constant, T the absolute temperature and E_a activation energy. The value of activation energy (E_a) calculated from the slope of ln (τ_b) versus $10^3/T$ curve is shown in Table 5.4.

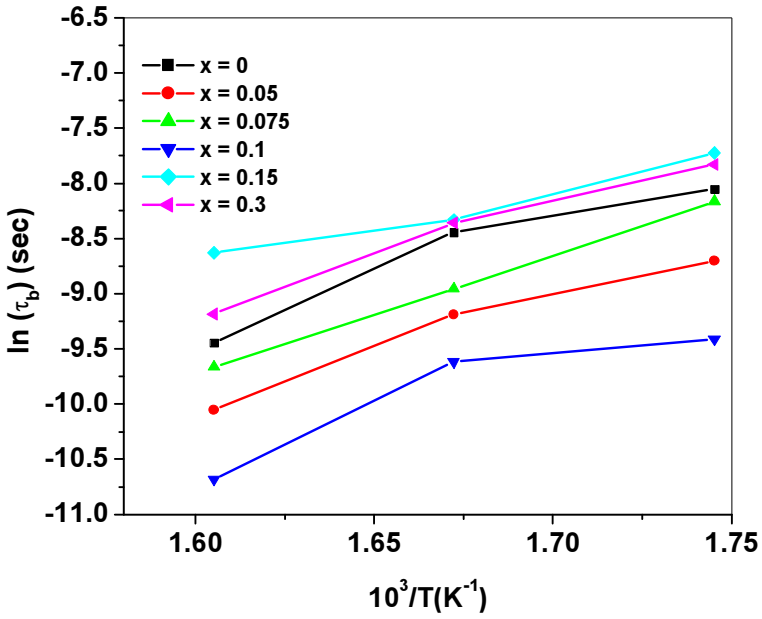

Fig. 5.9 Temperature variation of relaxation time in $Ba_{0.8}Sr_{0.2}(Ti_{1-x}W_x)O_3$ x = 0.0-0.3 samples

Fig. 5.10 shows the variation of σ with 10^3/ T (K^{-1}) for all the samples. The bulk conductivity (σ) of the samples have been evaluated from the impedance spectrum using the relation

$$\sigma = \frac{t}{R_b A}$$

where, R_b is the bulk resistance, t is the thickness and A is the area of the sample. It is observed that with increasing temperature conductivity increases confirming the negative temperature coefficient of resistance behaviour in the compound. The observed variation of ln σ vs. 10^3/ T (K^{-1}) is a straight line and follows the Arrhenius relationship

$$\sigma = \sigma_0 \exp\left(\frac{-E_a}{k_B T}\right)$$

where, σ_0 is the pre- exponential factor, E_a is the activation energy of the charge carriers, and T is the absolute temperature.

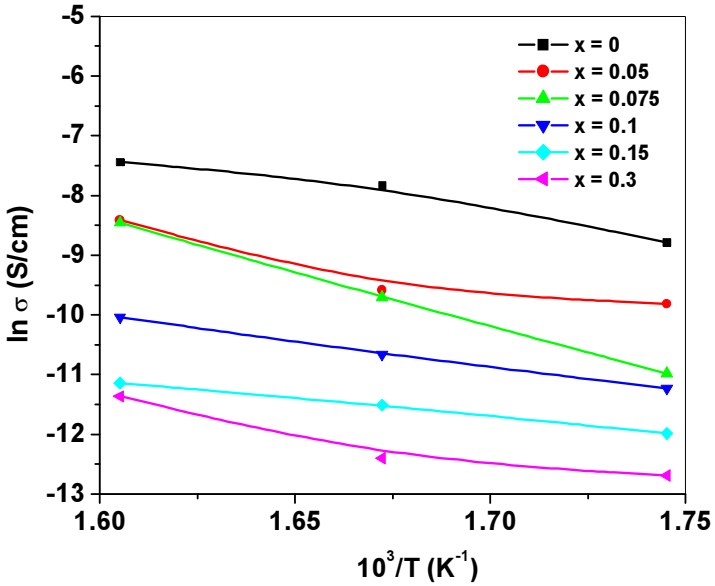

Fig. 5.10 Temperature variation of bulk conductivity in $Ba_{0.8}Sr_{0.2}(Ti_{1-x}W_x)O_3$ x = 0.0-0.3 samples

The values of activation energy (E_a) as calculated from the curve ln σ with 10^3/ T (K^{-1}) are shown in Table 5.4, which is nearly the same as that obtained from the relaxation time (τ_b) versus temperature curve.

Table 5.4. Activation energy calculated from conductivity and relaxation time curve

Composition	**E_a(from conductivity curve) (eV)**	**E_a (from relaxation time) (eV)**
x = 0	0.83	0.85
x = 0.05	0.81	0.78
x = 0.075	0.98	0.87
x = 0.1	0.73	0.76
x = 0.15	0.51	0.55
x = 0.3	0.81	0.83

Nearly the same values of E_a, from the two methods, suggest that relaxation and conduction processes may be attributed to the same type of charge carriers. This value of E_a is approximately the same as the energy required (~ 1 eV) for the motion of oxygen vacancies [36]. This confirms that the observed conductivity is due to the motion of oxygen vacancies in the material.

5.2.2.4 Ferroelectric Studies

Fig. 5.11 illustrates the hysteresis loops of the studied samples recorded at a frequency of 50 Hz. All the samples exhibit well- defined P-E hysteresis loops.

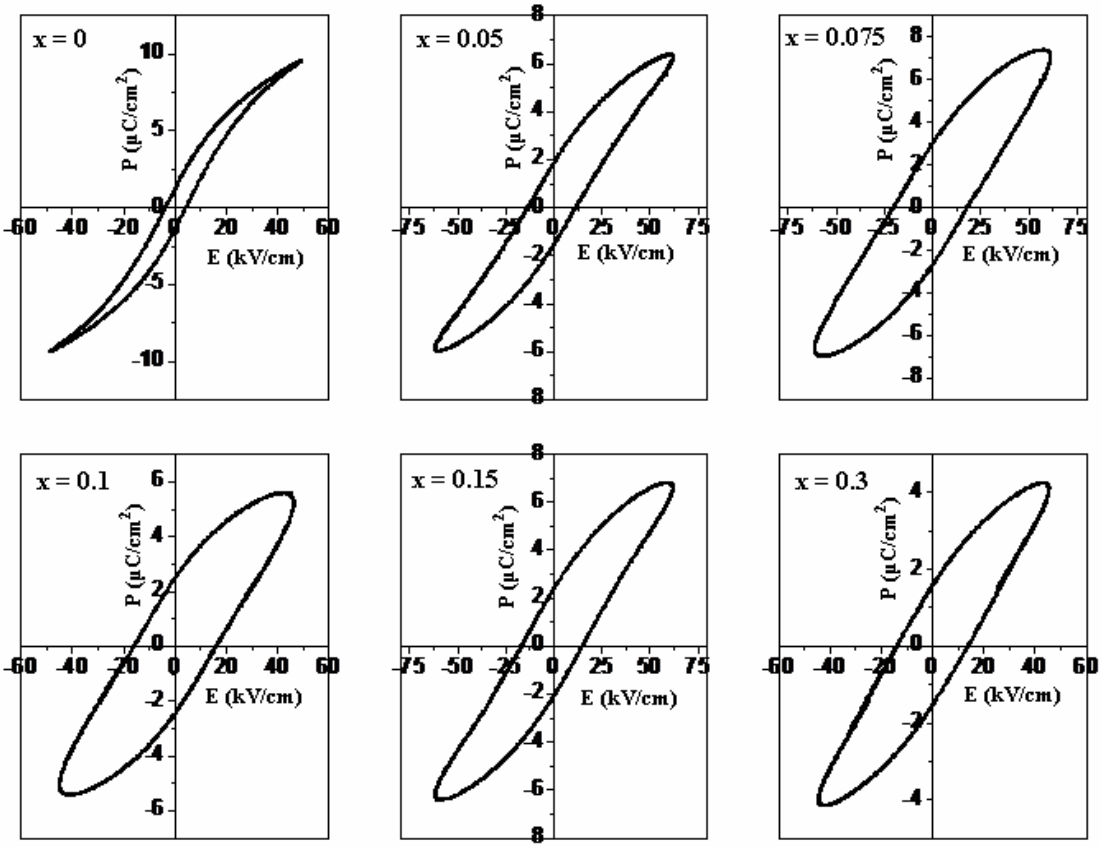

Fig. 5.11 P- E hysteresis loop in $Ba_{0.8}Sr_{0.2}(Ti_{1-x}W_x)O_3$ samples

It is observed that the values of remanent polarization (P_r) and coercive field (E_c) are dependent on W content of the specimen. It is further observed that P_r value

increases monotonically upto x = 0.075 and there is a decrease in remanent polarization thereafter. It is reported that defects such as oxygen vacancies act as space charge and influences the ferroelectric properties of these materials [37, 38].

Table 5.5 Values of remanant polarization and coercive field in $Ba_{0.8}Sr_{0.2}(Ti_{1-x}W_x)O_3$ x = 0.0-0.3

x (composition)	**P_r ($\mu C/cm^2$)**	**E_c (kV/cm)**
x = 0	1.31	4.10
x = 0.05	1.91	12.41
x = 0.075	2.93	19.20
x = 0.1	2.65	16.39
x = 0.15	2.22	15.79
x = 0.3	1.56	13.97

In the W- containing samples, as discussed earlier, the suppression of the oxygen vacancies reduces the pinning effect on the domain walls, leading to enhanced remanent polarization [39]. The reduction of P_r at higher tungsten concentration seems to be due to the presence of secondary phase (as observed in XRD diffractograms) which hampers the polarization switching process [40-41].

5.3 Conclusions

Based on the above observations and discussions the following conclusions can be drawn**.**

- A single phase pervoskite structure is maintained in the range $0.0 \leq x \leq 0.05$ in tungsten substituted barium strontium titanate specimens.
- Lattice parameters, unit cell volume and tetragonal strain decrease with increasing tungsten content.

- The Curie temperature reduces from 347 K to 295 K on tungsten substitution.
- At higher W concentration, it is observed that interdiffusion of grains takes place and the boundaries of the grains are not so sharp. The average observed grain size is found to be approximately in the range of 0.5 to 1.5 μm.
- Curie temperature remains the same at all the frequencies indicating non-relaxor behaviour and all compounds exhibit ferroelectric-paraelectric diffuse phase transition.
- Dielectric constant as well as loss decreases with increase in frequency.
- Dielectric constant increases for low concentration (x = 0.05) of W substitution and reduces for higher concentrations.
- The dielectric loss reduces significantly on tungsten substitution.
- W substitution enhances the remnant polarization of the specimen and the maximum observed value of remnant polarization is 2.93 $\mu C/cm^2$.
- Substitution of tungsten is found to be effective in eliminating oxygen vacancies which decreases the conductivity of the studied specimens.
- Nearly equal values of E_a suggest that the relaxation and conduction processes may be attributed to the same type of charge carriers, i. e., oxygen vacancies.

References

[1] Al-Allak, H. M. Birnkman, A.W. Russel, G. J. Roberts and J. Wood, *J. Phys. D: Appl. Phys.* **21** (1998) 1226.

[2] J. IIingsworth, H. M. Al- Allak and A. W.Brinkman, *J. Phys. D: Appl. Phys* **23** (1990) 971.

[3] A. J. Moulson and J. M. Herbert, Electroceramics: Materials, properties and Applications, Second Edition, John Wiley & sons. Inc. England

[4] U. Syamaprasad, R. K. Galgali and B. C. Mohanty, *Mater. Lett*. **7** (1988) 197-200.

[5] R. Thomas, V. K. Varadan, S. Kormaneni and D. C. Dube, *J. Appl. Phys.* **90** (2001) 1480.

[6] Cheng Zhang, Yuanfang Qu and Shicai Ma, *Materials Science & Engineering B*, **136** (2007) 118-122.

[7] S. Y. Wang, B. L. Cheng, Can Wang, H. B. Lu, Y. L. Zhou, Z. H. Chen and G. Z. Yang, *Journal of Crystal Growth* **259** (2003) 137-143.

[8] Tao Hu, Tim J. Price, David M. Iddles, Antti Uusimaki, Heli Jantunen, *Journal of the European Ceramic Society* **25** (2005) 2531-2535.

[9] Yanhua Fan, Shuhui Yu, Rong Sun, Lei Li, Yansheng Yin and Ruxu Du, *Thin Solid Films* **518** (2010) 3610-3614.

[10] Yuanliang Li and Yuanfang Qu, *Materials Research Bulletin* **44** (2009) 82-85.

[11] Yun Ye and Tailiang Guo, *Ceramic International* (In Press).

[12] A. K. Jha and R. G. Mendiratta, *J. Mater. Sci*. **31**(1996) 1735.

[13] C. Dong, *J. Appl Cryst*. **32** (1999) 838.

[14] M. Ghita, M. Fornari, D. J. Singh, S. V. Halilov, *Phys. Rev.B* **72** (2005) 054114.

[15] R. R. Das, P. Bhattacharya, W. Perez and R.S. Katiyar, *Ceram. International*, **30** (2004) 1175.

[16] R. Rai, S. Sharma and R. N. P Choudhary, *Solid State Comm*. **133** (2005) 635.

[17] Y. Zhu, X. Zhang, P. Gu, P. C. Joshi and S. B. Desu, *J. Phys. Condens. Matter*, **9** (1997) 10225.

[18] R. Rai, S. Sharma and R. N. P. Choudhary, *Mater. Lett.,* **59** (2005) 3921.

[19] A. Chen, Y. Zhi and L.E. Cross, *Phys. Rev. B* **62** (2000) 228.

[20] Cao Wanqiang, Junwen Xiong, Sun Juanpin, *Materials Chemistry and Physics* **106** (2007) 2-3, 338-342.

[21] Y.H. Xu, *Ferroelectric Materials and their Applications (Elsevier Science Publishers,* Amsterdam, 1991 P.131.

[22] I. Coondoo, A. K. Jha and S. K. Agarwal, Ceram. Int. **33**(2007) 41.

[23] Yong Zhang, Zhilun Gui, Longtu Li, Jiemo Tian, *Materials Science & Engineering B* **83** (2001) 66-69.

[24] R. Rai, S. Sharma, R.N.P. Choudhary, *Mater. Lett.* **59** (2005) 3921-3925.

[25] N. Zhong, X-L. Dong, D-Z.Sun, P-H. Xiang, H. Du, *Mater. Res. Bull.* **39** (2004) 175-184.

[26] N. Setter, L. E. Cross, *J. Appl. Phys.* **51** (1980) 4356-4360.

[27] A. M. Slipenyuk, M. D. Glinchuk, V. V. Laguta, I. P. Bykov, A. G. Bilous, O.I. Vyunov, *Ferroelectrics*, **288** (2003) 243-251.

[28] Zeming He, J. Ma, Yyanfang Qu, Xuemei Feng, *Journal of European Ceramic Society* **22** (2002) 2143-2148.

[29] P. Bomlai, N. Sirikulrat, T. Tunkasiri, *Materials Letters*, **59** (2005) 118-122.

[30] Il-Ho Kim, Ho- Won Lee, Young –Min Kim, Hyun- Joo Kim, Soon- Chul Ur, *Materials Letters* **60** (2006) 3027-3030.

[31] H. T. Langhammer, T. Muller, R. Bottcher, H. P. Abicht, *Solid State Sci.* **5** (2003) 965.

[32] M.A.L. Nobre, S. Lanfredi, *J. Physics and Chemistry Solids* **64** (2003) 2457-2464.

[33] B. Behera, P. Nayak, R.N.P. Choudhary, *J. Alloys and Comp.* **436** (2007) 226-232.

[34] D. M. Smyth, *Ferroelectrics*, **117** (1991) 117-124.

[35] Lina Zhang, Suchuan Zhao, Hanfeng Yu, Liaoying Zheng, Guorong Li and Qingrui Yin, Japanese, *Journal of Applied Physics*, **43** (2004) 7613-7617.

[36] S. Sen, P. Pramanik and R.N.P Choudhary, *Physica B*, **52** (2007) 387.

[37] Y. Noguchi, I. Miwa, Y. Gosshima, M. Miyayama, Jpn. *J. Appl. Phys.***39** (Part 2) (2000) L1259.

[38] T. Friessnegg, S. Aggarwal, R. Ramesh, B. Nielsen, E. H. Poindexter, D. J. Keeble, *Appl. Phys. Lett*. **77** (2000) 3126.

[39] Indrani Coondoo, A. K. Jha and S. K. Agarwal, *Ferroelectrics*, **356** (2007) 31-39.

[40] J. J. Shyu, C.C. Lee, *J. Eur. Ceram. Soc*. **23** (2003)1167-1173.

[41] C. H. Lu, C. Y. Wen, *Materials Letter.* **38** (1999) 278-282.

Chapter 6

Chapter 6

Synthesis and Characterization of $Ba(Ti_{1-x}W_x)O_3$ by Mechanical Activation Process

6.1 Introduction

It is well known that the characteristics of a material are dependent on the way it is processed. Synthesis methods of ferroelectric materials play a significant role in determining the microstructural, electrical and optical properties [1-3]. Very commonly ferroelectric materials are synthesized using solid-state reaction process. The powders require relatively high sintering temperature to obtain ferroelectric ceramics with desired compositions and characteristics [1-3]. For lead containing ferroelectrics, due to its high volatility, the lead component is very often lost during the sintering at high temperatures deteriorating the electrical, optical and other useful characteristics. To reduce sintering temperature, it is necessary to use powders with small particle size and narrow size distribution. Various wet-chemistry methods in the last decades, including chemical coprecipitation [4-7], sol-gel process [8-11], hydrothermal synthesis [12-18], microemulsion, combustion [19], thermal pyrolysis spray, molten salt [20,21], etc., have been used to get the ferroelectric compounds with desired properties. Although significant progresses have been made but there are limitations. For examples, sol-gel process uses metal alkoxides as the starting materials, which are very expensive and extremely sensitive to the environmental conditions such as moisture, light and heat. Moisture sensitivity makes it necessary to conduct the experiment in dry boxes or clean rooms. Co-precipitation processes involve repeated washing in order to eliminate the

anions coming from the precursor salts used, making the process complicated and very time consuming. Furthermore, it is difficult to produce large batches by using most of the chemical solution processing routes. Therefore, exploring alternative methods for the preparation of ferroelectric ceramics is crucial.

Recently, mechnoactivation technique, has been successfully employed to synthesize a wide range of nano-sized ceramics powders, such as ZrO_2 [22, 23], Fe_2O_3 [24, 25], YBCO superconductor [26], ferrite [27-29], as well as various ferroelectric materials [30-41]. The most significant characteristic of this technique is the formation of the desired compound is due to reactions of oxides precursors which are activated by mechanical energy, instead of the heat energy required in the conventional solid-state process. It uses cost-effective and widely available oxides as the starting powders and skips the intermediate calcination step, leading to a simpler process. Also, it takes place at room temperature in well sealed containers, thus effectively alleviating the loss of the volatile components, such as lead, bismuth and lithium. The high-energy milling can greatly improve the reactivity of precursors by reducing the phase formation temperatures of the some ferroelectric materials [42-46, 47-50, 40]. In view of this, tungsten substituted barium titanate was prepared by this novel technique and their structural, dielectric and ferroelectric properties were studied and have been discussed in this chapter.

6.2 Results and Discussions

6.2.1 Micro-structural Characterization

Fig. 6.1 shows the XRD patterns of the barium titanate powders milled for different durations, i.e., 5 hours, 10 hours, 20 hours and 30 hours.

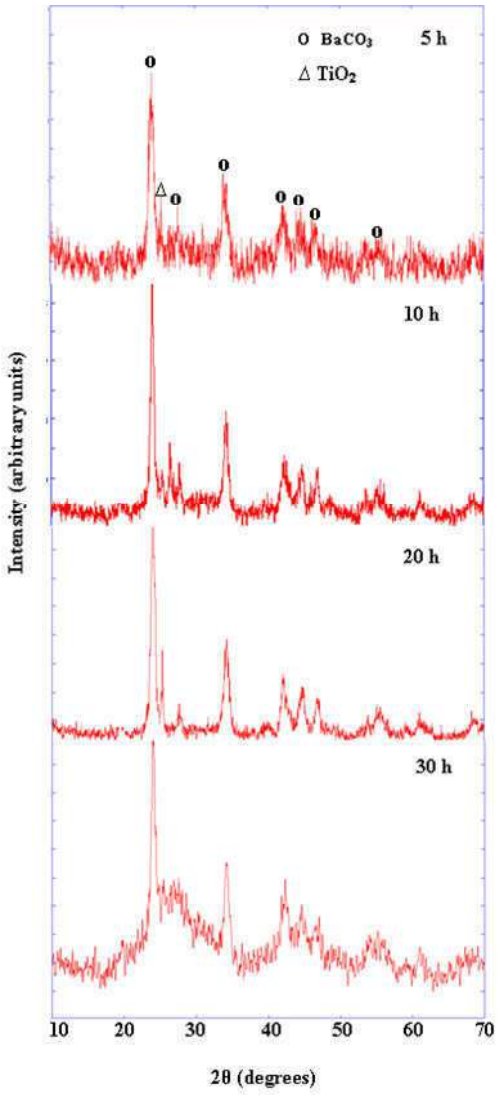

Fig. 6.1 XRD patterns of the studied samples at different milling time

It is observed that with increase milling durations peaks are slightly shifted towards lower angle and some peaks disappear in the samples milled for longer duration. However, in the as milled specimens, even after 30 hours of milling the phase is not formed properly and as discussed ahead, the specimen require sintering for the proper phase formation.

Fig. 6.2 shows the SEM images of the specimens milled for different durations. The size of the grains can be seen to be reducing with increasing milling time.

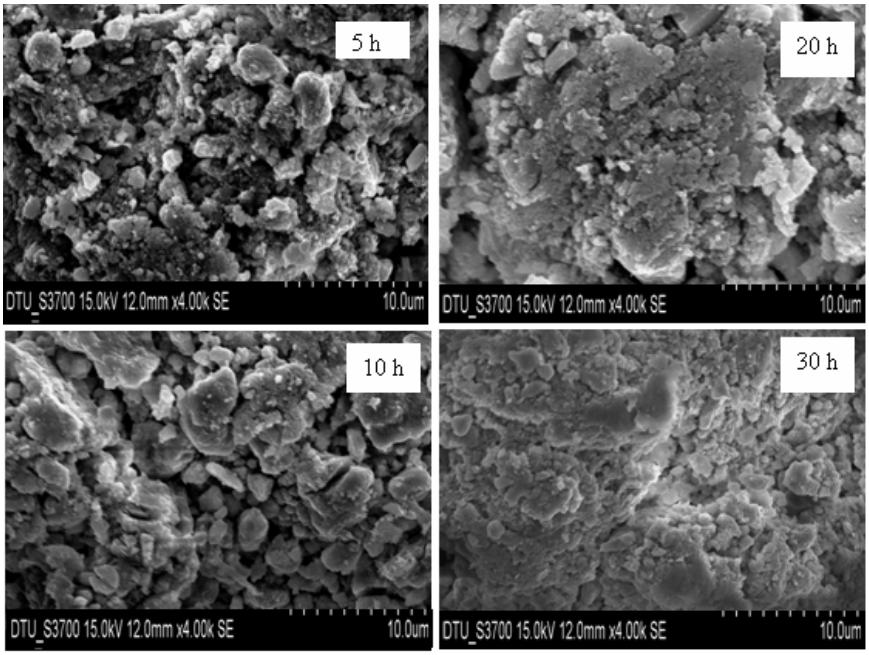

Fig. 6.2 SEM micrographs of pre-sintered barium titanate powders prepared at different milling time

The images obtained from transmission electron microscopy (TEM) and electron diffraction (ED) of the studied specimen milled for 30 hours is shown in Fig. 6.3. It can be seen that there is agglomeration of particles due to the reduction in their size. The average particle size is found in the nanometer range. The formation of particles of nanodimensions is also confirmed by electron diffraction rings showing the discrete diffraction spots.

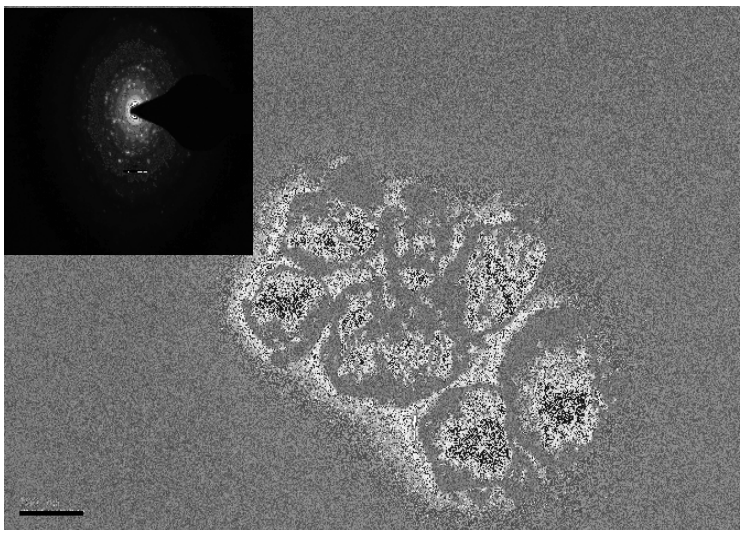

Fig. 6.3 TEM micrograph and electron diffraction pattern of 30 hours milled barium titanate powder

Fig. 6.4 shows the XRD patterns of the samples milled for different durations and sintered at 1250 ^{o}C for 2 hours. The peaks become well defined and shift slightly towards higher angles with increasing milling time. The peak at 22.5^{o} represents barium oxide in the XRD patterns of the specimens milled for lower milling durations. The indexing of the XRD peaks and determination of lattice parameters was carried out using Powder -X [51] and calculated lattice parameters are given in Table 6.1. It is observed that the compound prepared by mechanical activation process has tetragonal pervoskite structure. Using the calculated lattice parameters, unit cell volume and tetragonal strain (c/a) were calculated and are given in Table 6.1.

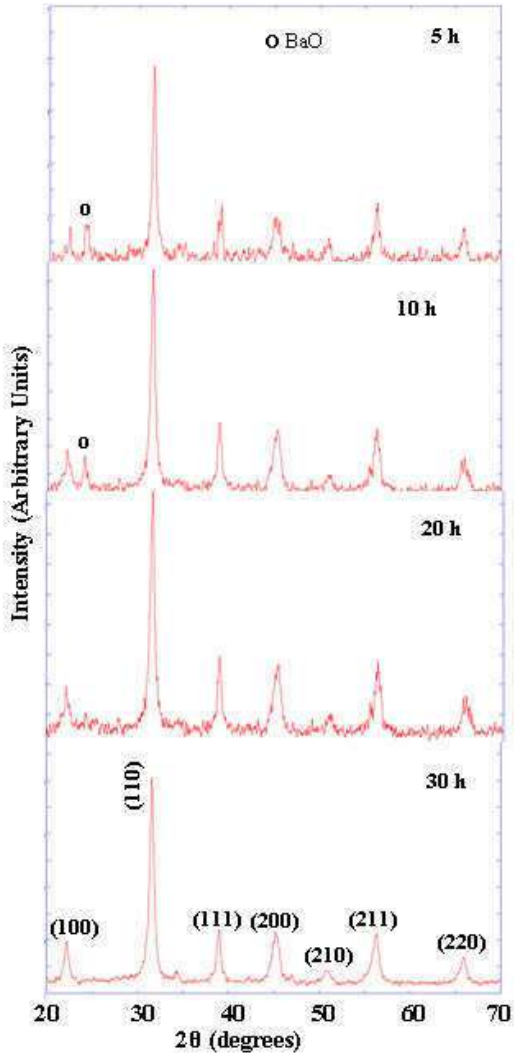

Fig. 6.4 XRD patterns of barium titanate sintered samples milled for different durations

SEM micrographs of the sintered samples milled for different durations are shown in Fig. 6.5. The average grain size, determined by linear intercept method, is observed to be in the range 0.3-0.2 μm. Grains are well defined and properly formed with increasing milling time. Grain boundaries are clearly visible at higher milling time.

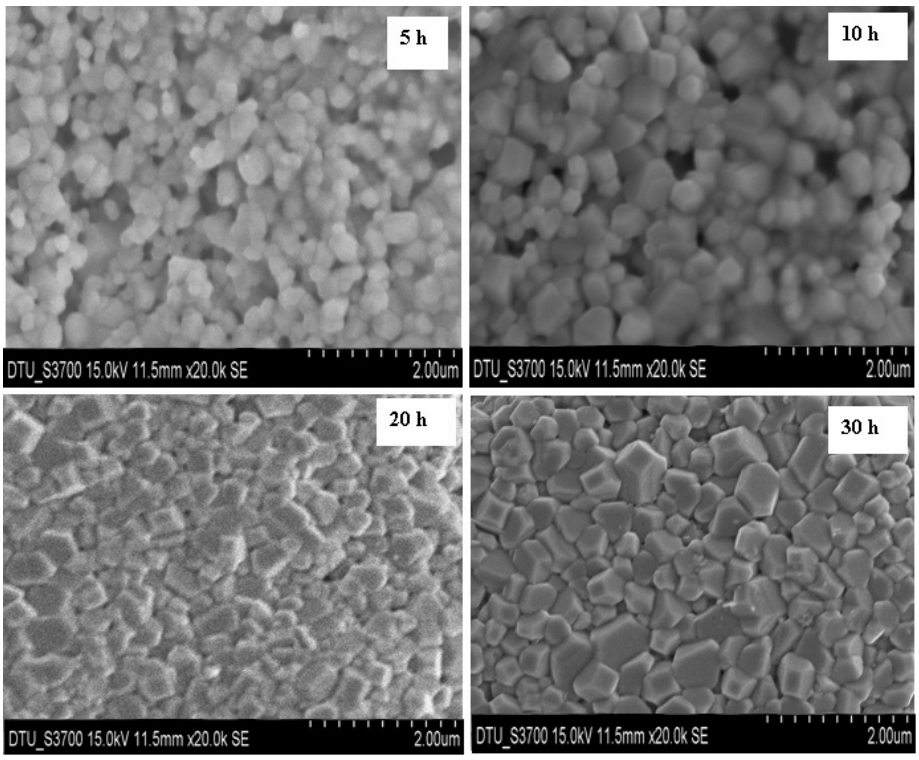

Fig. 6.5 SEM micrographs of the studied samples milled for different durations

Table 6.1 Lattice parameters, unit cell volume and tetragonal strain of the studied specimens milled for different durations

Milling time	**a (A^0)**	**c (A^0)**	**c/a**	**Volume $(A^0)^3$**
5 h	3.9831	4.0372	1.0135	64.05
10 h	3.9785	4.0313	1.0132	63.80
20 h	3.9727	4.0215	1.0122	63.51
30 h	3.9713	4.0215	1.0126	63.42

6.2.2 Electrical Characterization

6.2.2.1 Dielectric Studies

To see the effect of milling duration on the dielectric properties, (a) variation of ε′ and tan δ as a function of temperature at 100 Hz, 1 kHz, 10 kHz and 100 kHz frequencies and (b) the variation of ε′ and tan δ with frequency at room temperature were studied and are presented in this section.

Variation of ε′ with Temperature: Curie Temperature

The temperature dependence of dielectric constant (ε′) measured at 100 Hz, 1 kHz, 10 kHz and 100 kHz are shown in Fig. 6.6. For all the milling durations, the compound show dielectric anomaly at a temperature called the Curie temperature (T_c).

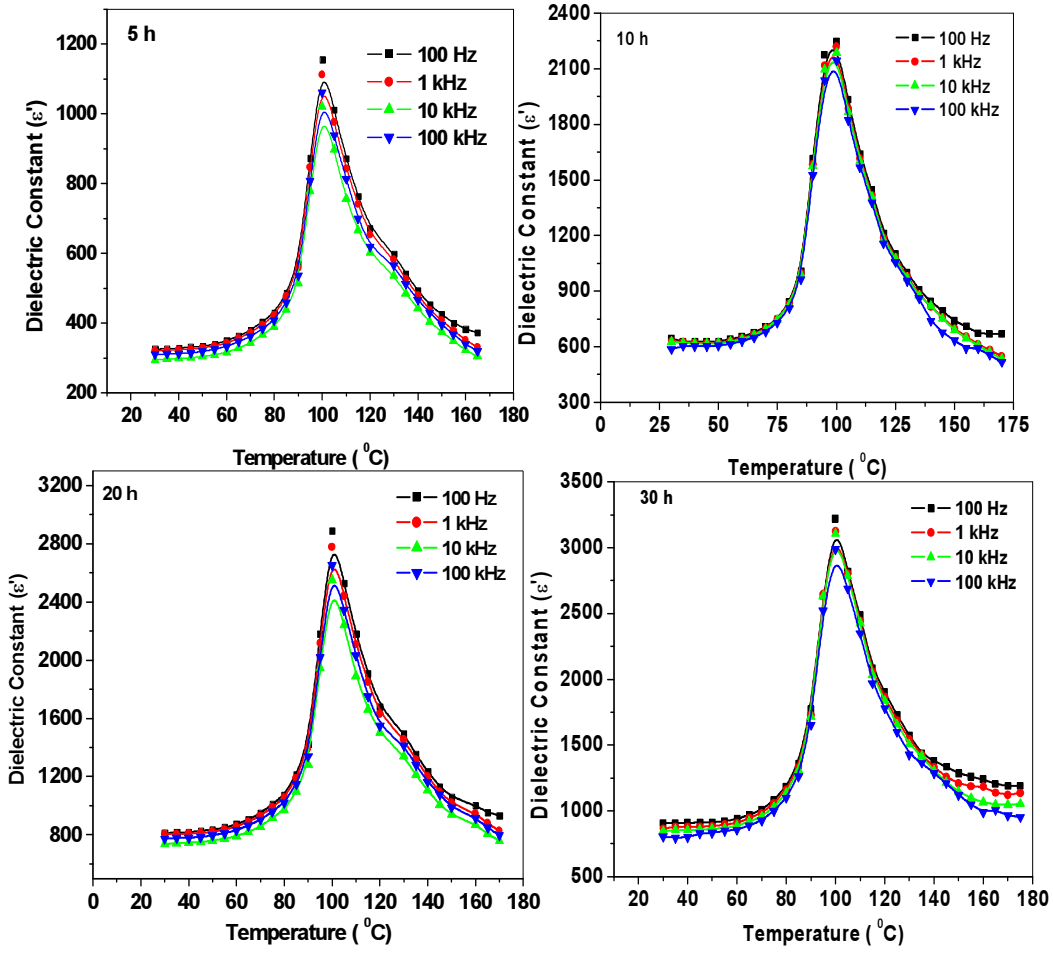

Fig. 6.6 Variation of dielectric constant (ε′) with temperature

The T_c remains the same at all the measured frequencies for milling time indicating the non-relaxor behavior of the compound. Fig. 6.7 shows the comparative variation of dielectric constant with temperature of the specimen with different milling durations at a frequency of 1 kHz. It is observed that the dielectric constant increases with increasing milling time and is maximum in the sample milled for 30 hour. Curie temperature remains the same (within experimental variation) in all the samples. The increase in dielectric constant can be understood as follows. It is known that in the fine grained ferroelectric ceramics, ε′ increases due to an increase in residual internal stress [52-56].

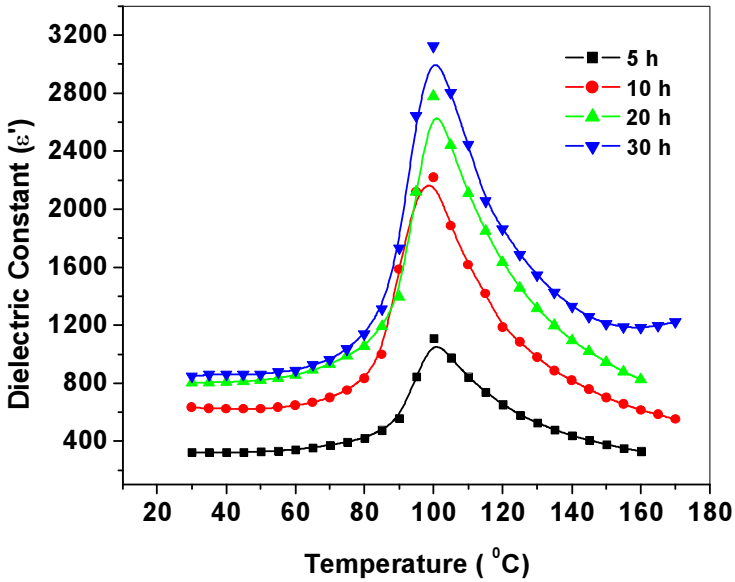

Fig. 6.7 Variation of dielectric constant with temperature at different milling time at frequency 1 kHz

The observed increase in ε′ value is due to the decrease in the average grain size with increase in milling time. The small observed reduction of unit cell volume (Table 6.1) with increase in milling duration may additionally be increasing the observed dielectric constant as can be followed from Clausis-Mossotti relation:

$$\varepsilon' = \left(\frac{3V_m + 8\pi\alpha_D}{3V_m - 4\pi\alpha_D}\right) = 1 + \left(\frac{12\pi(\alpha_D / V_m)}{3 - 4\pi(\alpha_D / V_m)}\right)$$

where V_m (= $V_{unit\ cell}/Z$) is the molar volume and α_D is the net dielectric polarizability.

Variation of tan δ with Temperature

Fig. 6.8 shows the temperature variation of dielectic loss (tan δ) of the studied specimens at different frequencies.

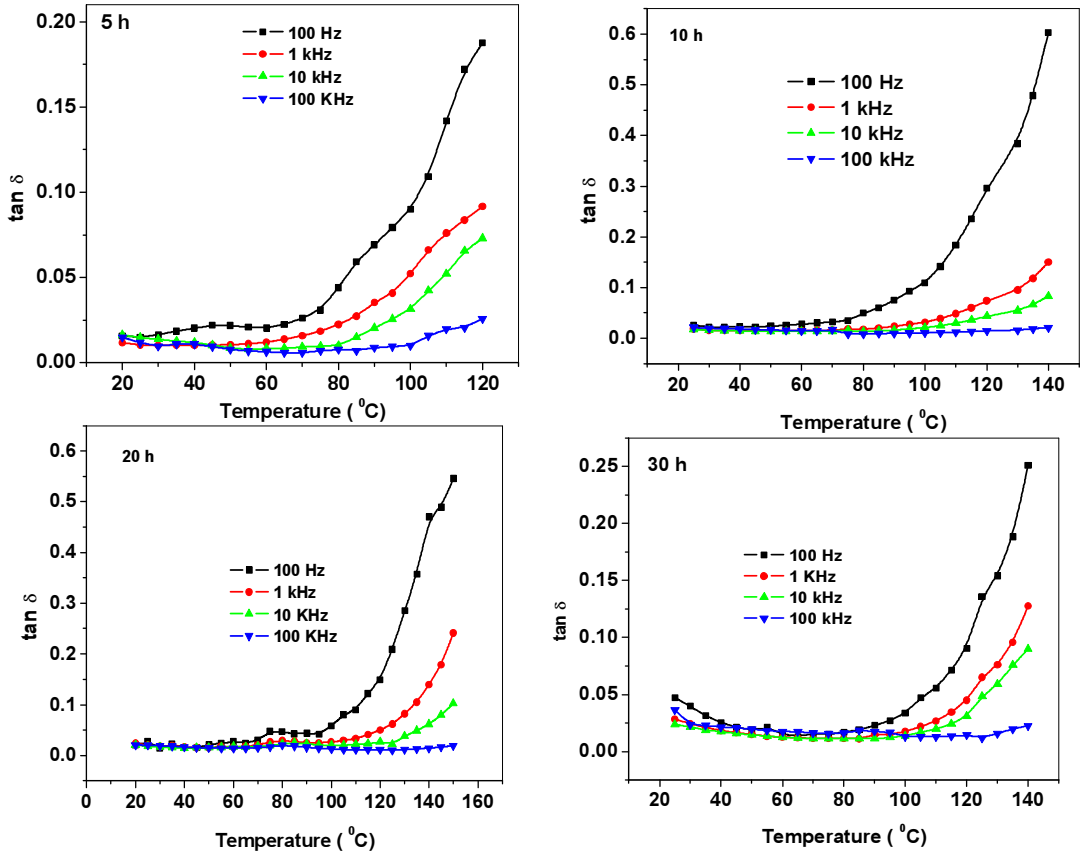

Fig. 6.8 Variation of dielectric loss (tan δ) with temperature

In all the samples, the dielectric loss (tan δ) has smaller value at lower temperature and is nearly independent of temperature upto 90 °C and at higher temperatures it increases sharply. This sharp increase of dielectric loss in high temperature region may be attributed to the increased mobility of space charges

arising from the defects or vacancies (like oxygen vacancies) in the samples [57]. Fig. 6.9 shows the variation of dielectric loss with temperature at different milling duration at 1 kHz. It can be seen that the dielectric loss is lowest in the specimen milled for 30 hours.

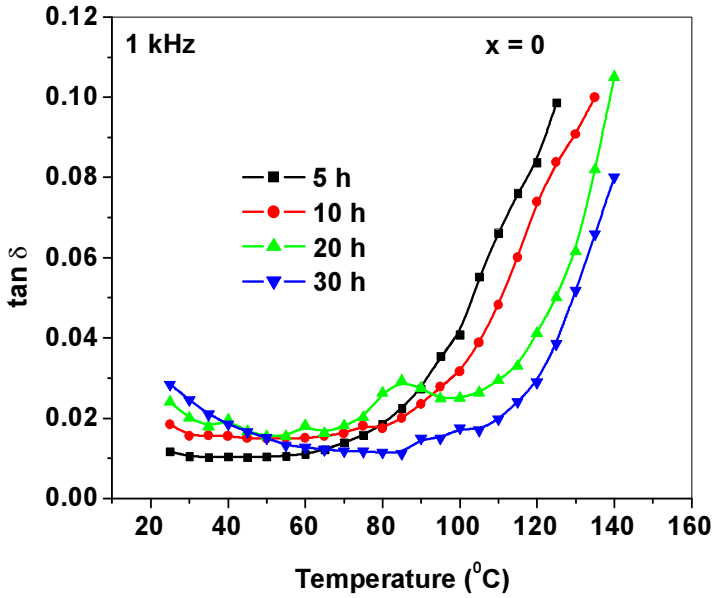

Fig. 6.9 Variation of dielectric loss with temperature

Variation of ε′ and tan δ with Frequency

Figs. 6.10 (a) and (b) show the variation of dielectric constant and dielectric loss as a function of frequency at room temperature in the specimens milled at different durations. In all the samples, both dielectric constant and dielectric loss decrease up to 1 kHz and remains nearly constant beyond this frequency. At lower frequencies, the dipoles follow the oscillating electric field resulting in higher values of dielectric constant and loss while at higher frequencies the dipoles are unable to follow the rapidly changing field leading to the reduction in the values of dielectric constant and loss. It is worth noting that the room temperature dielectric constant value is highest at room temperature and dielectric loss is lowest in the sample milled for the 30 hours.

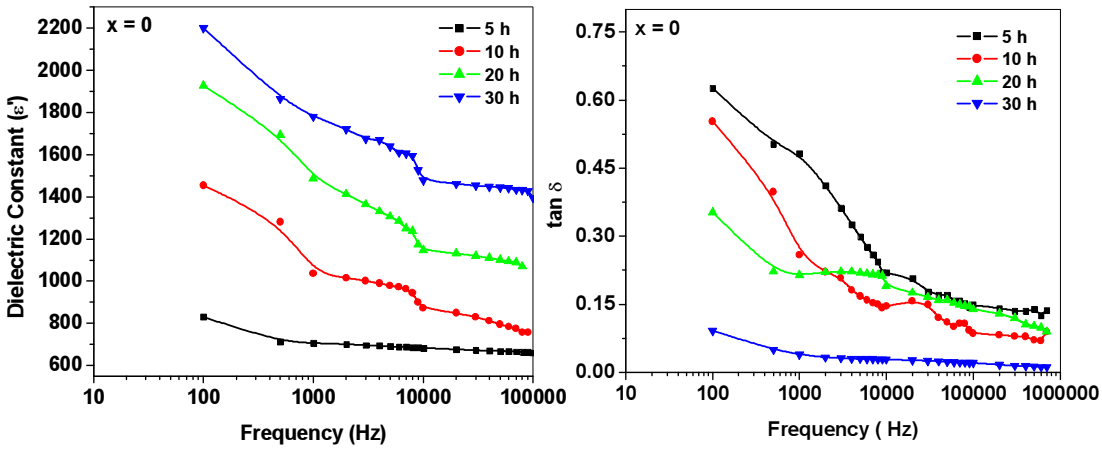

(a) (b)

Fig. 6.10 Variation of (a) dielectric constant and (b) dielectric loss with frequency at room temperature

6.2.2.2 Ferroelectric Properties

Fig. 6.11 illustrates the P-E hysteresis loops of the studied specimens milled for different duration at room temperature at a frequency of 50 Hz. The existence of well defined hysteresis loops is confirming the ferroelectric nature of the studied samples prepared by mechanical activation method.

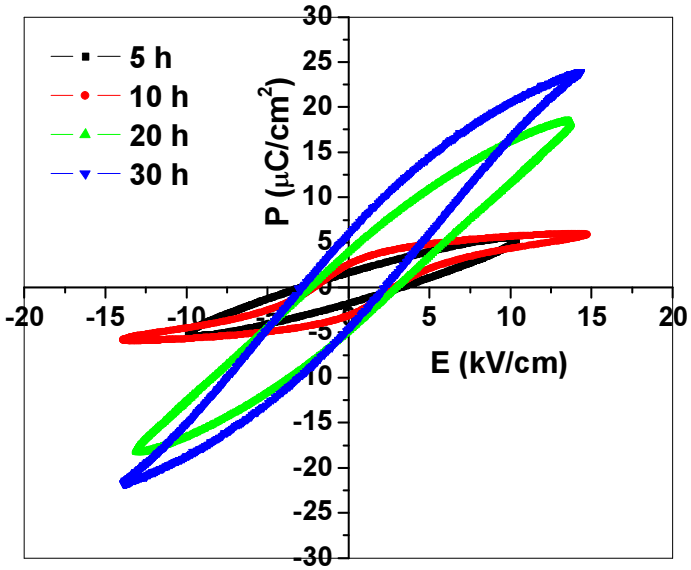

Fig. 6.11 P-E hysteresis loops of the studied specimens

The remanent polarization is found to be higher for the sample milled for longer duration and maximum value of remanent polarization (P_r) and coercive field (E_c) is observed to be 5.163 $\mu C/cm^2$ and 2.566 kV/cm.

6.2.2.3 Piezoelectric Properties

Fig. 6.12 shows the variation of piezoelectric coefficient (d_{33}) with milling time. It is observed that d_{33} value increases with increasing milling duration. It can be understood in terms of smaller grain size. Smaller grains have larger number of grain boundaries which results in the increase of internal electric fields generated by space charge layers at grain boundary [58], resulting in increased piezoelectric coefficient.

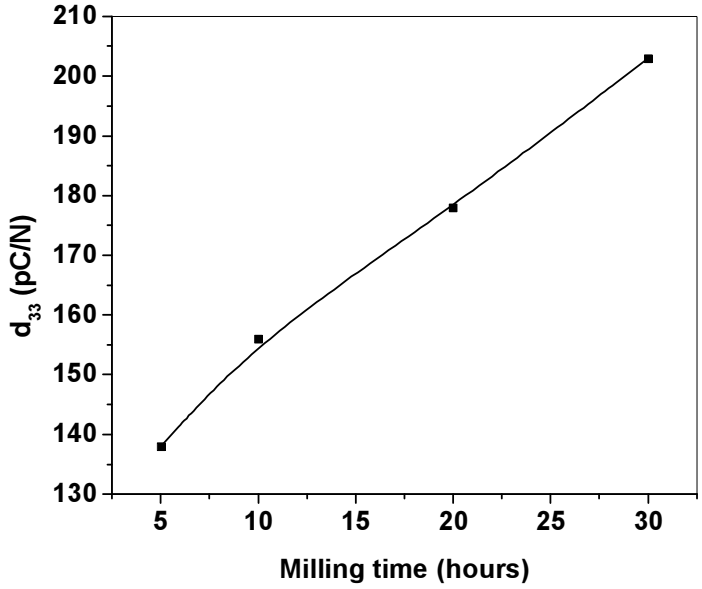

Fig. 6.12 Variation of piezoelectric coefficient with different milling durations

6.2.3 Structural Characterization of $BaTi_{0.95}W_{0.05}O_3$ Milled for Different Durations

X-ray Diffraction

Figs. 6.13 (a) and (b) show the XRD patterns of the composition $BaTi_{0.95}W_{0.05}O_3$ powder milled for different durations before and after sintering at 1250 ^oC for 2 hours.

The diffraction peaks shift slightly with milling time and some peaks disappear at higher milling time. The peak intensities of WO_3 and TiO_2 decrease with an increasing milling time.

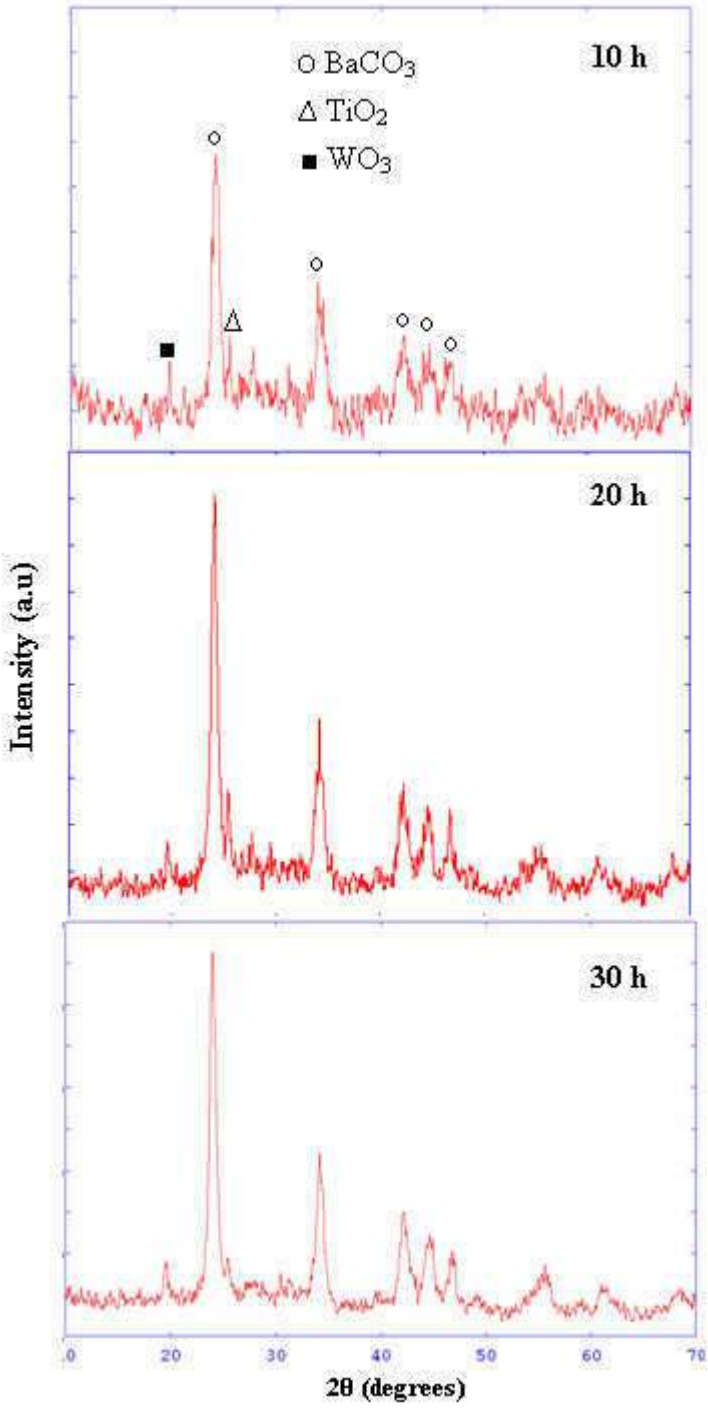

(a)

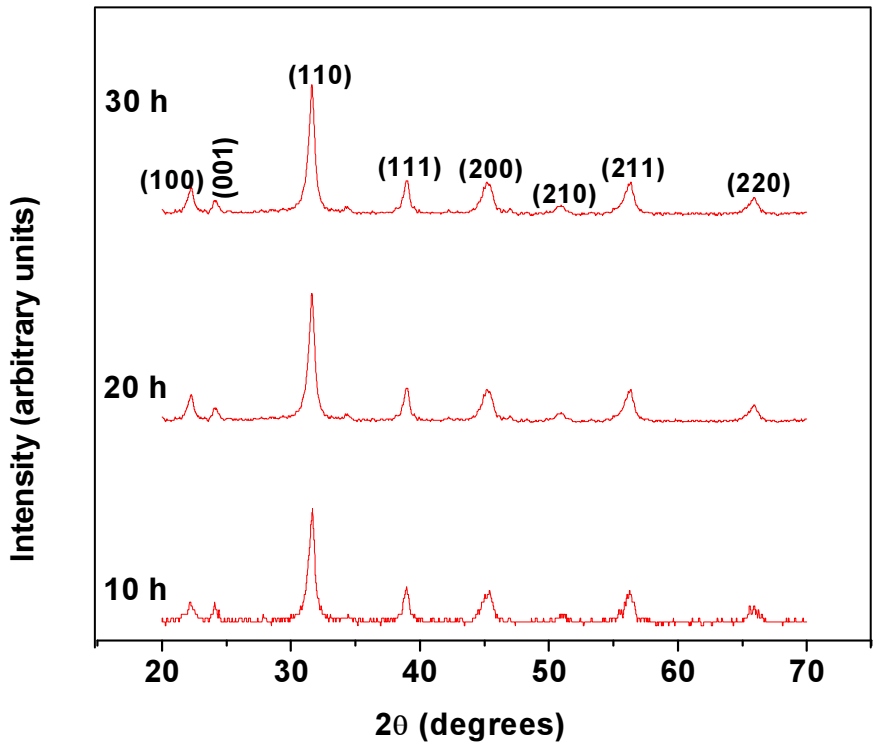

(b)

Fig. 6.13 XRD patterns of the $BaTi_{0.95}W_{0.05}O_3$ (a) before sintering and (b) after sintering

However, in the as milled specimens, even after 30 hours of milling the phase is not formed properly and the specimen require sintering for the proper phase formation. It is observed that after sintering single phase tetragonal structure is formed in samples. The lattice parameters were calculated using the observed interplanar spacing obtained from the diffractograms and refined using the least square refinement method by computer program package Powder-X [51] are given in Table 6.2. The tetragonal strain (c/a) of the compounds was very close to each other, suggesting that the structure of the phase formed is same irrespective of the milling time.

Table 6.2 Various lattice parameters of $BaTi_{0.95}W_{0.05}O_3$ samples milled for different durations

Milling time	a (A^0)	c(A^0)	Volume $(A^0)^3$	c/a
10 h	3.9945	4.0246	64.216	1.0075
20 h	3.9918	4.0213	64.077	1.0073
30 h	3.9915	4.0197	64.042	1.0070

SEM Analysis

Fig. 6.14 shows the SEM images of the specimens milled for different durations. The size of the grains can be seen to be getting reduced with increasing milling time.

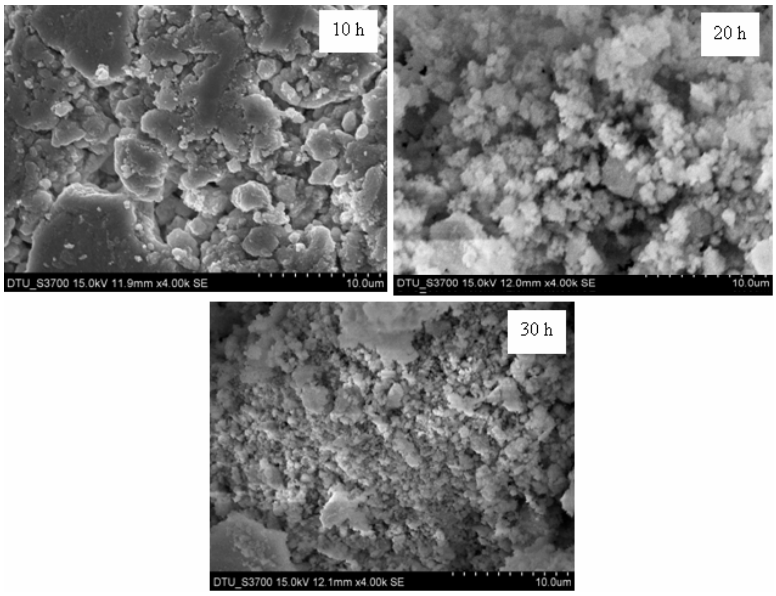

Fig. 6.14 SEM micrographs of pre-sintered $BaTi_{0.95}W_{0.05}O_3$ powders milled for different durations

TEM image and electron diffraction (ED) pattern of the 30 hours milled sample are shown in Fig. 6.15. It is seen that the particles are varying shape and size and connect with each other to form a large network system. The particle size is found in the nanometer range. The formation of particles of nanodimension is also confirmed by diffraction ring consisting of discrete diffraction spots.

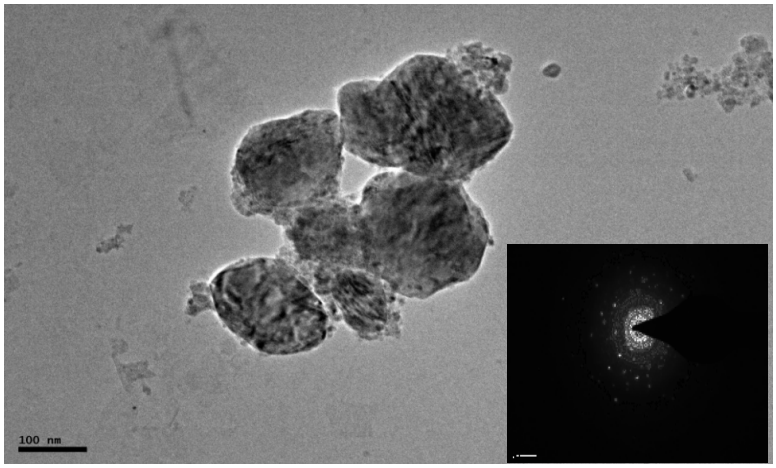

Fig. 6.15 TEM micrograph and electron diffraction pattern of 30 hours milled $BaTi_{0.95}W_{0.05}O_3$ powder

The SEM micrographs of these samples milled for different time are shown in Fig. 6.16. The average grain size of the compound decreases from 0.4-0.2 μm in the samples milled for 10 hours and 20 hours to less than 0.2 μm in the sample milled for 30 hours.

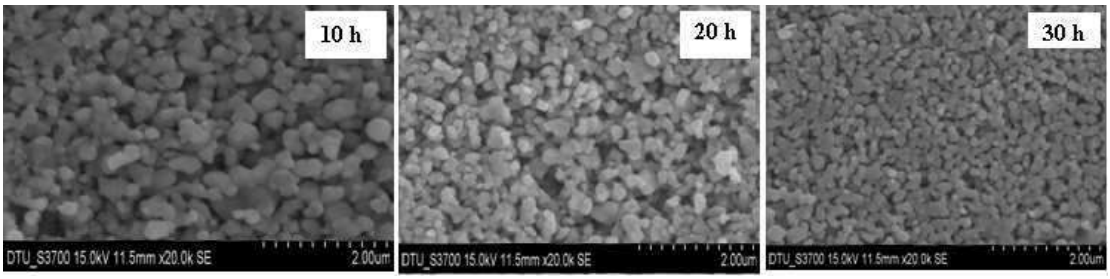

Fig. 6.16 SEM micrographs of $BaTi_{0.95}W_{0.05}O_3$ sintered samples milled for different durations

6.2.4 Electrical Characterization

6.2.4.1 Dielectric Studies

Variation of ε′ with Temperature: Curie Temperature

The temperature dependence of dielectric constant (ε′) measured at 100 Hz, 500 Hz, 1 kHz, 10 kHz and 100 kHz are shown in Fig. 6.17. For all the milling durations, the compound show dielectric anomaly at a temperature called the Curie temperature (T_c).

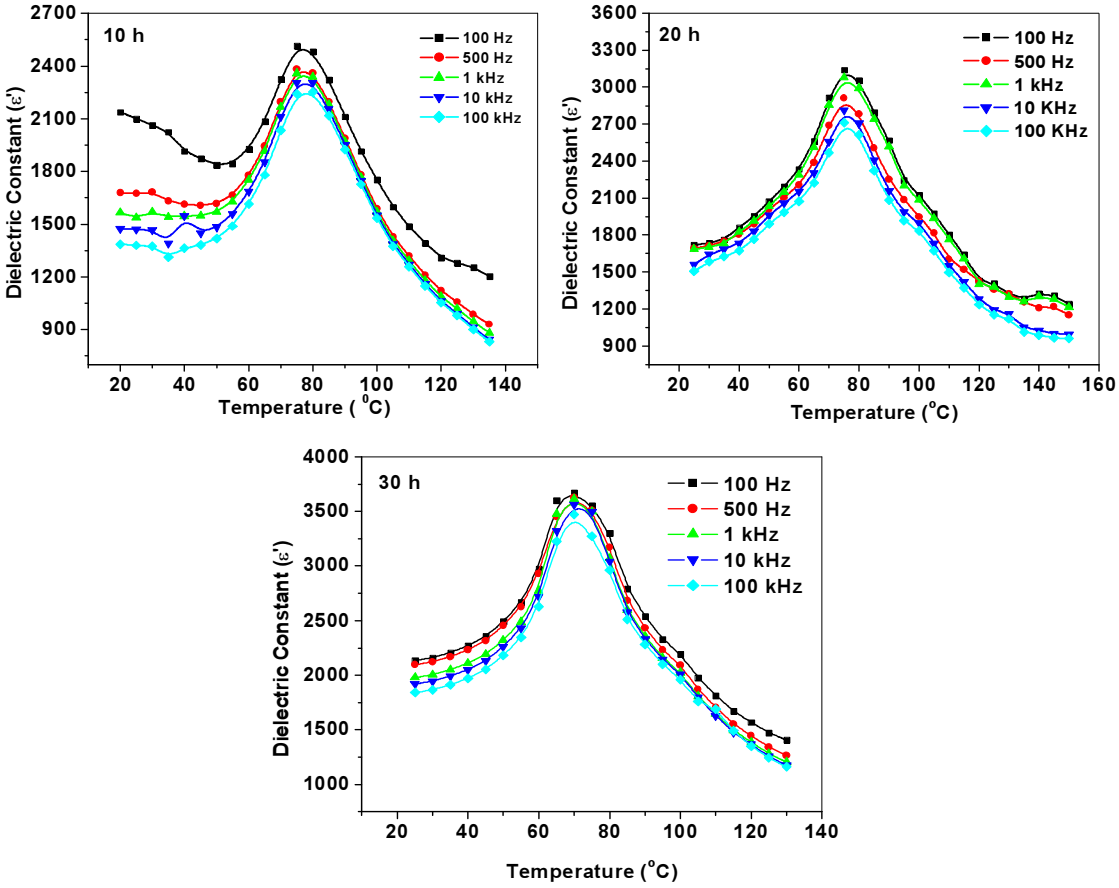

Fig. 6.17 Variation of dielectric constant (ε′) with temperature at different milling durations

Curie temperature remains same at all the frequencies indicating non-relaxor behaviour in the samples. Fig. 6.18 shows the variation of dielectric constant with temperature for different milling duration at a frequency of 1 kHz. It is observed that the dielectric constant value increases with increasing milling time and maximum in the sample milled for 30 hours. It is known that in the fine grained ferroelectric ceramics, ε′ increases due to an increase in residual internal stress [52-56, 59]. The increase in ε′ value is due to the decrease in the average grain size with increase in milling time.

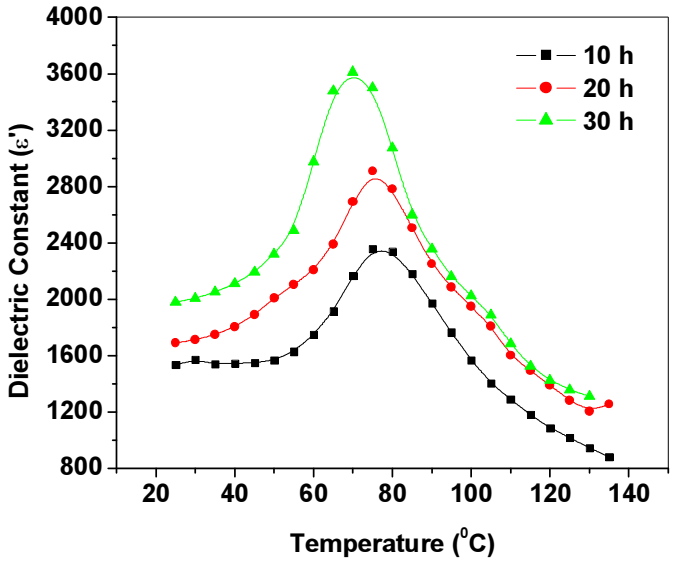

Fig. 6.18 Variation of dielectric constant (ε′) with temperature in $BaTi_{0.95}W_{0.05}O_3$ samples at 1 kHz

The small observed reduction of unit cell volume (Table 6.2) with increase in milling duration may additionally be increasing the dielectric constant as can be followed from Clausis-Mossotti relation:

$$\varepsilon' = \left(\frac{3V_m + 8\pi\alpha_D}{3V_m - 4\pi\alpha_D}\right) = 1 + \left(\frac{12\pi(\alpha_D / V_m)}{3 - 4\pi(\alpha_D / V_m)}\right)$$

where V_m (= $V_{unit\ cell}/Z$) is the molar volume and α_D is the net dielectric polarizability. However, the Curie temperature (T_c) is observed to decrease at higher milling time (Table 6.3). This is due to the decrease in grain size with increasing milling time as it is known that Curie temperature is strongly dependent on the grain size and it decreases significantly even when the grain size decreases by marginal value [56, 60]. Specimen with smaller grains has more interfacial or grain boundary energy as it contains large number of grain boundaries as seen in Fig.6.16. As a result smaller amount of thermal energy is required to undergo the phase transition [61]. Also, there are reports which co-relate the Curie temperature to the tetragonality ratio (c/a) in the specimen [62]. A decrease in tetragonality (Table 6.2) justifies the observed decrease in the Curie temperature in the specimen.

Table 6.3 Dielectric parameters and piezoelectric coefficient of $BaTi_{0.95}W_{0.05}O_3$ samples prepared at different milling time

Milling time	ε'_{max} (1 kHz)	T_c (^{0}C)	d_{33} (pC/N)	Diffusivity (γ)
10 h	2380.66	75	210	1.26
20 h	2964.60	75	227	1.12
30 h	3618.84	70	236	1.14

In the samples, the broad dielectric peaks indicate the diffuse nature of the phase transition. The diffusivity constant or degree of disorderness (γ) has been calculated using the formula:

$$\ln\left(\frac{1}{\varepsilon}-\frac{1}{\varepsilon_{\max}}\right)=\gamma\ln(T-T_c)+const. \qquad (6.2)$$

where ε'_{max} is the maximum value of ε' at $T = T_c$. The values of γ have been calculated from the slope ln $(1/\varepsilon - 1/\varepsilon_{max})$ versus ln $(T- T_c)$ curve (Fig. 6.19) and are given in Table 6.3. For all the samples, γ is found to be between 1 (obeying Curie-Weiss law) and 2 (for completely disordered system) confirming the diffuse phase transition in all the samples.

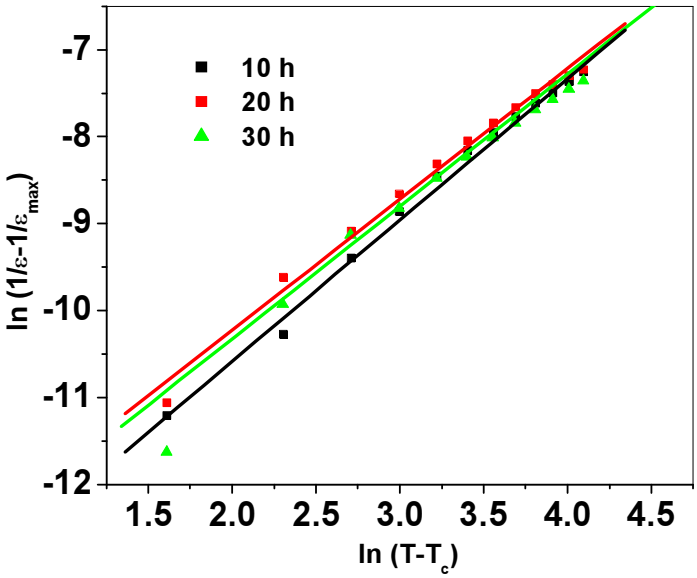

Fig. 6.19 Variation of ln $(1/\varepsilon - 1/\varepsilon_{max})$ with ln $(T- T_c)$

Variation of tan δ with Temperature

Fig. 6.20 shows the temperature variation of dielectric loss (tan δ) at different frequencies of 100 Hz, 500Hz, 1 kHz, 10 kHz and 100 kHz for different milling durations. In the samples, the dielectric loss has smaller values at lower temperatures and at higher temperatures it increases sharply. This sharp increase in dielectric loss at high temperatures may be attributed to the increased mobility of space charges arising from defects or vacancies in the samples [57]. To see the effect of milling duration on temperature variation of dielectric loss, the curves have been plotted in Fig. 6.21 at a frequency 1 kHz. It is observed that dielectric loss is lowest in 30 hour milled specimen compared to lower milling time.

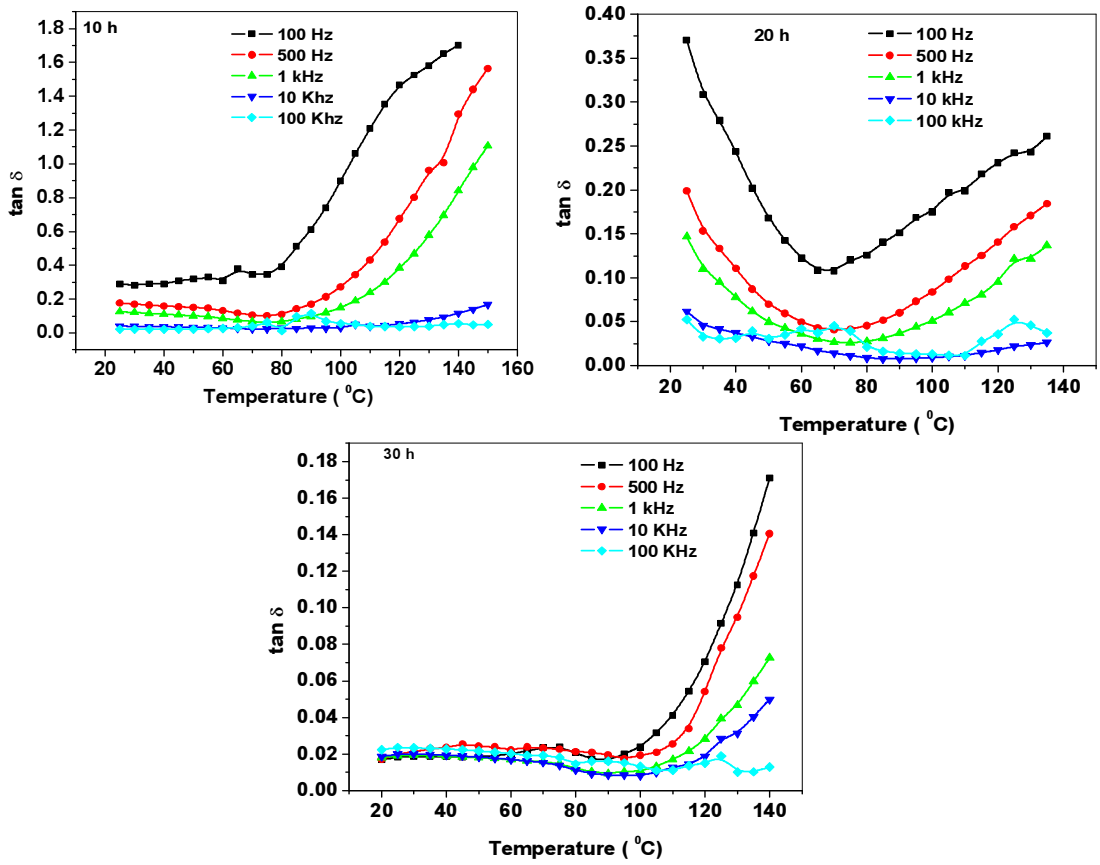

Fig. 6.20 Variation of dielectric loss (tan δ) with temperature

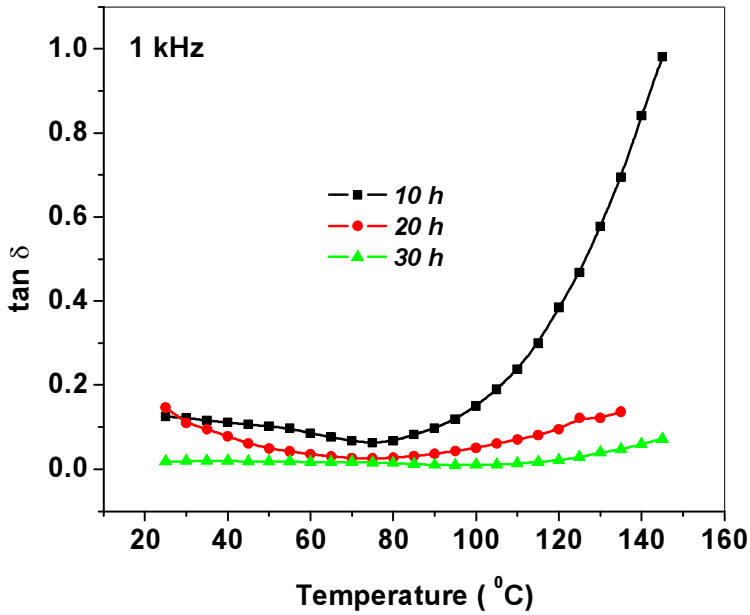

Fig. 6.21 Temperature variation of dielectric loss in the specimens with different milling time

Variation of ε´ and tan δ with Frequency

Fig. 6.22 (a) and (b) shows the variation of dielectric constant and dielectric loss as a function of frequency at room temperature. For all the samples, both dielectric constant and dielectric loss decrease upto 1 kHz and remain nearly constant beyond this frequency. This is due to the fact that at lower frequencies, the dipoles are able to follow the alternating field resulting in higher values of dielectric constant and loss while at higher frequencies the dipoles are unable to follow the rapidly changing field leading to the reduction in the values of dielectric constant and loss. It is worth noting that the room temperature dielectric constant value is highest and room temperature dielectric loss is lowest for the 30 hours milled specimen compared to that in the specimens milled for lower durations.

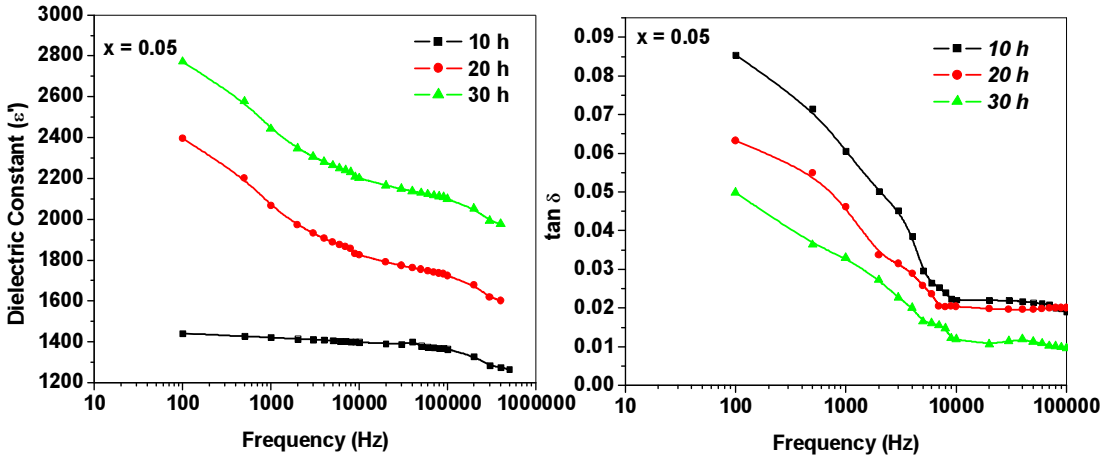

(a) (b)

Fig. 6.22 Variation of (a) dielectric constant (b) dielectric loss with frequency at room temperature

6.2.4.2 Ferroelectric and Piezoelectric Studies

Fig. 6.23 shows the variation of P-E loop of the specimen milled for 30 hours. The observed values of remanent polarization (P_r) and the coercive field (E_c) are 5.206 $\mu C/cm^2$ and 2.84 kV/cm. The higher value of remanent polarization at 30 hours milling time in mechanical activation method as compared to conventional method is possibly due to regular microstructure of sintered specimens with small grain size [58, 63].

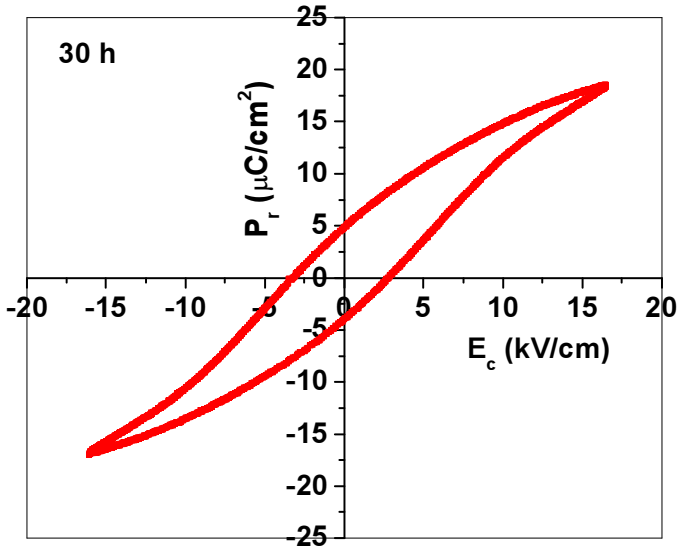

Fig. 6.23 P-E hystersis loop of the studied samples at 30 hours milling time

Piezoelectric coefficients of the studied samples are shown in Table 6.3. The maximum value of piezoelectric coefficient (d_{33}) is observed in the specimen milled for 30 hours.

6.3 Conclusions

Based on the above observations and discussions the following conclusions can be drawn from this chapter

- The synthesized compound has tetragonal structure.
- TEM micrograph reveal that the particles size of specimen milled for 30 hour reduce to nano-range.
- The formation of particles of nanodimensions is also confirmed by diffraction rings consisting of discrete diffraction spots.
- Grain size decrease with increase in milling time in the synthesized specimens.
- The samples milled for higher duration show higher dielectric constant.
- Tetragonal strain as well as volume decreases on increasing milling time.
- Piezoelectric coefficient increases with milling time. The highest value of d_{33} is observed to be 203 pC/N for pure barium titanate milled for 30 hours.
- Dielectric constant as well as loss decrease with increase in frequency, which is a normal behaviour of ferroelectric materials.
- Dielectric loss decreases with increasing milling time in all the samples.
- The highest value of d_{33} is observed to be 236 pC/N for $BaTi_{0.95}W_{0.05}O_3$ compound milled for 30 hours.

References

[1] K. Keizer, E. H. Janssen, K. J. De Vries and A. J. Burggraaf, *Mater. Res. Bull.* **8** (1973) 533.

[2] T. Yamamoto, *Amer. Ceram. Soc. Bull.* **71** (1992) 978.

[3] G. Arlt, *Ferroelectrics*, **104** (1990) 217.

[4] E. R. Camargo, J. Frantti and M. Kakihana, *J. Mater. Chem.* **11** (2001) 1875.

[5] Y. Yoshikawa and K. Tsuzuki, *J. Am. Ceram. Soc*. **75** (1992) 2520.

[6] M. Cerqueira, R.S. Nasar, E. R. Leite, E. Longo and J. A. Varela, *Mater. Lett*. **35** (1998) 166.

[7] E.E. Oren, E. Taspinar, A.C. Tas, *J.Am.Ceram.Soc*. **80** (1997) 2714.

[8] S. Kim, M. Jun and S. Hwang, *J. Am. Ceram. Soc*. **80** (1997) 2714.

[9] J. Tartaj, C. Moure, L. Lascano and P. Duran, *Mater. Res. Bull*. **36** (2001) 2301.

[10] J. B. Blum and S. R. Gurkovich, *J. Mater. Sci*. **20** (1985) 4479.

[11] D.M. Ibrahim and H. W. Henniche, Trans. *J. Am. Ceram. Soc.* **80** (1981) 18.

[12] S. Sato, T. Murakata, H. Yanagi and Miyasaka, *J. Mater. Sci*. **29** (1994) 5657.

[13] J. Moon, T. Li, C. A. Randall and J. H. Adair, *J. Mater. Res*. **12** (1997) 189.

[14] C. R. Peterson and E. B. Slamovich, *J. Am. Ceram. Soc*. **82** (1999) 1702.

[15] A. Wu, P.M. Vilarinho, I. M. Miranda Salvado and J.L. Baptista, *J. Am. Ceram. Soc.* **83** (2000) 1379.

[16] B.G. Muralidharan, A. Sengupta, G.S. Rao and D.C. Agrawal, *J. Mater. Sci.* **30** (1995) 3231.

[17] R. Zimmermann-Chopin and S. Auer, *J. Sol-gel Sci. Technol.* **3** (1994) 101.

[18] D.R. Chen, X. L. Jiao and R. R. Xu, J. *Mater. Sci. Lett*. **17** (1998) 53.

[19] Y. Narenda and G. L. Messing, *J. Am. Ceram. Soc*. **80** (1997) 915.

[20] R. H. Arendt, J. H. Rosolowski and J. W. Szymaszek, *Mater. Res. Bull*. **14** (1979) 703.

[21] C.C. Chiu, C.C. Li and S. B. Desu, *J. Am. Ceram. Soc*. **74** (1991) 38.

[22] J. Z. Jiang, F. W. Poulsen and S. Morup, *J. Mater. Res*. **14** (1999) 1343.

[23] L.B. Kong, J. Ma, W. Zhu and O. K. tan, *J. Alloys comp*. **335** (2002) 290.

[24] R. Janot and D. Guerard, *J. Alloys Comp*. **333** (2002) 302.

[25] M. Zdujic, C. Jovalekic, L. karanovic, M. Mitric, D. Poleti and D. Skala. *Mater. Sci. Eng. A* **245** (1998) 109.

[26] M. Simoneau, G. L. Esperance, J. L. Trudeau and R. Schulz, *J. Mater. Res*. **9** (1994) 535.

[27] Z. Q. Jin, W. Tang, J. R. Zhang, H. Lin and Y. W. Du, *J. Magn. Mater*. **182** (1998) 231.

[28] S. Wang, J. Ding, Y. Shi and Y. J. Chen, *J. magn. Mater*. **219** (2000) 206.

[29] D. J. Fatemi, V. G. Harris, V. M. Browning and J. P. Kirkland, *J. Appl. Phys*. **83** (1998) 6767.

[30] J. M. Xue, D. M. Wan, S. E. Lee and J. Wang, *J. Am. Ceram. Soc*. **82** (1999) 1687.

[31] L. B. Kong, W. Zhu and O. K. Tan, *Mater. Lett*. **42** (2000) 232.

[32] L. B. J. Ma, W. Zhu and O. K. Tan, *J. Alloys Comp*. **322** (2001) 290.

[33] J. Wang, J. M. Xue, D. M. Wan and B. K. Gan, *J. Solid State Chem*. **154** (2000) 321.

[34] X. S. Gao, J. M. Xue, J. Wang, T. Yu and Z. X. Shen, *J. Am. Ceram. Soc*. **85** (2002) 565.

[35] S. K. Ang, J. M. Xue and J. Wang, *J. Alloys Comp* **343** (2002) 156.

[36] L. B. Kong, J. Ma, H. Huang and R. F. Zhang, *Mater. Res. Bull*. **37** (2002) 1085.

[37] L. B. Kong, J. Ma, H. Huang, R, F. Zhang and W. X. Que, *J. Alloys Comp*. **337** (2002) 226.

[38] L. B. Kong, J. Ma, W. Zhu and O. K. Tan, *Mater. Lett*. **51** (2001)108.

[39] K. Shantha and K. B.R. Varma, *J. Am. Ceram. Soc.* **83** (2000) 1122.

[40] A. Castro, P. Millan, J. Ricato, L. Pardo, *J. Mater Chem*, **10** (2000) 767-71.

[41] C. H. Lu and C. H. Wu, *J. Eur. Ceram. Soc*. **22** (2002) 707.

[42] J. M. Xue, J. Wang, D. M. Wang, *J. Am Ceram. Soc*. **83** 1 (2000) 232-4.

[43] O. Abe, Y. Suzuki, *Mater Sci. Forum*, **225** (1996) 563-8.

[44] L. B. Kong, J. Ma, H. Huang, R.F. Zhang, W.X. Que, *J. Alloys and compound* **337** (2002) 226-30.

[45] V. Berbenni, A. Marini, G. Bruni, *Thermochim Acta* **374** (2001) 151-8.

[46] A. Castro, P. Begue, B. Jimenez, J. Rictoe, R. Jimenez, *J. Phys. Chem Mater*, **15** (2003) 3395-401.

[47] A. Castro, P. Millan, L. Pardo, B. Jimenez, *J. Mater Chem*, **9** (1999) 1313-7.

[48] J. Ricote, L. Pardo, A. Moure, A. Castro, P. Millan, D. Chateigner, *J. Eur Ceram Soc*, **21** (2001) 1403-7.

[49] B. Jimenez, A. Castro, L. Pardo, P. Millan, R. Jimenez, *J. Phys Chem Solids* **62** (2001) 951-8.

[50] L. Pardo, A. Castro, P. Millan, C. Alemany, R. Jimenez, B. Jimenez, *Acta Mater*. **48** (2000) 2421-8.

[51] C. Dong, *J. Appl. Cryst*.**32** (1999) 838.

[52] W. R. Busessem, L. E. Cross and A. K. Goswami, *J. Am. Ceramic. Soc*. **49** 133-6 (1996).

[53] G. Arlt, D. Hennings and G. De With, *J. Appl. Phys*, **58** 4 (1985) 1691-25.

[54] W. Kanzig, *Phys. Rev* **98** 2 (1955) 549-50.

[55] K. Uchino, E. Sadanago and T. Hirose, *J. Am. Soc*. **72** 8 (1989) 1555-8.

[56] S. K. S. Prashar, R. N. P. Choudhary, B. S. Murthy, *J. Appl. Phys*. **94** (2003) 6091.

[57] T. Friessings, S. Aggarwal, R. Ramesh, B. Nilesen, E. H. Poindexter and D. J. Keeble, *Appl. Phys. Lett*. **77** (2000) 127.

[58] R. Koduri and M. Lopez, *Ferroelectric Lett.* **34** (2007) 113.

[59] G. Li, L. Zheng, Q. Yin, B. Jiang and W. Cao, *J. Appl. Phys*. 98 (2005) 064108-1

[60] B. Praveen Kumar, G. Sreenivasalu, H. H. Kumar, D. K. Kharat, M. Balasubramanian, B. S. Murthy, *Materials Chemistry and Physics* **117** (2009) 338-42.

[61] S. K. S. Parashar, R. N. P. Choudhary and B. S. Murthy, *Journal of Applied Physics*, **98** (2005) 104305.

[62] B. A. Marinkoviae, B. D. Stojanoviæ1, V. B. Pavloviae, V. P. Pavloviae, M. M. Ristiae *Materials Structure*, **6**(1999) 2

[63] B. D. Stojanovic, C. Jovalekic, V. Vukotic, A. Z. Simoes, J. A. Varela, *Ferroelectrics* **319** (2005) 65-73.

Physica B 404 (2009) 4290–4294

Contents lists available at ScienceDirect

Physica B

journal homepage: www.elsevier.com/locate/physb

Phase transitions and electrical characteristics of tungsten substituted barium titanate

Sheela Devi, A.K. Jha *

Department of Applied Physics, Delhi College of Engineering, Faculty of Technology, University of Delhi, Delhi 110042, India

ARTICLE INFO

Article history:
Received 27 April 2009
Received in revised form
23 July 2009
Accepted 3 August 2009

Keywords:
Ferroelectrics
Dielectric response
Phase transitions

ABSTRACT

In the present work, phase transitions and electrical characteristics of tungsten substituted barium titanate are reported. Structural analysis of the prepared samples was carried out to confirm the formation of the compounds in proper phase. Scanning electron micrographs of the compounds have been used to investigate the grain morphology of the material. The dielectric properties of the samples have been studied as a function of temperature and frequency. The variation of dielectric constant (ε_r) with temperature shows a diffuse kind of ferro–paraelectric phase transition. The diffusitivity of the phase transitions has been calculated. Complex impedance spectroscopy analysis was carried out to investigate the electrical characteristics of the specimen.

1. Introduction

Since the discovery of barium titanate ($BaTiO_3$) in the early 1940s, this material has been used for a wide range of industrial and scientific applications such as capacitors, ultrasonic transducers, pyroelectric infrared sensors, positive temperature coefficient (PTC) resistors, etc. [1–4]. Being a lead free ferroelectric material, it is a good substitute for Pb containing compounds for various applications. It is a typical ferroelectric material with Curie temperature in the range of 120–130 °C [5]. $BaTiO_3$ has a perovskite (ABO_3) tetragonal structure at room temperature.

Substitutions at both A- and B-sites have been used to modify the electrical and dielectric properties of $BaTiO_3$ [6]. It is well established that the dielectric properties of ceramics depend not only on the nature and amount of dopants, but also on the different processing factors [7]. The substitution of tungsten has been found to be effective in enhancing the dielectric properties of ferroelectric materials [8–10]. However, not much work has been reported on the B-site substitution in barium titanate and there is hardly any extensive report in the literature on the tungsten substitution at B (Ti) site in this material. This prompted the authors to investigate the structural, dielectric and electrical characteristics of tungsten substituted barium titanate.

2. Experimental

Samples of compositions Ba $(Ti_{1-x}W_x)$ O_3; $x = 0.0$, 0.05, 0.15 and 0.30, were prepared using solid-state reaction technique taking $BaCO_3$, TiO_2 and WO_3 (all from Aldrich of 99.9% purity) in stoichiometric proportions. The powders were thoroughly mixed, ground and passed through sieve of appropriate size. Mixtures were calcined at 1150 °C for 2 h in air. The calcined specimens were mixed with appropriate quantity of polyvinyl alcohol and molded into disc shape pellets by applying a pressure of 300 MPa. The pellets were then sintered at 1250 °C for 2 h.

X-ray diffractograms of the sintered samples were recorded on a Philips X-ray diffractometer using Cu-K_α radiations ($\lambda = 1.5405$ Å) in the range $20° \leq 2\theta \leq 70°$ at a scanning rate of 0.02°/s. The sintered pellets were polished to a thickness of 1 mm, coated with silver paste on both sides for the use as electrodes and finally cured at 300 °C for 15 min. Scanning electron micrographs of the samples were recorded using Cambridge Stereo Scan 360 microscope. The dielectric parameters were measured from 100 Hz to 1 MHz on an Agilent 4284A LCR meter at oscillation amplitude of 1 V while the impedance measurements were carried out in the frequency range of $10–10^6$ Hz.

3. Results and discussions

3.1. Structural analysis

Fig. 1 shows the XRD patterns of the studied samples. It is observed that a perovskite structure is formed in all the samples.

* Corresponding author. Tel.: +91 9868242150; fax: +91 11 27871023.
E-mail address: dr_jha_ak@yahoo.co.in (A.K. Jha).

0921-4526/$ - see front matter © 2009 Elsevier B.V. All rights reserved.
doi:10.1016/j.physb.2009.08.064

Lattice parameters were calculated from the X-ray diffractogram and refined using least square refinement method by a computer-programme package Powder-X [11]. The calculated lattice parameters were used to find the unit cell volume and tetragonal strain (c/a) of the specimens. It is observed that there is a marginal decrease in tetragonal strain on the substitution of tungsten (Table 1). On the basis of ionic radii of atoms and co-ordination number [12] it is expected that the tungsten ions will occupy titanium (B) sites. Also, due to the smaller ionic radius of W^{6+} (0.60 Å) than that of Ti^{4+} (0.68 Å), a decrease in lattice constant is expected. Lattice parameters (Table 1) are indeed observed to decrease with increasing tungsten content, confirming the occupation of W^{6+} ions onto the Ti^{4+} sites.

In the X-ray diffractograms, the splitting of (0 0 2) and (2 0 0), (1 0 2) and (2 0 1), and (1 1 2) and (2 1 1) tetragonal peaks are observed at $2\theta = 43.97^\circ$ and 44.83°, 49.69° and 50.33° and 54.95° and 55.45°, respectively, which is indicative of the fact that all the compositions possess tetragonal structure [13]. The particle size (P) of the specimens were calculated using few selected strong peaks at different Bragg angles using Scherer's formula [14]:

$$P = K\lambda/\beta_{1/2}\cos\theta$$

where $K = 0.89$ and $\beta_{1/2}$ is the half peak width. The peak in the lower angle region was chosen for this purpose to avoid strain broadening. The calculated average particle size of the specimen is given in Table 2.

Fig. 2 shows the SEM micrographs of the studied samples. It is observed that the grains are homogeneously and uniformly distributed. The average grain size, determined by the linear intercept method, increases on tungsten substitution; the grain size increases upto ~3 μm in the sample with $x = 0.3$. It is well known that the composition influences the microstructure such as grain growth and densification which in turn control other properties of the material [15,16]. As seen in Fig. 2, tungsten substitution promotes grain growth and bigger grains are formed.

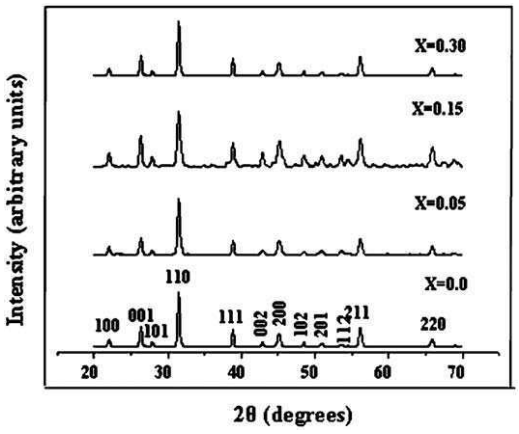

Fig. 1. XRD pattern of the studied samples.

3.2. Dielectric properties

Fig. 3 shows the variation of dielectric constant as a function of temperature at a frequency of 100 kHz. In the tungsten free sample, there is a sharp transition in the dielectric constant at Curie temperature T_c, where the dielectric constant is maximum. Diffuse kind of ferro–para phase transition is observed in the tungsten substituted samples with the phase transitions getting broader with increasing tungsten concentration. Further, it is observed that the Curie temperature decreases from 120 °C ($x = 0.0$) to 75 °C ($x = 0.05$) on tungsten substitution. However, as the concentration of tungsten is increased to $x = 0.30$, the Curie temperature again increases to 85 °C. The observed reduction in T_c and its subsequent increase can be understood as follows. It is known that when a higher valent ion replaces titanium, this leads

Table 2
Grain resistance, grain boundary resistance and particle size.

Composition	Temperature (°C)	R_g (kΩ)	R_{gb} (kΩ)	Particle size (nm)
$x = 0.0$	325	50	–	21.89
	345	18		
	365	9.5		
$x = 0.05$	325	250	–	21.17
	345	210		
	365	45		
$x = 0.15$	325	885	–	22.48
	345	420		
	365	142	160	
$x = 0.30$	325	1450	–	22.99
	345	900		
	365	240	165	

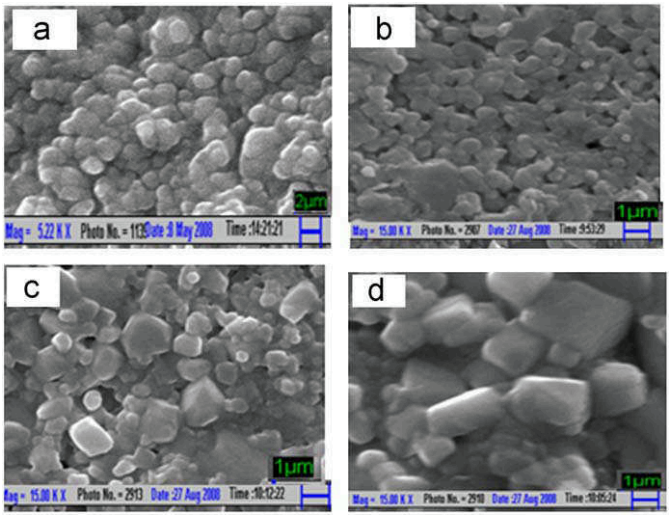

Fig. 2. SEM micrograph of the studied samples.

Table 1
Lattice parameters, volume, ionic radii, co-ordination number, dielectric constant, Curie temperature and diffusivity.

Composition	a (Å)	c (Å)	c/a	Volume (Å)^3	Ionic radii	CN	ε_r	T_C (°C)	Diffusivity (γ)
$x = 0.0$	3.999	4.038	1.009	64.575	$Ti^{4+} = 0.68$	6	1667.48	120	
$x = 0.05$	3.996	4.025	1.007	64.271	$W^{6+} = 0.60$	6	1759.17	75	1.26
$x = 0.15$	3.994	4.019	1.006	64.111			2025.83	80	1.59
$x = 0.30$	3.989	4.010	1.005	63.807			2281.37	85	1.74

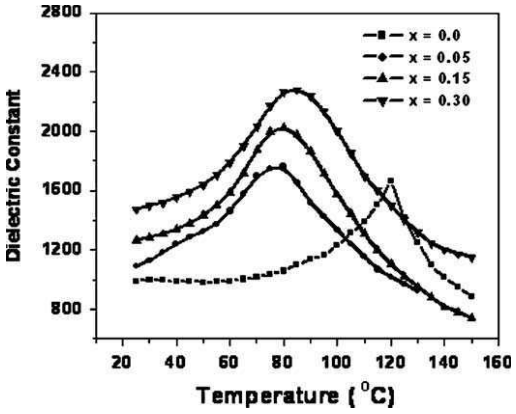

Fig. 3. Dielectric constant vs. temperature at different composition.

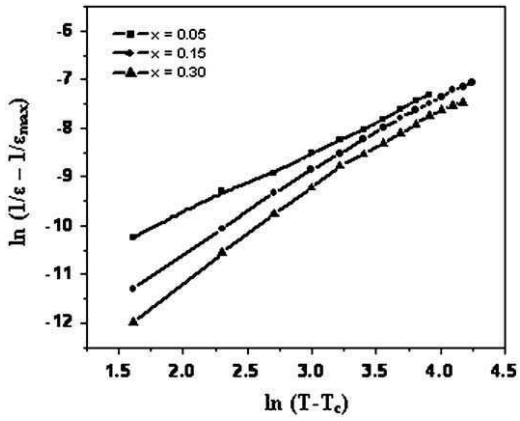

Fig. 4. Variation of $\ln(1/\varepsilon - 1/\varepsilon_{max})$ with $\ln(T-T_c)$ at 100 kHz.

to a decrease in the bonding force between tungsten and oxygen atoms [17]. This decrease in the bond energy leads to lesser distortion of the octahedron resulting in a decreased c/a ratio which is responsible for the reduction in Curie temperature. However, for higher concentration of tungsten, a shift in T_c to higher temperature and the corresponding increase in peak dielectric constant of tungsten are also observed. In perovskite ferroelectrics, substitution at B-site (located inside an oxygen octahedron) and the observed increase in dielectric constant and Curie temperature owing to larger polarization can be well explained by the enlarged "rattling space" available to the smaller B-site ions [18,19]. Further, it is known [20] that the substitution of tungsten introduces cation vacancies at B-site, which possibly lead to an enhancement of ferroelectric structural distortion and an eventual increase in T_c. The increase in dielectric constant indicates enchanced polarizabilty due to increased rattling space. Another possible reason for the increase in dielectric constant is that these cation vacancies make the domain motion easier and increase the dielectric permittivity [21,22]. This can also be understood in terms of larger grains in the sample containing higher concentration of tungsten as observed in the SEM micrographs (Fig. 2). It is known that the domain walls are comparatively free in the larger grains resulting in higher polarization. It is reasonable to believe that the observed variations in dielectric constant and T_c are due to the cumulative effect of all the above mentioned causes.

The quantitative evaluation of the diffusivity or disorderness in a specimen can be made using the expression [23]

$$\ln(1/\varepsilon - 1/\varepsilon_{max}) = \gamma \ln(T - T_c) + \text{constant}$$

where γ is a measure of diffusivity or disorderness of the ferroelectric to paraelectric phase transition and ε_{max} is the maximum dielectric constant. The variation of $\ln(1/\varepsilon - 1/\varepsilon_{max})$ versus $\ln(T-T_c)$ (at 100 kHz) is shown in Fig. 4 and the calculated value of γ is given in Table 1. It is found that γ lies between 1 (normal Curie–Weiss behavior) and 2 (for completely disordered system) confirming the diffuse type phase transitions in the specimens, as indeed observed [24]. The observed value of γ increases with increase in the tungsten content of the sample. This observation is in conformity with the observed phase transitions in Fig. 3.

Fig. 5 shows the variation of dielectric loss (at 100 kHz) as a function of temperature. It is observed that the loss initially remains largely independent of temperature up to nearly 90 °C and thereafter it increases with the increase in temperature. Further, it is observed that the loss increases more rapidly in the tungsten containing samples than that in the tungsten free

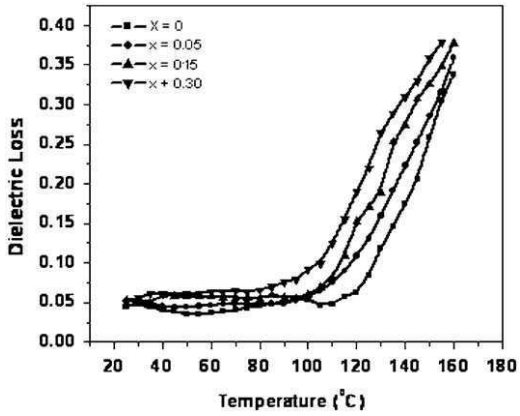

Fig. 5. Dielectric loss vs. temperature at different composition.

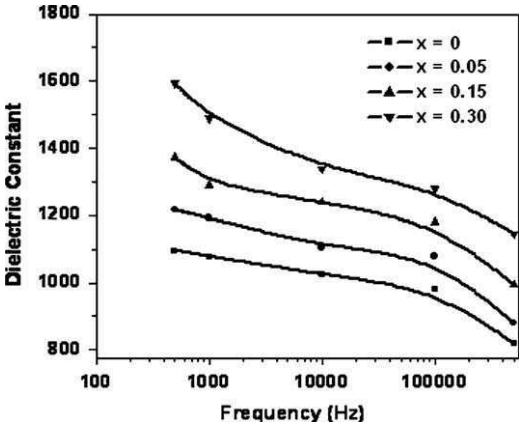

Fig. 6. Dielectric constant vs. frequency at different composition.

sample. The observed variation of dielectric loss can be understood as follows. As discussed earlier, the substitution of W^{6+} for Ti^{4+} results in the formation of cation vacancies, leading to the soft characteristics in the material [25]. In the soft materials, large loss occurs due to the domain boundary vibrations or excitations that are readily stimulated under the weak a.c. drive conditions [13].

Fig. 6 shows the variation of dielectric constant (ε_r) as a function of frequency, in the frequency range 100 Hz–1 MHz at room temperature. As the frequency increases, the dielectric constant is observed to decrease in all the samples, which is a

normal behavior of these materials [26]. The decrease is rapid at lower frequencies and become slower at higher frequencies. This phenomenon is due to the frequency dispersion [27]. Upto a frequency of around 1 kHz the decrease in dielectric constant is due to the reduction of the space charge polarization. At the higher frequencies the dipoles are unable to follow the variation of the applied a.c. electric field, resulting in the reduction of dipolar polarization and the consequent decrease in dielectric constant. It is further observed in Fig. 6, that the dielectric constant of higher tungsten containing sample is larger and it also decreases with frequency more rapidly. This is indicative of the formation of larger number of space charge, i.e., cation vacancies, in the sample with higher tungsten content confirming the earlier observations.

Fig. 7 shows the variation of dielectric loss with frequency at room temperature. It is observed that with the increasing frequency the dielectric loss decreases. In the dielectric materials, cation vacancies formation, lattice distortion, etc. produce an absorption current resulting in loss. Also, with the increase in frequency of the applied field, the dipoles are unable to follow the rapidly oscillating field leading to the reduction in the loss. Further, as observed in Fig. 7, dielectric loss is higher in the sample with higher tungsten content and the decrease in the loss is rapid with the increasing frequency. This can be understood in terms of the presence of the increased space charges i.e. cation vacancies, and their inability to follow the high frequency a.c. field in these samples.

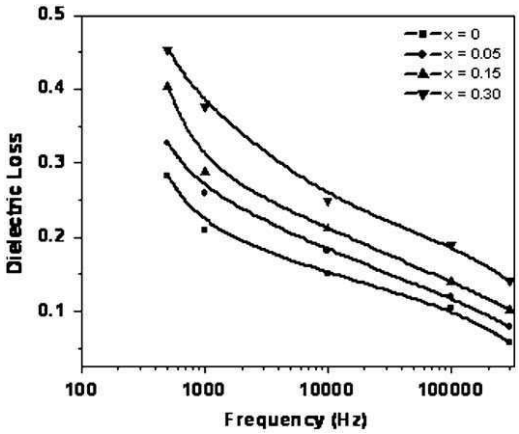

Fig. 7. Dielectric loss vs. frequency at different composition.

4. Impedance analysis

Complex impedance spectroscopy (CIS) is a well-known and powerful technique for investigating the electrical characteristics of the materials [28]. This technique enables us to evaluate and separate the contributions due to various components such as bulk, grain boundaries or interface phenomenon to the overall electrical property of material [29]. It is based on the principle of analyzing the response of a sample to a sinusoidal electrical signal and the subsequent calculation of the resulting impedance with respect to the frequency of the applied signal.

Fig. 8 shows the complex impedance plots of the $BaTi_{1-x}W_xO_3$ ceramics for different concentrations of tungsten at 325, 345, and 365 °C. The impedance spectra are characterized by the appearance of semicircular arcs, with some degree of decentralization (i.e., having their centers below the real axis). This decentralization or non-Debye type relaxation obeys the Cole–Cole formalism [30], where the depressed semicircle represents typically a relaxation phenomena with a spread of relaxation time. The Z'–Z'' plots of the substituted samples at small tungsten concentration are dominated by a single semicircle which represents the impedance contribution of the grains. However, at higher temperature (365 °C) and higher concentration of tungsten, the contribution from grain boundaries is also significant (Table 2). This is indicated by the presence of two semicircles, exhibiting both grain (bulk property) and grain boundary effects. The high frequency semicircle corresponds to grain contribution, and the low frequency semicircle corresponds to the grain boundary effect (magnified view given in the inset) [31]. The calculated values of R_b and R_{gb} of

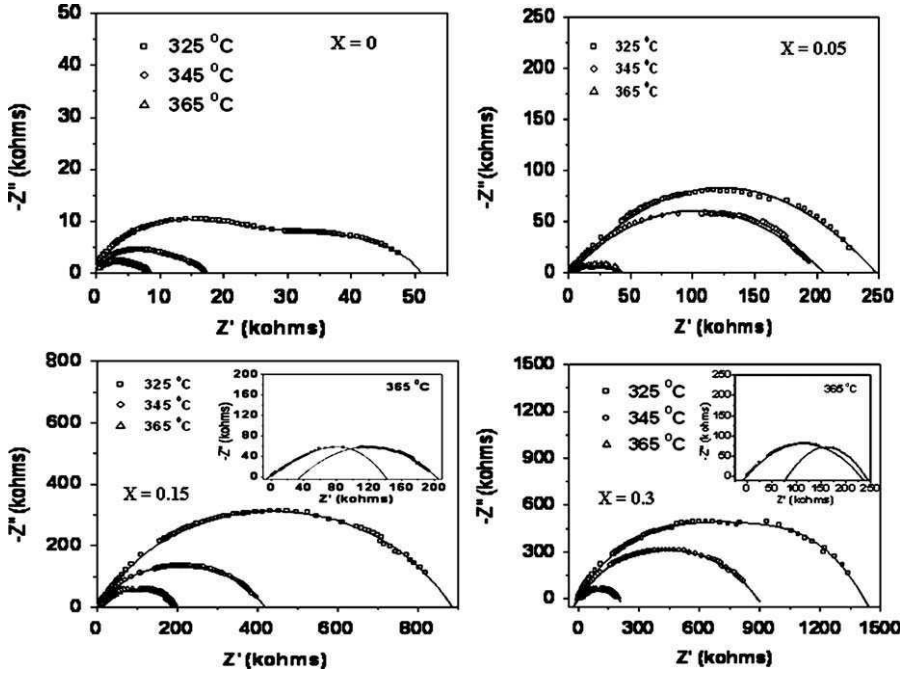

Fig. 8. Plot of real part of impedance (Z') with imaginary part of the impedance (Z'') of BTW ($x = 0$, 0.05, 0.15, 0.30), in inset the magnified view of Z' vs. Z'' at 365 °C.

the samples are given in Table 2. The value of bulk resistance R_b was calculated from the high frequency intercept of the semicircle on the real axis.

It is also observed that with the increase in tungsten concentration, the bulk resistance increases. The oxygen vacancies are considered to be the most mobile ionic charge carriers in the perovskite oxides [32]. In the W-containing samples the substitution of W^{6+} onto Ti^{4+} sites is accompanied by the formation of cation vacancies and subsequent elimination of oxygen vacancies. It is the decrease in the concentration of the oxygen vacancies that a decrease in conductivity with increasing concentration of tungsten is observed.

5. Conclusions

The X-ray diffractograms confirm the formation of the materials with tetragonal structure. Unit cell volume and tetragonal strain decrease with the increase in the tungsten content of the sample. Curie temperature decreases on tungsten substitution but it again increases on increasing the tungsten content. The peak dielectric constant is found to increase on tungsten substitution and the compounds show diffuse kind of ferro–para phase transitions with the diffusivity increasing with the increasing tungsten content. The dielectric constant as well as loss decreases with the increase of frequency. At higher temperature and W-content the grain boundary contribution to the overall impedance becomes significant. Substitution of tungsten is found to be effective in eliminating oxygen vacancies which decreases the conductivity of the studied samples.

Acknowledgment

The authors are thankful to All India Council for Technical Education, New Delhi, for the grant of a research project.

References

[1] G.H. Haertling, J. Amer. Ceram. Soc. 82 (1999) 797.
[2] R.E. Jones, P.D. Mainar, J.O. Olowolafe, J.O. Campbell, C.J. Mogab, Appl. Phys. Lett. 60 (1992) 1022.
[3] M.H. Frey, D.A. Payne, Appl. Phys. Lett. 63 (1963) 2753.
[4] H. Hu, S.B. Krupanidhi, J. Appl. Phys. 74 (1993) 3373.
[5] W. Kanzig, Ferroelectricity 74 (1987) 285.
[6] R. Farhi, M. El Marssi, A. Simon, J. Ravez, J. Eur. Phys. B 18 (2000) 605.
[7] H. Shi, Y. Lin, T. Ao-Tang, Solid State Commun. 135 (2005) 304.
[8] Y. Wu, S.J. Limmer, T.P. Chou, C. Nguyen, J. Mater. Sci. Lett. 21 (2002) 947.
[9] X. Zong, Z. Yang, H. Li, M. Yuan, Mater. Res. Bull. 41 (2006) 1447.
[10] I. Coondoo, A.K. Jha, S.K. Agarwal, J. Eur. Ceram. Soc. 27 (2007) 253.
[11] C. Dong, J. Appl. Crystallogr. 32 (1999) 838.
[12] R.D. Shannon, C.T. Prewitt, Acta Crystallogr. B 25 (1969) 925.
[13] X. Zong, Z. Yang, H. Li, M. Yuan, Mater. Res. Bull. 41 (2006) 1447.
[14] P. Scherrer, Gottin Nachr. 2 (1918) 98.
[15] T. Atsuki, N. Soyama, T. Yonezawa, K. Ogi, Japan J. Appl. Phys. 34 (1995) 5096.
[16] M. Noda, Y. Matsumuro, H. Sugiyama, M. Okuyama, Japan J. Appl. Phys. 38 (1999) 2275.
[17] C. Wanqiang, J. Xiong, S. Juanpin, Mater. Chem. Phys. 106 (2–3) (2007) 338.
[18] I. Coondoo, A.K. Jha, S.K. Agarwal, Ceram. Internat. 33 (2007) 41.
[19] K. Singh, D.K. Bopardikar, D.V. Atkare, Ferroelectric 82 (1988) 55.
[20] N. Zhong, X.-L. Dong, D.-Z. Sun, P.-h. Xiang, H. Du, Mater. Res. Bull. 39 (2004) 175.
[21] Y. Wu, S.J. Limmer, T.P. Chou, C. Nguyen, J. Mater. Sci. Lett. 21 (2002) 947.
[22] S. Takahashi, M. Takahashi, Japan J. Appl. Phys. 11 (1972) 31.
[23] S.M. Pilgrim, A.E. Sutherland, S.R. Winzer, J. Amer. Ceram. Soc. 73 (1990) 3122.
[24] J. Daniels, K.H. Harlet, R. Wernicke, Philips Res. Rep. 36 (1976) 487.
[25] N. Zhong, X.-L. Dong, D.-Z. Sun, P.-h. Xiang, H. Du, Mater. Res. Bull. 39 (2004) 175.
[26] M.E. Lines, A.M. Glass, Principle and Applications of Ferroelectric Materials, Oxford Clarendon Press, New York, 1997.
[27] M. Golio, The RF and Microwave Hand book, CRC Press, Boca Raton, 2001.
[28] J.R. MacDonald, Impedance Spectroscopy, Wiley, New York, 1987.
[29] T.C. Chen, C.L. Thio, S.B. Desu, J. Mater. Res. 12 (1997) 2628.
[30] M.A.L. Nobre, S. Lanfredi, J. Phys. Chem. Solids 64 (2003) 2457.
[31] B. Behera, P. Nayak, R.N.P. Choudhary, J. Alloys Comp. 436 (2007) 226.
[32] D.M. Smyth, Ferroelectrics 117 (1991) 117.

Structural and Electrical Investigations of Tungsten Substituted Barium (Strontium) Titanate Ferroelectric Ceramics

A thesis submitted

by

Sheela Devi

in fulfillment of the requirements
for the award of the degree of

Doctor of Philosophy

to

University of Delhi
Delhi, India

Chapter 7

Chapter 7

Conclusions & Suggestions for Future Work

7.1 Conclusions

In this chapter, a recapitulation of the main results in the present work has been summarized and conclusions have been drawn. Also, the perspectives for the future work, in the context of the present work, have been put forth.

The effects of tungsten substitution in barium titanate and barium strontium titanate have been studied in the present work. Nanocrystalline barium titanate and $BaTi_{0.95}W_{0.05}O_3$ were prepared by high-energy ball milling technique and their properties have been investigated.

Firstly, the processing conditions, i.e., calcinations and sintering temperatures and rate of heating were optimized. It was found that the optimized rate of heating and sintering condition for $BaTi_{0.85}W_{0.15}O_3$ compound is 8 ^{o}C/min and 1250 ^{0}C for 2 hours. The synthesized compound at this optimum preparation condition has tetragonal pervoskite structure at room temperature. Scanning electron micrographs indicate that average grain size increases up to 2μm and at higher sintering temperature and duration partial melting of specimen takes place. The compound shows the diffuse type of ferroelectric-paraelectric phase transition in the samples. Curie temperature remains the same at all the frequencies indicating non-relaxor behavior in all the specimens. Curie temperature decreases in tungsten substituted samples as compared to tungsten free sample. The compound shows the positive

temperature coefficient of resistance (PTCR) behaviour and resistivity increases sharply around at Curie temperature in all the samples. The remanent polarization (P_r) value and Coercive field (E_c) of the sample at optimized sintering condition is 1.80 $\mu C/cm^2$ and 2.20 kV/cm. When the temperature approaches the Curie temperature the remanent polarization decreases and finally the ferroelectric phase disappear. The maximum value of piezoelectric coefficient (d_{33}) in the specimen sintered at 1250 ^oC for 2 hours is 112.48 pC/N.

A series of specimens with substitutions of tungsten at titanium site in barium titanate was prepared at optimized sintering conditions and their structural and electrical properties have been investigated. Single phase pervoskite tetragonal structure is formed for the entire concentration range of the substituent. The lattice parameters and tetragonal strain decrease with increase in tungsten concentration. Scanning electron micrographs reveal that W addition in barium titanate is effective in improving the microstructure and large grains are observed. The average grain size increase upto ~ 3μm. Substitution of the smaller W^{6+} ions for Ti^{4+} ions in barium titanate is found to be effective in improving the dielectric constant. Curie temperature decrease on tungsten substitution but it again increases on increasing the tungsten content. The peak dielectric constant is found to increase on tungsten substitution. The compounds show diffuse ferroelectric-paraelectric phase transitions with the diffusivity increasing with the increasing tungsten content. Dielectric constant as well as the loss decrease with the increase of frequency, which is a normal behavior of all dielectric materials. In Cole-Cole (Nyquist) plots, at higher temperature and at higher W-content the grain boundary contribution to the overall impedance becomes significant. Tungsten substituted barium titanate show PTCR

behavior. Substitution of tungsten is found to be effective in eliminating oxygen vacancies which decreases the conductivity of the studied samples. Polarization-Electric field hysteresis loop confirms the ferroelectric nature of the synthesized material at room temperature and remanent polarization increases with increases in tungsten content. The d_{33} value is observed to increase with increasing W content up to x = 0.15. The observed behaviour have been explained in terms of the microstructural features and the contribution from the inherent defects (oxygen vacancies) and cationic vacancies in W- substituted barium titanate.

W-substituted barium strontium titanate specimens were also prepared and studied. Single phase pervoskite structure is maintained up to tungsten concentration x $\leq$ 0.05. For higher W content, an unidentified peak is observed and intensity of this peak increases with W concentration. Lattice parameters, unit cell volume and tetragonal strain decrease with increasing tungsten content. The Curie temperature reduces from 347 K to 295 K on tungsten substitution. For low W content not much change is observed in granular distribution. At higher W concentration, it is observed that interdiffusion of grains takes place and the boundaries of the grains are not so sharp. The average observed grain size is found to be in the range of 0.5 to 1.5 μm. Curie temperature remains the same at all the frequencies indicating non-relaxor behaviour and all the compounds exhibit ferroelectric-paraelectric diffuse phase transition. Dielectric constant as well as loss decreases with increase in frequency. Dielectric constant increases for low concentration (x = 0.05) of W substitution and reduces for higher concentrations. The dielectric loss reduces significantly on tungsten substitution. W substitution enhances the remanent polarization of the specimen and the maximum observed value of remanent polarization is 2.93 $\mu C/cm^2$.

Substitution of tungsten is found to be effective in eliminating oxygen vacancies which decreases the conductivity of the studied samples. Nearly equal values of activation energies, calculated from relaxation time and conductivity curves, suggest that the relaxation and conduction processes may be attributed to the same type of charge carriers, i. e., and oxygen vacancies.

Mechanical activation process (i.e, high- energy ball milling) has successfully been used to synthesize nanocrystalline barium titanate and $BaTi_{0.95}W_{0.05}O_3$ ferroelectric ceramics. This process skips the high energy consuming calcination step, making the preparation process simpler than the conventional technique. Dielectric, ferroelectric and piezoelectric properties have been observed to improve in the samples prepared by mechanical activation process compared to that in the samples prepared by conventional solid-state reaction technique indicate the superiority of mechanical activation process over the conventional solid-state reaction method.

7.2 Scope for Future Studies

- These compositions can also be prepared by chemical routes and properties can be compared with those prepared by solid- state reaction techniques.
- The investigated compounds can be studied using XPS technique to find out the valencies of the cations.
- The temperature dependent X-ray diffraction studies can be taken up to understand the structural changes in the Curie temperature region and beyond.
- Barium strontium titanate can be studied in microwave region.
- Tunability, i.e., the degree of variation in the dielectric constant with electric field should be taken up to investigate the suitability for devices.

- Voltage- modulation scanning force microscopy has proven to be a powerful tool to characterize ferroelectric films and nanostructures on the nanometer scale. Hence, this work can be taken up for better understanding of ferroelectric properties of the studied compositions in thin films and nanostructured forms.
- Neutron diffraction study should be undertaken to investigate cationic and anionic disorders.